DIGITAL SIGNAL PROCESSING FOR LASER PHASE NOISE COMPENSATION IN HIGH-CAPACITY DIGITAL COHERENT TRANSMISSION SYSTEMS

YULIANG GAO

Ph.D

The Hong Kong Polytechnic University

2015

The Hong Kong Polytechnic University

Department of Electrical Engineering

DIGITAL SIGNAL PROCESSING FOR LASER PHASE NOISE COMPENSATION IN HIGH-CAPACITY DIGITAL COHERENT TRANSMISSION SYSTEMS

YULIANG GAO

A thesis submitted in partial fulfillment of the requirements for

the degree of Doctor of Philosophy

February 2015

Certificate of Originality

I hereby declare that this thesis is my own work and that, to the best of my knowledge and belief, it reproduces no material previously published or written, nor material that has been accepted for the award of any other degree or diploma, except where due acknowledgement has been made in the text.

…….. (Signed)

YULIANG GAO
…….. (Name of student)

Abstract

Capacities in optical transmission networks must evolve to catch up with the recent customers' demand for high bandwidth services such as streaming video, video-on-demand, and cloud-based storage/computing. The emerging demands for bandwidth consuming services promote the development of digital signal processing in coherent optical communication systems. In the receiver side, recent advances in high order modulation detection requires future carrier phase estimation (CPE) algorithms to be more robust, efficient and even adaptive. This thesis focuses on developing three advanced carrier phase recovery techniques that are suitable for various applications such as high efficient transmissions, elastic optical networks and advanced data detection technologies with software-defined forward error correction.

In the second chapter, an advanced CPE technique suitable for hardware efficient implementation in dual-polarization (DP)-16QAM system is proposed. The proposed CPE use quadrature phase shift keying (QPSK) partitioning and maximum likelihood detection to offer similar laser linewidth tolerance with much reduced calculation complexity comparing to other CPE techniques reported in the literatures. The impact of average length to the laser linewidth tolerance is numerically studied, and the computational complexity is discussed in detail. We also experimentally verified its tolerance to laser linewidth in a 200 Gb/s DP-16-QAM system. Due to its feed-forward structure and reduced computation complexity, the algorithm is suitable for future real-time recovery applications for 16-QAM signals.

For higher order modulation formats and elastic optical networks, a blind and universal digital signal processing technique for the recovery of any square-shaped QAM or time-domain hybrid QAM (TDHQ) signals is proposed. Without the aid of training symbols, the algorithm provides fast and robust signal recovery that greatly simplifies the receiver implementation for future dynamic or elastic optical networks. The platform is consisted of several newly proposed techniques such as a modulation-format-independent CPE (MFI-CPE) and a modulation independent joint timing phase and frequency offset estimation module. The transmission performance is fully studied both numerically and experimentally in 28Gbaud transmission systems with various modulation formats. Comparing with traditional training symbol aided technologies, the proposed MFI-CPE achieves similar performances.

Finally, a blind and universal cycle-slip detection and correction (CS-DC) technique is proposed. We analytically derive the probability density function (pdf) of cycle slip (CS) after CS-DC and analyzed the impact of detetion threshold to the correction accuracy. The analytical model agrees well with the Mont-Carlo simulation results and gives more accurate estimation when CS probability is extremely low. Extensive simulation results suggest that the proposed CS-DC technique can successfully reduce the CS probability by over one order of magnitude. In addition, we also proposed to cascaded two CS-DC stages to drive the CS probability further down by two order of magnitudes to 2×10^{-7} in 28 GBaud PM-QPSK and PM-16-QAM transmission systems even with an extreme amount of fiber

nonlinearities. In the end, simulations results demonstrate that the proposed algorithm is robust against residue frequency offset and inter-channel nonlinear distortions.

Publications Arising From the Thesis

Journal articles

[1] K. Zhong, X. Zhou, Y. Gui, L. Tao, **Y. Gao**, W. Chen, J. Man, L. Zeng, A. P. K. Lau, C. Lu, "Experimental study of PAM-4, CAP-16, and DMT for 100Gb/s short reach optica transmission systems," ***Optics Express***, Vol. 23, No. 2, pp: 1176-1189, 2015.

[2] **Y. Gao**, E. Ha, A. P. T. Lau, C. Lu, X. Xu, and L. Li, "Non-data_aided and universal cycle slip detection and correction for coherent communication systems," ***Optics Express***, Vol. 22, No. 25, pp: 31167-31179, 2014.

[3] W. Wang, Q. Zhuge, M. Morsy-Osman, **Y. Gao**, X. Xu, M. Chagnon, M. Qiu, M. T. Hoang, F. Zhang, R. Li, and D. V. Plant, "Decision-aided sampling frequency offset compensation for reduced-guard-interval coherent optical OFDM systems," ***Optics Express***, Vol. 22, No. 22, pp: 27553-27564, 2014.

[4] X. Zhou, K. Zhong, **Y. Gao**, C. Lu, A. P. T. Lau, and K. Long, "Modulation-format-independent blind phase search algorithm for coherent optical square M-QAM systems," ***Optics Express***, Vol. 22, No. 20, pp: 24044-24054, 2014.

[5] M. Qiu, Q. Zhuge, M. Chagnon, **Y. Gao**, X. Xu, M. Morsy-Osman and P. V. Plant, "Digital subcarrier multiplexing for fiber nonlinearity mitigation incoherent optical communication systems", ***Optics Express***，Vol. 22, No. 15, pp:18770-18777, 2014.

[6] W. Wang, Q. Zhuge, **Y. Gao**, M. Qiu, M. Morsy-Osman, M. Chagnon, X. Xu and D. V. Plant, "Low overhead and nonlinear-tolerant adaptive zero-guard-interval CO-OFDM"，***Optics Express***，Vol. 22, No. 15, pp:17810-17822, 2014.

[7] A. P. T. Lau, **Y. Gao**, Q. Sui, D. Wang, Q. Zhuge, M. H. Morsy-Osman, M.

Chagnon, X. Xu, C. Lu, D. V. Plant, “Advanced DSP Techniques Enabling High Spectral Efficiency and Flexible Transmissions: Toward elastic optical networks” ***IEEE Signal Process. Mag***., vol. 31, no. 2, pp. 82-92, March. 2014.

[8] L. Tao, Y. Wang, **Y. Gao**, A. P. T. Lau, N. Chi, C. Lu, “40 Gb/s CAP32 System With DD-LMS Equalizer for Short Reach Optical Transmissions” ***IEEE PHOTONICS TECHNOLOGY LETTERS,*** Vol. 25, NO. 23, pp. 2346-2349, Dec. 1, 2013 .

[9] **Y. Gao**, A. P. T. Lau, C. Lu, “Modulation-Format-Independent Carrier Phase Estimation Technique for Square M-QAM Systems” ***IEEE PHOTONICS TECHNOLOGY LETTERS***, Vol. 25, NO. 11, pp:1073-1076, June 1, 2013 .

[10] L. Tao, Y. Wang, **Y. Gao**, A. P. T. Lau, N. Chi, and C. Lu, “Experimental demonstration of 10 Gb/s multi-level carrier-less amplitude and phase modulation for short range optical communication systems”，***Optics Express***，vol. 21, no. 5, pp. 6459-6465, 2013.

[11] S. Yan, X. Weng, **Y. Gao**, C. Lu, A. P.T. Lau, Y. Ji, L. Liu, and X. Xu, “Generation of square or hexagonal 16-QAM signals using a dual-drive IQ modulator driven by binary signals”，***Optics Express***，vol. 20, no. 27, pp. 29023-29034,2012.

[12] **Y. Gao**, A. P. T. Lau, S. Yan, and C. Lu, "Low-complexity and phase noise tolerant carrier phase estimation for dual-polarization 16-QAM systems," ***Opt. Express***, vol. 19, no. 22, 21717–21729, 2011.

Conference articles

[13] W. Wang, Q. Zhuge, **Y. Gao**, D. V. Plant, “Design of enhanced channel equalizers for adaptive zero-guard-interval CO-OFDM systems,” in Proceedings OFC/NFOEC, Los Angeles, CA, 2015, Paper Th2A.26.

[14] W. Wang, Q. Zhuge, **Y. Gao**, X. Xu, D. V. Plant, "Performance optimization in ROADM-enabled DWDM systems using flexible modulation formats," in Proceedings OFC/NFOEC, Los Angeles, CA, 2015, Paper Th2A.27.

[15] F. Zhang, Q. Zhuge, M. Qiu, X. Xu, W. Wang, **Y. Gao**, M. Chagnon, D. V. Plant, "Advanced and low-complexity digital backpropagatoin for subcarrier-multiplexing systems," in Proceedings OFC/NFOEC, Los Angeles, CA, 2015, Paper Th3D.4.

[16] A. P. T. Lau, **Y. Gao**, Q. Sui, D. Wang and C. Lu, "Advanced DSP for High Spectral Efficiency and Flexible Optical Communications," in *Signal Processing in Photonic Commun. 2014*, paper SM2D.1.

[17] A. P. T. Lau , **Y. Gao**, Q. Sui, D. Wang, C. Lu, "Advanced DSP Techniques Enabling Flexible Transmissions and Elastic Optical Networks," in *International Photonics and OptoElectronics Meetings (POEM) 2014*, paper OTh3B.3.

[18] L. Tao, Y. Wang, **Y. Gao**, A. P. T. Lau, C. Lu, "10 Gb/s CAP128 System using Directly Modulated Laser for Short Reach Optical Communications," in Proceedings OFC/NFOEC, San Francisco, CA, 2014, Paper Th3K.1.

[19] **Y. Gao**, Q. Zhuge, D. V. Plant, C. Lu and A. P. T. Lau, "Blind and Universal DSP for Arbitrary Modulation Formats and Time Domain Hybrid QAM Transmisssions," in Proceedings OFC/NFOEC, San Francisco, CA, 2014, Paper Th3E.5.

[20] **Y. Gao**, A. P. T. Lau, C. Lu, Y. Dai and X. Xu, "Blind Cycle-Slip Detection and Correction for Coherent Communication Systems" in Proc. ECOC, London, UK, 2013, Paper P. 3. 16.

[21] A. P. T. Lau, **Y. Gao**, Q. Sui, D. Wang, Q. Zhuge, M. M. Osman, M. Chagnon, X. Xu, C. Lu and D. V. Plant, "Beyond 100 Gb/s: Advanced DSP Techniques Enabling High Spectral Efficiency and Flexible Optical Communications," in

International Conference on Optical Commun. and Networks (ICOCN) 2013, paper SC1In9.

[22] **Y. Gao**, A. P. T. Lau and C. Lu, "Residual Carrier-Aided Frequency Offset Estimation for Square 16-QAM Systems" in Proceeding CLEO-PR & OECC/PS, Kyoto, Japan, 2013.

[23] S. Yan, D. Wang, **Y. Gao**, C. Lu, A. P. T. Lau, Y. Zhu, Y. Dai, X. Xu, "Generation of 64-QAM using a single dual-drive IQ modulator driven by 4-level and binary electrical signals" in Proceedings OFC/NFOEC, Anaheim, CA, 2013, Paper OM3C.5.

[24] **Y. Gao**, A. P. T. Lau, C. Lu, "Cycle-slip Resilient Carrier Phase Estimation for Polarization Multiplexed 16-QAM Systems" in Proceeding OECC, Busan, Korea, 2012, Paper SC2_1077.

[25] S. Yan, D. Wang, **Y. Gao**, C. Lu, A. P. T. Lau, L. Liu, X. Xu, "Generation of square or hexagonal 16-QAM signals using a single dual drive IQ modulator driven by binary signals" in Proceeding OFC/NFOEC, Los Angeles, CA, 2012, Paper OW3H. 3.

[26] **Y. Gao**, A. P. T. Lau, C. Lu, Y. Li, J. Wu, K. Xu, W. Li, and J. Lin, "Low-Complexity Two-Stage Carrier Phase Estimation for 16-QAM Systems using QPSK Partitioning and Maximum Likelihood Detection" in Proceedings OFC/NFOEC, Los Angeles, CA, 2011, Paper OMJ6.

Acknowledgments

First of all, I am especially thankful to my doctoral advisor Dr. Alan Pak Tao Lau for providing me this precious opportunity to study at Photonics Research Centre. He not only guided me with his professional knowledge but also taught me the way of thinking and the attitude of research.

Secondly, I would like to send my sincere appreciation to Professor David V. Plant for offering me the great opportunity to work as a Post Graduate Trainee in McGill University. Without his generous sharing and kind guidance, the exchange study would never be so fruitful and rewarding.

Thirdly, I am heartily thankful to my co-supervisors Professor LU Chao and Hwa-yaw TAM for their valuable insights and discussions. Without their kind help, this work can never be possible.

Furthermore, I am grateful to the current and former colleagues at Photonics Research Centre: Shuangyi Yan, Qi Sui, Elwin Ha, Junwen Zhang, Li Tao, Kangping Zhong, Jie Liu, Dawei Wang, Faisal N. Khan, Xuan Weng, and Dezhao Huang. It is an honor to work in the group. I would also like to thank the colleagues from McGill University: Qunbi Zhuge, Wei Wang, Meng Qiu, Xian Xu, Mohammed Morsy-Osman, Mathieu Chagnon, Jonathan M. Buset, Minh Thang Hoang, Rui Li, Fangyuang Zhang, Chunshu Zhang, and Junjia Wang for their insightful discussion and continuous assistance.

Last but not least, thanks to my parents who give me support all the way along.

Table of Contents

List of Abbreviations

ADC	Analogue-digital converter
ASE	Amplified spontaneous emission
ASIC	Application Specific Integrated Circuit
BER	Bit error ratio
BPS	Blind phase search
BVT	Bandwidth-variable transceiver
CD	Chromatic dispersion
CMA	Constant modulus algorithm
CMMA	Cascaded multi-modulus algorithm
CPE	Carrier phase estimation
CS-DC	Cycle slip detection and correction
CSP	Cycle slip probability
DA	Data-aided
DAC	Digital-to-analog converter
DD-LMS	Decision directed-least mean square
DE	Differential encoding
DFB	Distributed-feedback
DGD	Differential group delay
DOP	Degree of polarization
DP	Dual polarization

DPSK	Differential phase shift keying
DQPSK	Differential quadrature phase shift keying
DSP	Digital signal processing
ECL	External cavity laser
EDFA	Erbium doped fiber amplifier
EON	Elastic optical networks
FIR	Finite impulse response
FOE	Frequency offset estimation
FPGA	Field-programmable gate array
GVD	Group velocity dispersion
i.i.d.	independent identically distributed
LMS	Least-mean square
LO	Local oscillator
LP	Linear polarized
MFI	Modulation-format-independent
MFO	Modulation-format-oblivious
MIMO	Multi-input multi-output
ML	Maximum-likelihood
MMA	Multi-modulus algorithm
MMSE	Minimum mean square error
NDA	Non-data-aided

OFDE	Overlap frequency domain equalization
OOK	On-off-keying
OPM	Optical performance monitoring
OSNR	Optical signal-to-noise ratio
OTN	Optical transmission network
PBC	Polarization beam combiner
PBS	Polarization beam splitter
PDF	Probability density function
PDL	Polarization dependent loss
PDM	Polarization-division multiplexed
PLL	phase-lock loop
PM	Polarization multiplexing
PMD	Polarization mode dispersion
PRBS	Pseudo-random bit sequence
PS	Polarization scrambler
PSD	Power spectral density
PSP	Principal states of polarization
QAM	Quadrature amplitude modulation
QPSK	Quadrature phase-shift keying
ROADM	Reconfigurable optical add/drop multiplexer
SD-FEC	soft decision-forward error correction

SE	Spectral efficiency
SR-CPE	Slip-reduced carrier phase estimation
SMF	Single mode fiber
SOP	State of polarization
SP	Service provider
TDHQ	Time-domain hybrid QAM
TPE	Timing phase estimation
TS	Training symbol
U-DSP	Universal digital signal processing
VVPE	Viterbi and Viterbi phase estimation
WDM	Wavelength division multiplexed

Chapter 1 Introduction

The un-preceded demand for data capacity has fueled the development of fiber-optic communication continuously over the last decade [1]. This insatiable and relentless demand of modern optical transmission network requires transmission systems to push the capacity to the limit while minimizing the system bandwidth. To this end, advanced systems seek to encode the signal on every possible degree of freedom of an optical carrier such as signal amplitude, frequency, optical phase as well as polarization states.

1.1. Evolution of Optical Communication Systems

Before the era of coherent detection, most of the researchers in optical transmission networks are focused on binary modulation and time domain multiplexing technologies such as optical time domain multiplexing [2] or electrical domain multiplexing [3]. However, the commercialization of both systems was not successful since it is difficult to transmit such short optical pulses in the optical fiber. In addition, the binary modulation has a low spectral efficiency (SE) and thus requires a large bandwidth that imposed a great challenge for both the electrical and optical components. Various multiplexing technologies have been introduced to reduce the symbol rate and alleviate the stringent bandwidth requirements for the components. One of the most adopted technologies in optical transmission networks is wavelength

division-multiplexing (WDM). In 1978, WDM was first published and were being experimentally realized by 1980 with only two channels combined. At present, modern WDM systems can handle up to 160 channels and can thereby expand the system capacity of one single mode fiber (SMF) to well over 1.6 Tbit/s.

On the other hand, high order modulation formats have been recently developed to increase the spectral efficiency further and results in multifold growth in system data rate. For current 100G channel designs, differential quadrature phase shift keying (DQPSK) modulation format has been vigorously studied. Each DQPSK symbol has four modulation levels representing two data bits, for this reason, the symbols rate can be made half of the data rate. In experiments, a 107Gb/s DQPSK channel was designed with a symbol rate of 53.5 Gbaud [4].

In the first decade of this century, the telecom industry selected one optimal 100G signalling format for long haul optical transmission links - two single-carrier QPSK channels on two orthogonal polarization states at the same time, e.g. polarization multiplexed(PM)-QPSK [5]. With this design, the symbol rate is furhter reduced to one-quarter of the data rate, around 30 Gbaud, which fits well within the bandwidth of commercially available optical modulators. Fig. 1.1 summarizes a variety of modulation and multiplexing possibilities in a single-mode optical fiber system, which supports a single transverse mode in two polarizations.

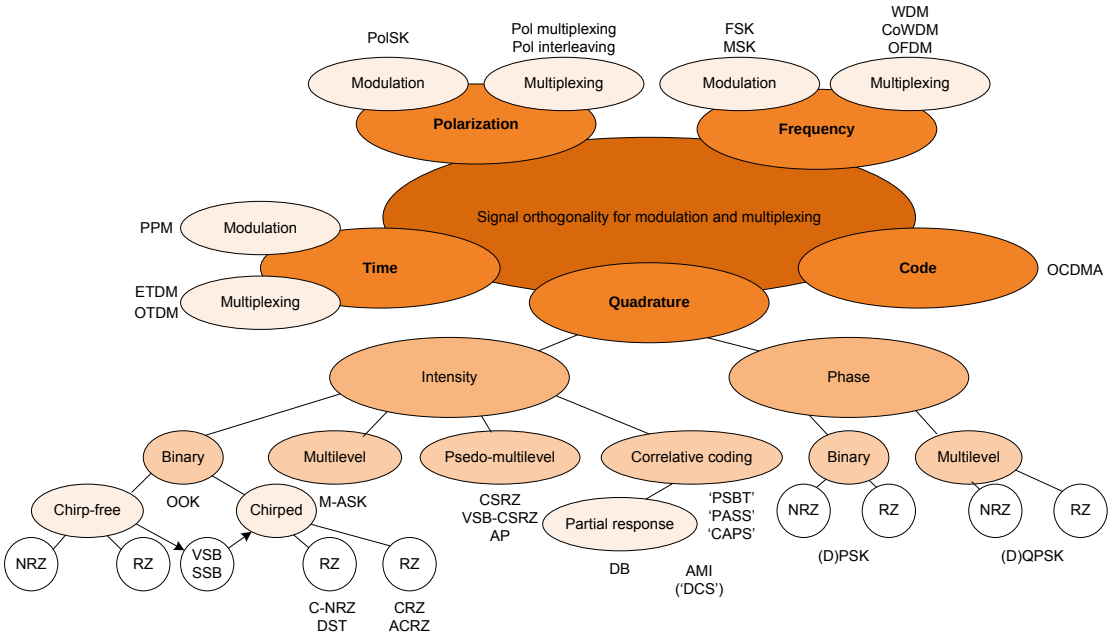

Fig. 1.1 Classification of the most important modulation formats and multiplexing schemes discussed in recent optical communications [6].

Coherent detection enabled PM-QPSK at 100 Gb/s per channel transponders are already in wide deployments. In 2010, OTU4 in ITU-T G.709 was finalized as the standard for 100Gb/s transport channel capacity, and 100 GbE in IEEE 802.3ba was the standard for 100Gb/s Ethernet port speed. In 2012, 400 Gb/s and 1 Tb/s per channel transmission using 16-ary quadrature amplitude modulation (16-QAM) formats and above are demonstrated and beginning to be commercialized for the next generation systems. Table 1.1 shows the typical specifications of existing commercial 100G systems.

Table 1.1 Typical specifications of commercial 100G systems

Item	Value
Optical band used	C-band
Optical bandwidth	4.5 THz
Number of 100G channels	90
Total system capacity	9Tb/s
Channel spacing	50 GHz
Modulation format	PM-QPSK
Protocol and FEC overhead ratio	25%
Reach distance	2500 km
Chromatic dispersion tolerance	50,000 ps/nm

1.2. Coherent Detection

The high order modulation and advanced multiplexing technologies at the transmitter side demands a new reception technology that can linearly handle the whole optical signal and capable of down-conversion it to a baseband electrical signal. In late 1980's and early 1990's, coherent detection was extensively studied as one of the promising technologies that is capable of both amplitude and phase detection by beating the signal with another receiver-side laser output, i.e. local oscillator (LO). By exploiting the beating term, coherent receivers allow detection of any advanced modulation format and are regarded as a game changer in the modern OTN.

Coherent detection was heavily studied to enhance receiver sensitivity in the late 1980s and 1990s [7]. However, inline optical amplification proved to be a cheaper and easier way to improve system performance. Although the coherent detection was then criticized by adding some complexity to the receiver, it is still a giant leap given that the whole information of an optical signal can be accessed which is essential in

promoting the system capacity especially in high spectral efficiency transmission systems. In addition, with full information of the electrical field, the receiver tolerance to noise can be greatly improved, and fiber propagation impairments can be compensated using signal processing.

The fundamental concept behind coherent detection is to take the product of electric fields of the modulated signal light and the continuous-wave LO as shown in Fig. 1.2. At the transmitter side, the optical signal can be described by

$$E_s = A_s exp(j\omega_s t) \tag{0.1}$$

where $A_s(t)$ is the complex signal and ω_s is the angular frequency. Similarly, the field of the LO can be described by

$$E_{LO}(t) = A_{LO} exp(j\omega_{LO} t) \tag{0.2}$$

where A_{LO} is the LO amplitude and ω_{LO} is the angular frequency of the LO. We note here that the complex amplitudes A_s and A_{LO} are related to the power of the optical fields by $P_s = |A_s|^2/2$ and $P_{LO} = |A_{LO}|^2/2$, where P_s and P_{LO} are the power of the signal and LO, respectively.

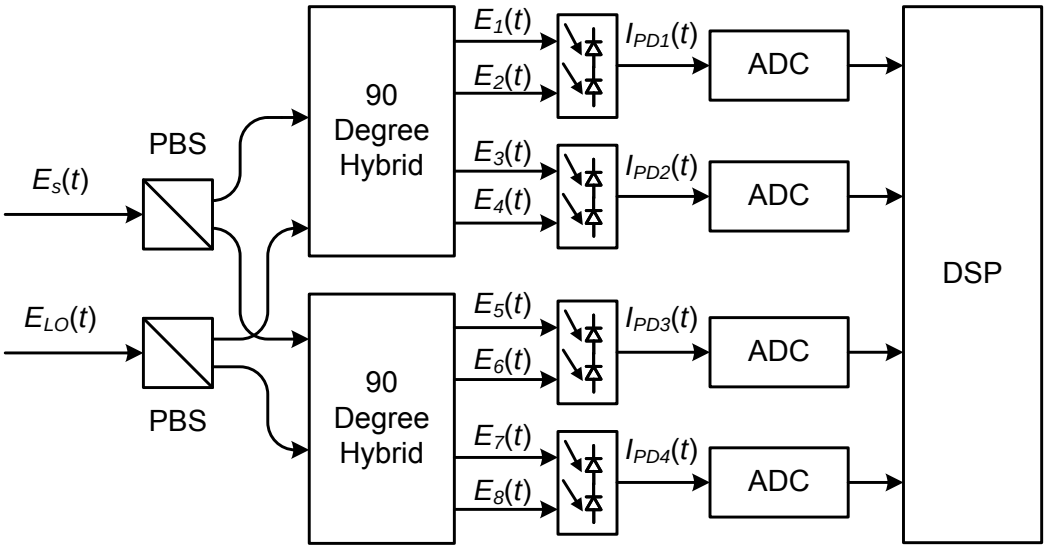

Fig. 1.2 Configuration of the phase/polarization diversity receiver.

In practical polarization multiplexed systems, polarization diversity coherent receivers should be implemented because the SOP of the incoming signal is random and is not likely to remain aligned to that LO all the time. The receiver employing polarization diversity is shown in Fig. 1.2, where the two phase-diversity homodyne receivers are combined with the polarization diversity configuration. After the polarization beam splitter (PBS), the arbitrary state of polarization (SOP) of the signal is separated into two linear polarization components. Let the *x*- and *y*-polarization components after PBS be written as

$$\begin{bmatrix} E_{sx}(t) \\ E_{sy}(t) \end{bmatrix} = \begin{bmatrix} \sqrt{\alpha} A_s e^{j\delta} \\ \sqrt{1-\alpha} A_s \end{bmatrix} exp(j\omega_s t) \tag{0.3}$$

where α is the power splitting ratio of the two polarization components and δ is the phase difference between them. These parameters are dependent on the birefringence of the transmission fiber and is time varying in general. In contrast, the *x*- and *y*-polarization components equally separated from the linearly polarized LO are

written as

$$\begin{bmatrix} E_{LOx} \\ E_{LOy} \end{bmatrix} = \frac{1}{\sqrt{2}} \begin{bmatrix} A_{LO} \\ A_{LO} \end{bmatrix} exp(j\omega_{LO}t) \tag{0.4}$$

The 90 ° optical hybrids in Fig generate electric field $E_{1,\ldots,8}$ at the double-balanced photodiodes PD1-PD4:

$$E_{1,2} = \frac{1}{2}\left(E_{sx} \pm \frac{1}{\sqrt{2}}E_{LO}\right), \tag{0.5}$$

$$E_{3,4} = \frac{1}{2}\left(E_{sx} \pm \frac{j}{\sqrt{2}}E_{LO}\right), \tag{0.6}$$

$$E_{5,6} = \frac{1}{2}\left(E_{sy} \pm \frac{1}{\sqrt{2}}E_{LO}\right), \tag{0.7}$$

$$E_{7,8} = \frac{1}{2}\left(E_{sy} \pm \frac{j}{\sqrt{2}}E_{LO}\right), \tag{0.8}$$

where E_{LO}=$E_{LO,x}$=$E_{LO,y}$. Photocurrents from *PD*1 to *PD*4 are then given as

$$I_{PD1} = R\sqrt{\frac{\alpha P_s P_{LO}}{2}}cos\{\theta_s - \theta_{LO} + \delta\}, \tag{0.9}$$

$$I_{PD2} = R\sqrt{\frac{\alpha P_s P_{LO}}{2}}sin\{\theta_s - \theta_{LO} + \delta\}, \tag{0.10}$$

$$I_{PD3} = R\sqrt{\frac{(1-\alpha) P_s P_{LO}}{2}}cos\{\theta_s - \theta_{LO}\}, \tag{0.11}$$

$$I_{PD4} = R\sqrt{\frac{(1-\alpha) P_s P_{LO}}{2}}sin\{\theta_s - \theta_{LO}\}. \tag{0.12}$$

From (0.9) to (0.12), we find that the polarization-diversity receiver can separately measure complex amplitudes of the two polarization components as

$$I_x(t) = I_{PD1}(t) + jI_{PD2}(t), \tag{0.13}$$

$$I_y(t) = I_{PD3}(t) + jI_{PD4}(t), \tag{0.14}$$

from (0.13) and (0.14) we can reconstruct the complex polarization multiplexed signal although they may suffer from polarization crosstalk at the moment.

1.3. Channel Impairments and Laser Phase Noise

The continuous demand for spectral efficient transmission system results in the resurgence of coherent detection. However, the coherent detected optical field has already experienced various channel impairments during fiber transmissions such as chromatic dispersion, polarization mode dispersion, fiber nonlinearities and laser phase noise. Fig. 1.3 depicts the standard basic model for a long-haul fiber-optic channel consisting of major transmission impairments including chromatic dispersion $H_{CD}(\omega)$, polarization-mode dispersion $H_{PMD}(\omega)$ and amplified spontaneous emission (ASE) noise $n_x(t)$, $n_y(t)$ from inline optical amplifiers, which are typically modeled as complex circularly symmetric zero-mean additive white Gaussian random process. Practical laser imperfections include frequency offset Δf between transmitter laser and local oscillator and laser phase noise $\phi_t(t)$, $\phi_r(t)$ modeled as a Wiener process [1]. In this case, the received signal is given by (1.15) where $\mathcal{F}^{-1}$ denotes inverse Fourier Transform and $\tilde{E}_{t,x(y)}(\omega)$ is the Fourier Transform of $E_{t,x(y)}(t)$.

$$\begin{bmatrix} E_{r,x}(t) \\ E_{r,y}(t) \end{bmatrix} = \mathcal{F}^{-1}\left\{ H_{CD}(\omega) H_{PMD}(\omega) \begin{bmatrix} \tilde{E}_{t,x}(\omega) \\ \tilde{E}_{t,y}(\omega) \end{bmatrix} \right\} \cdot exp\big(j(2\pi\Delta f t + \phi_t(t) + \phi_r(t))\big) + \begin{bmatrix} z_x(t) \\ z_y(t) \end{bmatrix} \quad (0.15)$$

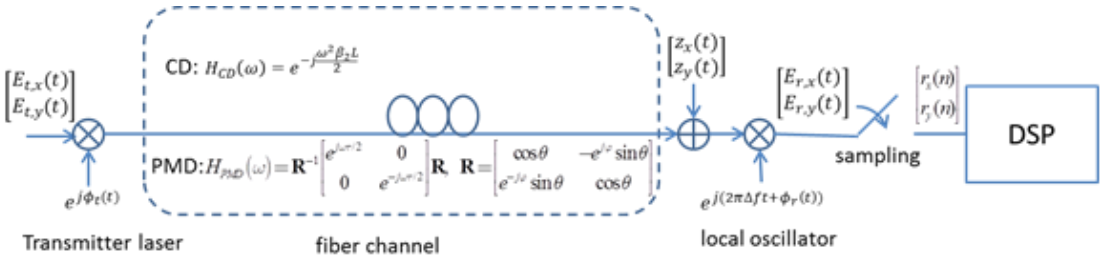

Fig. 1.3 Canonical channel model for polarization-multiplexed long-haul fiber-optic communication systems with digital coherent receivers. The transmitted signal in the *x*-(*y*-)polarization is $E_{t,x}$(t) and $E_{t,y}$(t) and major transmission impairments include CD $H_{CD}(\omega)$, polarization mode dispersion (PMD) $H_{PMD}(\omega)$, amplified spontaneous emission noise $n_x(t)$, $n_y(t)$ as well as laser imperfection-induced impairments such as carrier frequency offset $e^{j2\pi\Delta ft}$ between transmitter laser and local oscillator and laser phase noise $e^{j\phi_t(t)}, e^{j\phi_r(t)}$. In this formulation, L, β, τ denote fiber length, group velocity dispersion (GVD) coefficient and differential group delay (DGD) between two polarization modes respectively and θ, φ are angles relating the input signal's state of polarization (SOP) to the principal states of polarization (PSP) of the fiber.

Among these various impairments, laser phase noise, known as the fluctuation of the optical carrier phase, is a challenging issue in coherent detection systems. Even for a single-frequency laser, where essentially all power is in a single resonator mode, the output will not exhibit a perfect sinusoidal oscillated electric field due to various external influences. For simplicity, phase noise is described as the random phase of photons with spontaneous emission and can be quantified by the power spectral density (PSD) of the phase deviations. The width of the main peak in the PSD is called laser linewidth that leads the optical phase $\phi(t)$ that follows a Wiener process as shown in Fig. 1.4. Here, the phase difference $\phi(t_2)$- $\phi(t_1)$ is modelled as zero-mean Gaussian random variable with variance $2\pi\Delta\nu|t_2 - t_1|$ where $\Delta\nu$ is the laser linewidth.

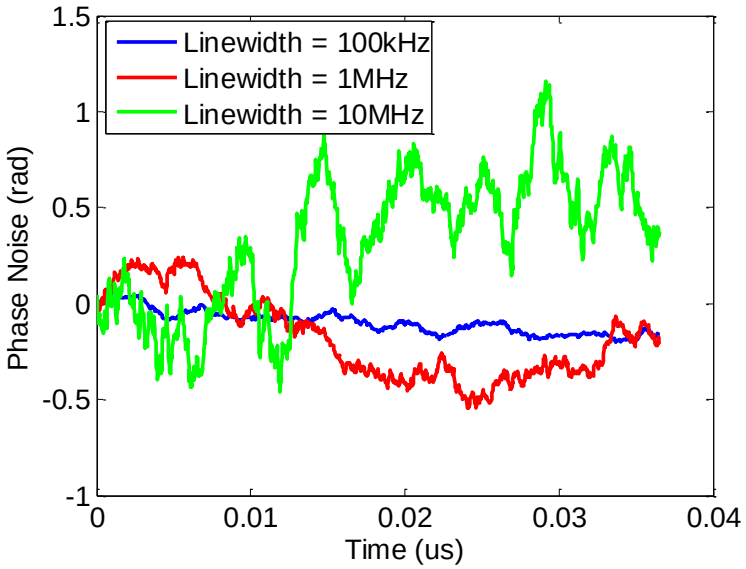

Fig. 1.4 Evolution of laser phase noise in a 28GBaud coherent system with various laser linewidths.

1.4. Digital Signal Processing and Its Function Blocks

A typical DSP platform for long-haul coherent detection usually includes chromatic dispersion compensation, timing phase and frequency compensation, polarization demultiplexing, carrier frequency and phase estimation, etc. Newly developed high-speed analog-to-digital converters (ADC) with about 60-GS/s sampling rate help in digitizing the coherently detected 100G channel for digital signal processing (DSP). With the recent advances in high-speed digital-to-analog converter (DAC) and field-programmable gate array (FPGA) technologies, the real-time recovery and processing of digital signal in the electrical domain becomes reality. Thus, flexible and accurate digital signal compensation techniques for these distortions in the receiver side digital signal processing modules have received tremendous attention in

recent years.

1.4.1. Chromatic Dispersion Compensation

In the absence of fiber nonlinearity, the chromatic dispersion effect on a pulse envelope $A(z,t)$ may be modeled by the following equation [8]

$$\frac{\partial A(z,t)}{\partial z} = j\frac{\beta_2 z}{2}\frac{\partial^2 A(z,t)}{\partial t^2} \tag{0.16}$$

where z is the distance of propagation, t is time variable in a frame moving with the pulse, and β_2 is the GVD coefficient of the fiber.

For CD compensation, one of the widely deployed approaches is the conventional frequency domain equalization (FDE) for a channel with frequency domain transfer function that model (0.16) given by

$$G(z,\omega) = exp\left(-j\frac{\beta_2 z}{2}\omega^2\right) \tag{0.17}$$

where β_2 is the GVD parameter and z is the length of transmission. The frequency response of dispersion compensation filter is thus given by the all-pass filter

$$H(\omega) = \frac{1}{G(\omega)} = exp\left(j\frac{\beta_2 z}{2}\omega^2\right) \tag{0.18}$$

truncated to half of sampling frequency f_s. In particular, overlap frequency domain equalization (OFDE) is chosen for practical implementation considerations [9]. It has also been proved that the FDE is more computational efficient than the time domain equalization. In OFDE implementation, the data is first divided into overlapping blocks then transformed to the frequency domain where the CD is compensated block-by-block as shown in Fig. 1.5.

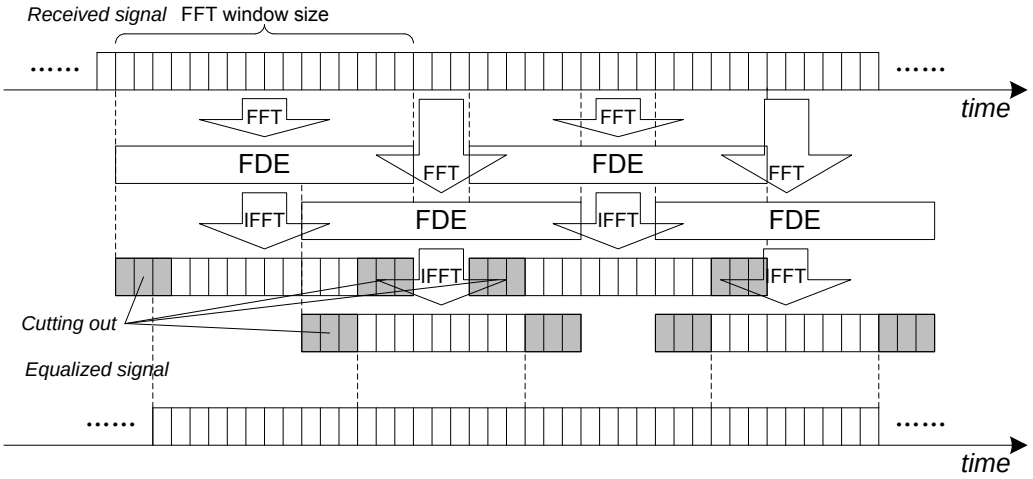

Fig. 1.5 CD compensation using OFDE. Overlapping blocks of data are transformed to frequency domain where the effect of CD is equalized.

1.4.2. Timing Phase Recovery

After compensation of the chromatic dispersion, the timing phase error can be detected by several digital timing phase recovery algorithms for correcting the timing phase error in the data samples, such as Gardner's timing recovery [10], digital filter and square timing recovery [11] or Mueller-Muller timing recovery [12], etc.

In particular, Gardner's algorithm is attractive due to its simplicity and only requiring 2 samples/symbol. This algorithm applies a zero-crossing timing error detector with function of

$$e(k) = x(k - 1/2)(x(k) - x(k - 1)) \tag{0.19}$$

where k is the index of symbol and linear interpolation with feedback structure to perform the timing phase recovery as shown in Fig. 1.6

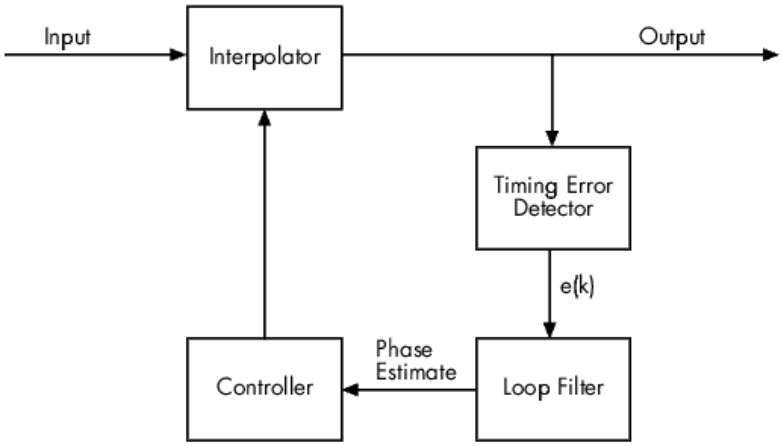

Fig. 1.6 Feedback structure of Gardner's timing error detector

The interpolator generates additional samples based on the needs of the timing error detector. As implemented in our code, the interpolator uses linear interpolation between pairs of points. Cubic or piecewise parabolic interpolators are also applicable. After the timing phase error has been corrected, the data is output at the symbol rate, i.e., 1 sample/symbol with optimal sampling position (or sampling phase).

1.4.3. Polarization Demultiplexing

Polarization-division multiplexed (PDM) signals can also be demultiplexed by digital signal processing without using optical dynamic polarization control at the receiver. A Jones matrix representation may model the impact of polarization dependent effects on the propagation. In contrast to the CD, which may be considered constant, the Jones matrix may evolve in time due to effects such as rapid polarization rotation. Therefore, adaptive compensation schemes must be used, such as constant modulus algorithm (CMA) etc., to correctly demultiplex the two orthogonal polarizations while

compensate other possible polarization dependent distortions such as polarization mode dispersion (PMD), polarization dependent loss (PDL), etc. The goal of polarization demultiplexing is to estimate the inverse Jones matrix by using digital filters with tap coefficients constantly updated by a specific error function. It has been shown that optical communications using PDM is analogous to wireless communications using multiple-input-multiple-output (MIMO) antennae and so the algorithms for channel equalization in wireless communications can be readily applied to optical communications [13].

Among the numerous algorithms, CMA proposed by D. N. Godard is one of the most preferred due to its good performance and simplicity stucture [14]. As compared to the decision-directed least-mean-square (DD-LMS) algorithm, the CMA is decision-independent. It allows us to separate the task of polarization de-multiplexing and carrier phase recovery in different functional blocks, which cannot be realized by using a decision-dependent algorithm such as the DD-LMS.

Although the classic CMA is quite appropriate for square QAM signals in Nyquist WDM systems, several modified versions have been employed such as cascaded multi-modulus algorithm (CMMA) [15] and multi-modulus algorithm (MMA) [16], etc., to achieve better optical signal-to-noise ratio (OSNR) performance in the cost of slower convergence speed and higher computational complexity.

1.4.4. Frequency Offset Estimation

A typical temperature-stabilized wavelength locker for WDM systems has a wavelength accuracy of about ±5 GHz [17], which is much larger than the tolerance of typical carrier phase estimation technologies. Thus, digital frequency estimation techniques and corrections have to be implemented to limit the residue frequency offset within the CPE tolerance.

In order to accurately estimate the carrier frequency offset the modulation information needs to be first eliminated either in a data-aided (DA) or a non-data-aided (NDA) manner. Usually, NDA based frequency offset estimation (FOE) is more widely implemented than DA methods. The most utilized technique finds the FO by locating the maximum power in the Fourier transform of the signal spectrum after it has been processed by an M-th power operation [18] (1.20)

$$z_k = (x_k)^M = e^{j(2M\pi\Delta f kT+\theta)} + n_k \tag{0.20}$$

where x_k is the input, Δf denotes frequency offset, T is the symbol period, θ is carrier phase noise and n_k is the zero-mean additive noise. After the fourth-power operation, the maximum likelihood (ML) estimate of the carrier frequency offset Δf is the location of the maximum amplitude of in tis spectrum i.e.

$$\widehat{\Delta f} = argmax\left\{\left|\frac{1}{L}\sum_{k=0}^{L-1} z_k e^{j2\pi\frac{nk}{N}}\right|\right\} \tag{0.21}$$

1.4.5. Carrier Phase Estimation

CPE is an important component of coherent communications. In radio communication

a system, phase synchronization is typically achieved by a phase-lock loop (PLL) employing a one-tap least-mean square (LMS) filter to implement decision-directed phase estimation in a feedback manner. Feedback techniques rely on calculating the phase estimate $\phi(k)$ from $r_{CPE}(k)$ and the symbol decision $\hat{s}(k)$ and use it as the initial estimate for $\phi(k+L)$ where L denotes the total feedback delay. L is determined by the degree of parallelization P and pipelining (number of steps in an algorithm).

Unfortunately, in high-speed optical communications, required ASIC parallelizations may create a large feedback delay and considerably limit practical use of feedback algorithms. On the other hand, phase noise in optical communications is typically much larger than that in wireless communications which makes phase estimation a more serious issue especially for higher order modulation formats. To this end, one can either use feedforward algorithms avoiding feedback loops or develop new algorithmic and hardware feedback structures that can somehow reduce P and/or L.

One of the most widely deployed feedforward algorithms for phase estimation in coherent detection systems is the Viterbi & Viterbi phase estimation (VVPE) [19]. After preceding DSP that compensate other impairments and down sampled to symbol rate, let the k^{th} symbol in one polarization going into the CPE unit be

$$r_{CPE}(k) = s(k) \cdot e^{j\phi(k)} + n(k) \tag{0.22}$$

where $\phi(k) = \phi_t(k) + \phi_r(k)$ is the combined transmitter and receiver phase noise and $n(k)$ is the additive ASE noise. For quadrature phase-shift keying (QPSK) signal,

signal $s(k)$ can be expressed as

$$s(k) = A \cdot exp(j\theta(k)) \tag{0.23}$$

where A denotes the signal amplitude which could be normalized to be 1 for simplicity and $\theta = 0, \pm\pi/2, \pi$ which can be eliminated by raising r_{CPE} to its fourth power, we obtain

$$r_{CPE}^4(k) = exp(j4\theta(k)). \tag{0.24}$$

The carrier phase can then be estimated and compensated from the phase of the received signal as shown in Fig. 1.7.

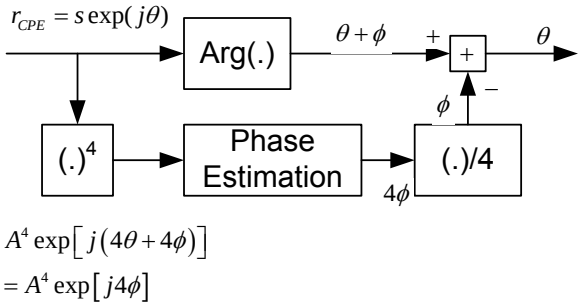

Fig. 1.7 Schematic of phase estimation algorithm for QPSK [20].

For higher-order modulation formats, blind-phase-search [21] is considered as one of the most popular methods which was originally introduced for more general synchronous communication systems [22]. BPS estimator features good tolerance to laser linewidth, blind feedforward manner, and universality to arbitrary QAM formats, however, at expense of huge hardware implementation complexity. Such complexity can be somewhat lowered by reducing the number of 'test phases' using multi-stage approaches [23], [24].

For most of the power efficient modulation formats, constellations distribute

symmetrically around the origin including the widely employed QPSK modulation. This phenomenon is called phase ambiguity. As for the QPSK symbols, all the transmitted symbols locate in the four symmetric quadrants as shown in Fig. 1.8.

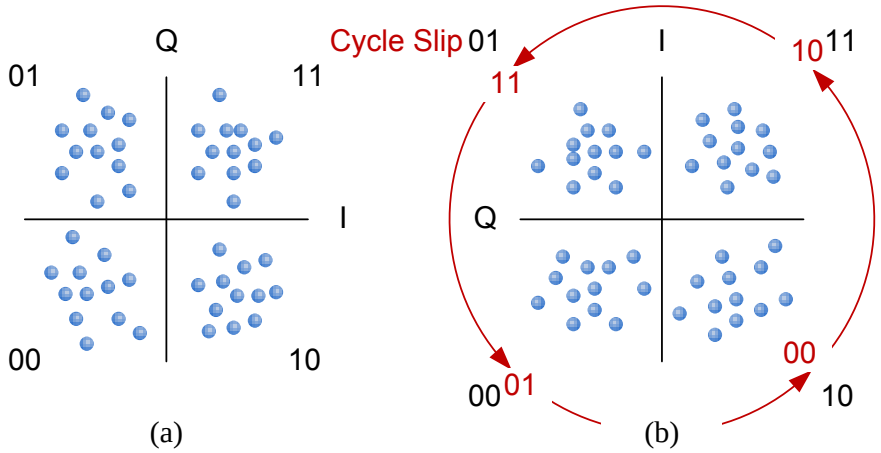

Fig. 1.8 Cycle slip demonstration with slip phases of (a) 0 and (b) $\pi/2$.

Due to phase ambiguity, the QPSK symbols distribute remains the same after $\pi/2$ rotation thus is not detectable for most of the existing CPE methods. However, the rotated symbols convey different bit information from the transmitted ones and will introduce catastrophic error burst.

A cycle slip happens when the CPE output deviate from the actual phase noise by more than half of the ambiguous phase, e.g. $\pi/2$ for QPSK so that the phase ambiguity cannot be corrected. Cycle slips are caused mainly by two different mechanisms. In the first case, the laser phase noise changes too fast for the CPE to catch up with since most of the CPEs are designed to track a slowing varying random walk process. This is possible given a laser output has an unlimited spectral distribution function. Most of the time, the laser phase noise does not change that fast, and contrarily, it is the phase estimate that has been impaired to experience an abrupt

change.

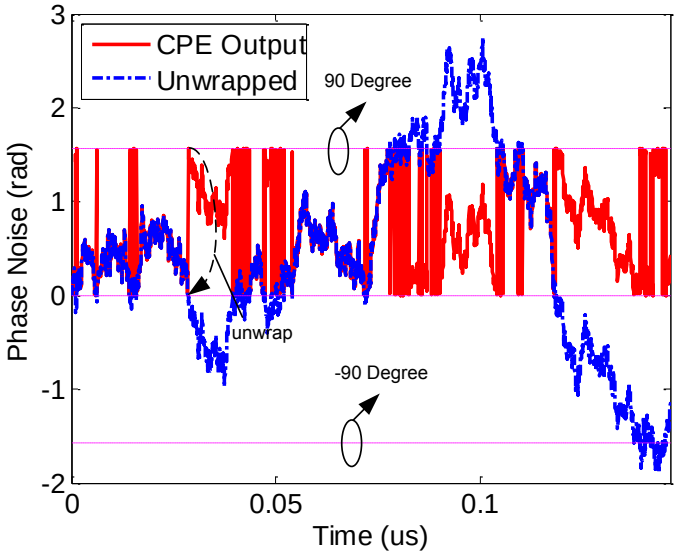

Fig. 1.9 Phase unwrap for QPSK symbols whose ambiguous phase is $\pi/2$. The laser linewidth is 10 MHz.

Without the redundant aiding symbols, the phase estimation range is confined from 0 to $\pi/2$ as described in [21], and so the output needs to be unwrapped as is illustrated in Fig. 1.9. The CPE unwraps its output whenever it crosses the estimation boundaries based on the slow varying assumption of laser phase noise as illustrated in Fig. 1.4. However, the received phase noise after transmission may experience cycle slip effects due to the additional phase noise induced by ASE noise, residue frequency offset or inter-channel nonlinearities, etc. Although at a very rare rate, a single cycle slip may undermine all the date transmission afterwards since a wrong phase estimate persists until redundant symbols are received which causes large error burst that could not be corrected by forward error correction (FEC) technologies.

1.5. Elastic Optical Network

It is envisioned that future Internet traffic will be much more dynamic, unpredictable and heterogeneous in all aspects due to the emergence of large content providers with dynamic traffic demands across optical networks. Consequently, researches enabling flexible/adaptive transmissions or elastic optical networking (EON) to maximize network efficiency have recently attracted a lot of attention [25]. Continued global traffic growth at an exponential rate around 40% per year is posing major challenges for the service provider (SP) networks. These challenges imply that the optical layer will have to be low cost, flexible, and reconfigurable:

Low cost: the future network must be as spectrally efficient as possible as the result of the increased pressure on SP margins. Today's network is developing a streamlined system in which only two layers can be afforded: a transport layer and a service layer.

Flexible: the dynamic service provisioning requires the network will have to be realized in a flexible manner. The existing "one size fits all" approach widely adopted in previous generation DWDM systems will no longer work, and software configuration will have to be accommodated instead.

Configurable: to cope with the unpredictable traffic patterns, connection should be set up for any source/destination and any available resources should be utilized.

Reconfigurable: to avoid resource idling and increase resources utilization efficiency, capabilities of fast release, redeployment and re-optimization have to be incorporated in future dynamic networks. In terms of the physical layer, we would favor a single

and universal software-defined bandwidth-variable transceiver (BVT) [26] that is applicable to different carrier wavelength, bit rate, symbol rate, modulation format and coding and/or path of transmission across the network.

To address the conflict between service provider's limited provisioning capacity and clients' increasing demands for higher bandwidth, a new "elastic" networking design [27] has been proposed enabling SPs to update their system without frequently overhauling it. In a recent two years, 100 Gb/s-based transmission systems have been rapidly deployed since they fit well with the existing ITU grid of 50 GHz without breaking any grid boundaries. For the next generation considerations, both the Telecom and Datacom industries are looking forward to a physical layer design beyond 100Gb/s, and 400 Gb/s is one of the most promising candidates. Unfortunately, it is hard for the 400Gb/s to be fitted into the 50GHz ITU grid using reasonable modulation formats since a higher spectral efficiency modulation format would greatly reduce the maximum transmission reach.

Fig. 1.10 shows an existing ITU grid (top) vs. a flexible grid (bottom). The fixed grid does not support bit rates of 400 Gb/s and 1 Tb/s at standard modulation formats as they overlap with at least one 50 GHz grid boundary. Also, the existing grid stardard has more idle bandwidth which is a huge waste of the precious bandwidth resources. For different requirements, e.g. distance and capacity, ect., the agile modulation format adjustment technique could also be introduced to minimize the bandwidth consumption of future EON systems.

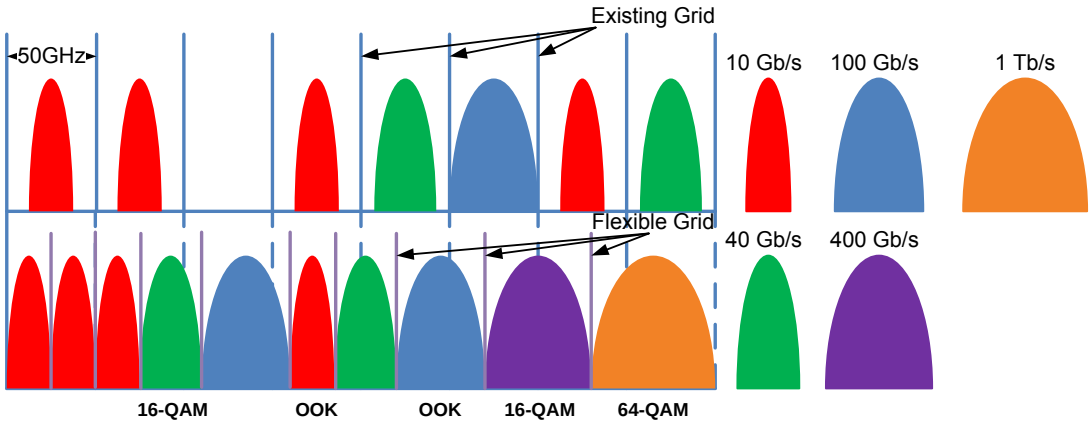

Fig. 1.10 Use of spectrum for a link with different bit rates [25].

1.6. New challenges for Carrier Phase Estimation

As we move from QPSK to higher order QAM formats (e.g. 16-QAM) and commensurate baud rates, several impairments impose unique and extremely stringent constraints on system performance that are unforeseen in wireless/copper-wire systems. This situation has led to a series of new challenges in the CPE research for long-haul coherent optical systems:

The sampling rate for optical systems is of the order of tens of Giga-samples per second while current Application Specific Integrated Circuit (ASIC) technologies support serial processing speeds of approximately 1 GHz [28]. Therefore, while massive algorithmic/hardware parallelization is required, this approach can exacerbate laser phase noise-induced impairments in feedforward as well as feedback algorithms. Considering larger oscillator phase noise compared with wireless systems, CPE and its hardware structures for high speed optical applications need to be optimized to reduce such parallelization penalties with low computation complexity.

Moving forward, 400 Gb/s and 1 Tb/s per channel transmission using 16-QAM and above were demonstrated and commercialized in 2012. The next generation of hardware (e.g. Digital to Analog Converters) and software (e.g. programmability) advances will enable EON. One of the key challenges in enabling EONs is the need to employ adaptive/flexible receiver CPE supporting multiple baud rates, bandwidths, and modulation formats.

Most CPE techniques suffer from the problem of cycle slips (CS) in which the received signal are phase rotated by any integer multiple of $\pi/2$ and leads to catastrophic detection error. To cope with this problem, one can use differential encoding (DE) where information is encoded in the difference between neighboring bits/symbols. On the other hand, we are moving towards soft decision – forward error correction (SD-FEC)-based transmission system, enabling a higher pre-FEC bit error ratio (BER) but at the same time not favor DE. Numerous techniques have been proposed to suppress CSs without DE which basically involves either inserting pilot tones or inserting pilot symbols at regular intervals in the expense of increased transmitter complexity. Thus, it is highly desirable to develop a non-data-aided CS-DC technology applicable to any modulation format.

1.7. Dissertation Outline

Chapter 1 briefly introduces the recent progress of recent advances in optical transmission systems over the past decade. Coherent detection and several major

digital signal processing modules are reviewed. As one of the unique signal processing module in the receiver side recovery platform, the motivation of developing carrier phase estimation algorithms for different optical transmission applications is highlighted. The objective of this dissertation is to propose, design, and analyze three advanced carrier phase estimation technologies that is suitable for long-haul optical transmission links with different modulation formats and spectral efficiency.

In chapter 2, a low-complexity and laser phase noise tolerant carrier phase estimation using QPSK partitioning and maximum likelihood detection is proposed for polarization multiplexed 16-QAM transmission systems. The optimum configurations with respect to various combinations of OSNR and laser linewidth are statistically studied. The maximum phase noise tolerance of the proposed algorithm analyzed based on simulation results. To verify its performance, the QPSK partitioning + ML CPE is also experimentally tested in a 200 Gb/s DP-16-QAM system. In addition, the computation complexity of the proposed algorithm is also analyzed indicating its simplicity and advantage in future high speed and computation efficient real-time digital coherent receivers.

In chapter 3, a modulation-format-independent carrier phase estimation technique is proposed for the future elastic optical transmission system in which a great variety of modulation formats are adopted for maximizing system capacity. To accurately estimate phase noise for different modulation format without frequently

adjusting the estimating module, a new cost function for laser phase noise detection is proposed based on a common constellation feature shared by all the most widely used square-shaped QAM signals. To demonstrate a modulation-format-independent signal reception in a real EON transmission system, we have also proposed a blind and universal DSP platform for the recovery of arbitrary modulation formats and even time domain hybrid QAM transmissions. The proposed DSP platform is comprised of two stages, e.g. an initialization stage and a tracking stage, to achieve rapid, robust initialization of the transmission links meanwhile maintaining a steady, accurate tracking ability. To avoid the use of training symbols several format-universal algorithms has been developed for the initialization stage such as the joint timing phase estimation and frequency offset estimation and modulation-format-independent carrier phase estimation.

In chapter 4, a simple non-data-aided (or unsupervised) and universal cycle slip detection and correction (CS-DC) technique based on locating the minimum of the sliding average of twice estimated phase noise is proposed. We analytically derive the probability density function of the CS detection metric and study how the sliding window length and detection threshold affects CS detection performance. Simulation results reveal significant cycle slips reduction for various modulation formats with a residual CS probability of 2×10^{-7} for single carrier system even in unrealistic highly nonlinear system setups. In addition, we show that a second stage of CS-DC with a different sliding window length can further reduce the cycle slip probability (CSP) by

at least an order of magnitude. We also show that CS-DC is tolerant to inter-channel nonlinearities and residue frequency offset effects.

The conclusion is then made and possible research directions in the future are discussed.

Chapter 2 Low-Complexity and Phase Noise Tolerant Carrier Phase Estimation for Dual-Polarization 16-QAM Systems

2.1. Introduction

The increasing demand for data traffic has continued to motivate research on more spectrally efficient optical transmission systems to better utilize the valuable bandwidth resources of the optical fiber [29], [30]. DP-QPSK operating at 100 Gb/s with receiver digital signal processing (DSP) are now commercially available [31]-[33]. In addition, 16-QAM with its higher SE of 4 bit/s/Hz has become the natural choice and thus promising candidate for next generation optical transmission system beyond 100Gb/s per channel [34]-[36].

Carrier phase estimation is an integral part of DSP-based receiver through which laser phase noise is compensated. For DSP-based receivers, blind and feed-forward CPE are more desirable due to their algorithmic and implementation simplicity [37]. The tolerance of laser phase noise and hence performance of CPE generally degrades for systems using high spectral efficient modulation formats and/or lasers with large linewidths. Consequently, the vast majority of 16-QAM transmission experiments demonstrated in recent years used external cavity lasers (ECL) instead of the more cost effective distributed-feedback (DFB) lasers because of their narrow linewidths [35]. Consequently, linewidth-tolerant and low-complexity CPE is critical for

practical realization of 16-QAM transmission systems in future optical communication systems. To this end, various feed-forward CPE algorithms for 16-QAM systems proposed to date stems from two fundamental approaches: 1) QPSK partitioning schemes [38], [39] which were derived from classical Viterbi and Viterbi phase estimation (VVPE) approach for QPSK signals [19]. However, QPSK partitioning for 16-QAM systems introduces a more stringent linewidth requirement compared to VVPE for QPSK systems; 2) blind-phase-search (BPS, also called the minimum distance method) [21] that was originally introduced for more general synchronous communication systems [22], [40]. BPS demonstrates higher linewidth tolerance but comes with an expense of high computational complexity. Such complexity can be somewhat lowered by reducing the number of 'trial phases' [41]-[44]. In these papers, two-stage strategies have been reported where BPS is used in only one of the two stages as fine [41] or coarse [42] carrier phase estimator or both stages [23], [43]. However, the computational complexity of such modified BPS is not reduced significantly [44].

In this thesis, we extend our previous work [45] and propose a low-complexity and phase-noise tolerant feed-forward CPE for DP-16-QAM systems by using QPSK partitioning with maximum likelihood (ML) detection. In addition, as signals from both polarizations are impaired by identical laser phase noise (up to a constant phase offset due to path differences travelled by signals in different polarizations) in a canonical DP system [46], [47], phase information from both polarizations are jointly

processed for better carrier phase estimation accuracy and hence improved overall transmission performance. Simulation results for a 200 Gb/s DP-16-QAM system demonstrates similar linewidth tolerance and a computational complexity reduction by a factor of at least three compared with other feed-forward CPE techniques with large linewidth tolerance reported in the literature. The performance of the proposed and other feed-forward CPE techniques are also experimentally verified and compared with. Such comparisons also serve as a good experimental assessment of various feed-forward CPE for practical 16-QAM implementation of transmission systems.

2.2. Algorithm Design

Consider a DP-16-QAM system where the received signal is sampled and processed in a DSP. After CD (and possibly nonlinearity compensation), timing recovery, polarization demultiplexing, re-sampling to one sample per symbol and frequency offset compensation, the n^{th} received symbol of the *x*-polariztion (*y*-polarization) can be expressed as

$$s_{n,x(y)} = b_{n,x(y)} \cdot exp\left(j\theta_{n,x(y)}\right) + z_{n,x(y)} \tag{2.1}$$

where $b_{x(y)} = \{\pm 1 \pm j, \pm 3 \pm 3j, \pm 1 \pm 3j, \pm 3 \pm j\}$ are the DP-16-QAM signals, $\theta_{n,x(y)}$ is the combined phase noise of the transmitter laser and LO at the receiver and $z_{n,x(y)}$ models the collective ASE noise generated from inline amplifiers which are complex circularly symmetric Gaussian random processes. Laser phase noise is typically modeled as a Wiener process in which the phase difference between two

adjacent symbols $\theta_{n+1,x(y)} - \theta_{n,x(y)}$ can be modeled as zero-mean Gaussian random variable with variance $\sigma^2 = 2\pi\Delta v \cdot T_s$ where T_s is the symbol period, Δv is the combined linewidths of the transmitter laser and LO.

The proposed CPE is a multi-stage algorithm consisting of QPSK partitioning, phase offset (between signals in different polarization) compensation followed by an ML detection. The block diagram of the CPE is shown in Fig. 2.1.

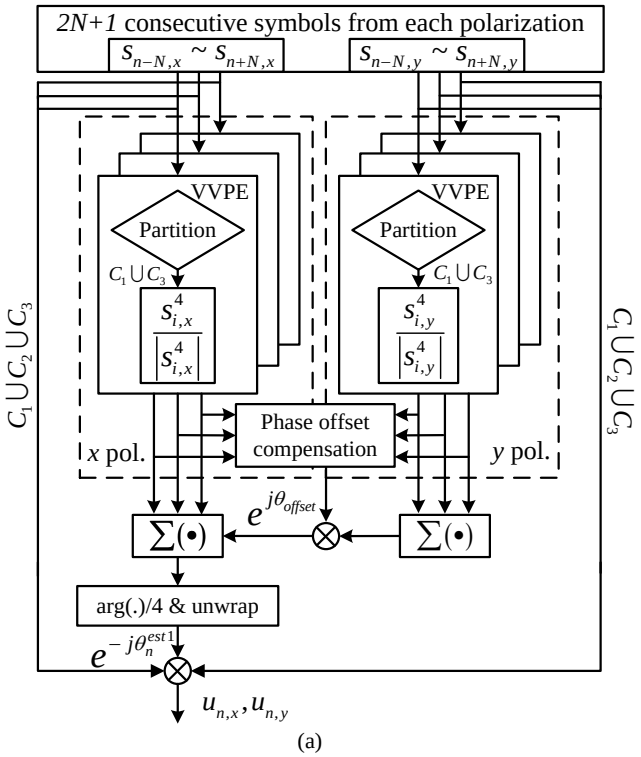

Fig. 2.1 Block diagram of the first stage estimator of the proposed two-stage CPE composed of a VVPE and a phase-offset cancellation block.

2.2.1. QPSK Partitioning for 16-QAM signals

For a 16-QAM constellation, only the part of the symbols whose modulation phases can be eliminated by raising them to the 4th power are suitable for the commonly used

Viterbi and Viterbi phase estimation (VVPE) for QPSK systems. The identification of such symbols for CPE is known as QPSK partitioning and is illustrated in Fig. 2.2 [39]. The symbols are classified into three rings (Class I (C_1), Class II (C_2) and Class III (C_3)) according to their amplitudes. In the inner and outer rings, the symbols belonging to C_1 for C_3 can be viewed as two QPSK constellation sets and their modulated phase can be eliminated by VVPE and carrier phase can be estimated [19].

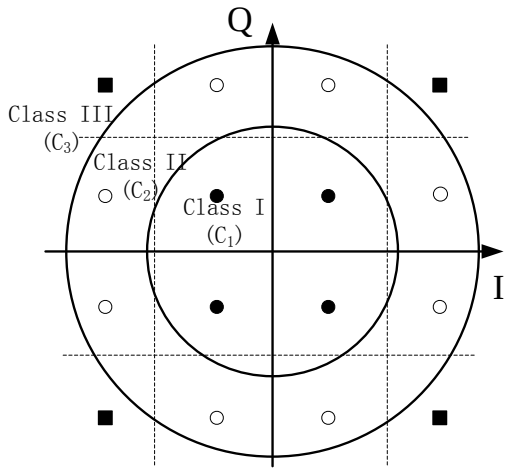

Fig. 2.2 QPSK partitioning for 16-QAM signals based on the received signal amplitude. The initial estimate of the laser phase can be obtained by VVPE for Class I and Class III symbols.

To recover the phase of the n^{th} symbol $s_{n,x(y)}$, a vector of $2N+1$ symbols $s_{n-N,x(y)}$..., $s_{n+N,x(y)}$ are first normalized and partitioned and N is referred to as the filter half width for the rest of the paper. If the symbols belong to Class I symbols (C_1) or Class III symbols (C_3), they are first selected to be processed by modified VVPE [38]. Since the outcomes of the two VVPEs from both polarizations should suffer from identical phase noise up to a constant phase offset [47], this phase offset can be easily estimated and compensated without much increase in computational complexity. The VVPE

results from both polarizations are then summed up to reduce the effect of ASE noise. The first stage carrier phase estimate θ_n^{est1} is then given by

$$\theta_n^{est1} = \frac{1}{4} \cdot arg\left(\sum_{i:s_{i,x}\in C_1 \cup C_3} \frac{s_{i,x}^4}{|s_{i,x}^4|} + e^{j\theta_{offset}} \cdot \sum_{i:s_{i,y}\in C_1 \cup C_3} \frac{s_{i,y}^4}{|s_{i,y}^4|}\right), \quad i \in \{n-N, \dots, n+N\} \tag{2.2}$$

where θ_{offset} is the phase offset estimate between two polarizations, and N is the filter half width of a sliding summing window. It should be noticed that our QPSK partitioning scheme does not require phase rotations on the Class II symbols, suggested in [39], and those symbols will be processed in a subsequent *ML* estimators instead.

2.2.2. Phase-Offset Estimation

The phase-offset results in catastrophic error when signals on both polarizations are summed up to estimate the phase noise [47]. Fortunately, this phase-offset can be interpreted by simply observing VVPE outcome difference between *x* and *y* polarizations. However, ASE noise and incorrectly partitioned symbols can severely worsen the phase offset estimates. One way of eliminating these two impairments is by using the following recursive equation [47]

$$q_k = \alpha \left[\frac{s_{k,x}^4}{|s_{k,x}^4|}\right] \cdot \left[\frac{s_{k,x}^4}{|s_{k,x}^4|}\right]^* + q_{k-1} \cdot (1-\alpha), k: \left(s_{k,x} \in C_1 \cup C_3\right) \cap \left(s_{k,y} \in C_1 \cup C_3\right) \tag{2.3}$$

$$\theta_{offset} = arg(q_k)/4 \tag{2.4}$$

where α is a constant parameter, q_k is the current phase-offset estimation. Note that the phase offset estimation technique requires received symbols from both *x* and *y*

polarizations at the same time slot to belong to C_1 or C_3, which means only 1/4 of the symbols, on average, are used to estimate θ_{offset}. As pointed out in [47], the phase-offset is a constant or slow varying value, which is much longer than estimation convergence time, so it is not unnecessary to continuously process the phase-offset estimation.

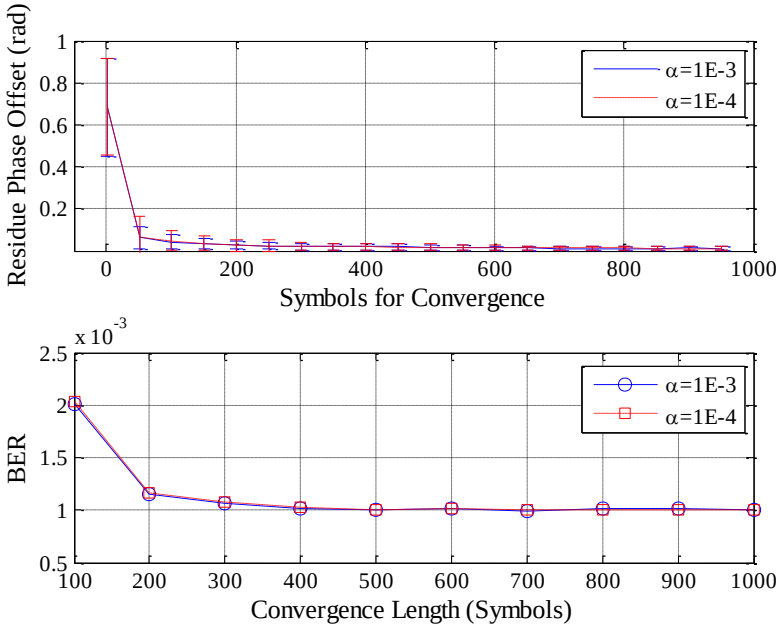

Fig. 2.3 Residue phase-offset and BER versus convergence length. Fifty trials has been performed for each point, OSNR penalty is 1dB @ BER=1e-3 & $\Delta v \cdot T_s$=2E-4.

In Fig. 2.3, both residue phase offset and BER versus convergence time are plotted. The linewidth times symbol period product and SNR was set to be 2e-4 and 17.54dB, respectively, which are the same value to achieve BER of 1e-3 when there is no phase–offset. Simulations of fifty trials with 2e18 symbols on each polarization are performed. Both the residue phase offset and BER are well converged even only after 500 symbols. Thus, it is safe to set the convergence length to be 1000 symbols. After the convergence, the slow time varying feature of phase-offset is experimentally

studied. We experimentally investigated three possible methods: 1. continuously updating θ_{offset}; 2. periodically updating θ_{offset} in a longer time slot; 3. only updating θ_{offset} at the beginning. In Fig. 2.4, method 2 updates θ_{offset} using the first 1000 symbols in every 10000 symbol block, while phase-offset is only estimated using the first 1000-symbol time slot. As shown in the inset of Fig. 2.4, the residue phase-offset is within negligible $\pm$ 1.5e-2 rad for all the three methods, which is so small that the three methods achieved the same OSNR penalty with the BER difference to be 2e-5 at maximum, as shown in Fig. 2.5. Since the performance is the same, however method 3 favors the simplest complexity, we choose to use method 3 in the rest of the paper.

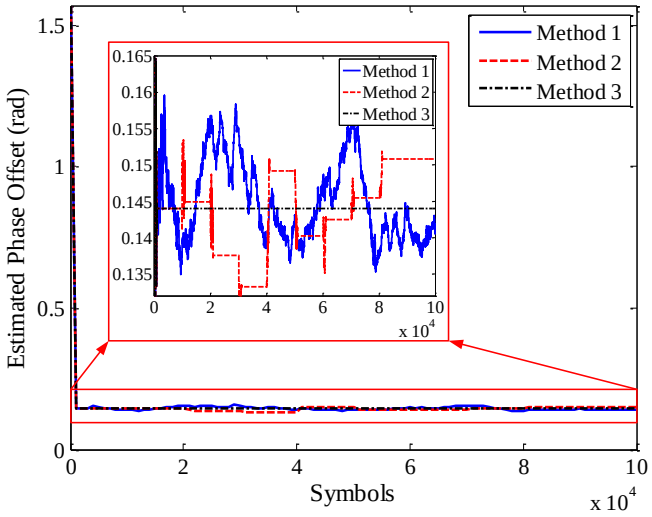

Fig. 2.4 Estimated phase offset for various methods. (Method 1: Continuous, Method 2: Periodical, Method 3: One True)

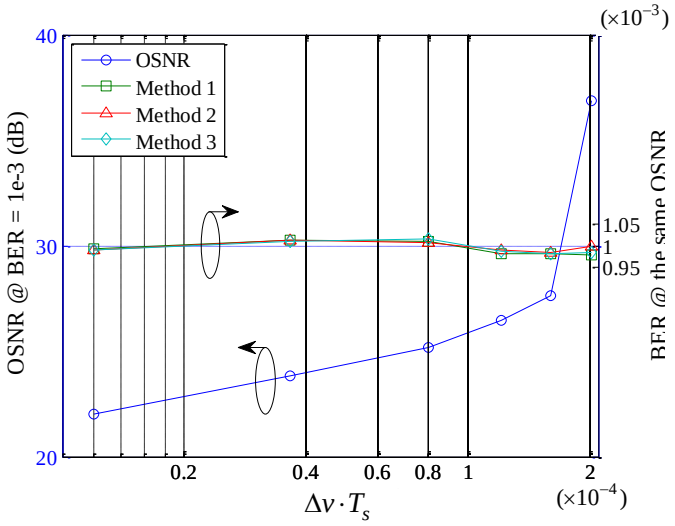

Fig. 2.5 OSNR penalty and BER versus $\Delta v \cdot T_s$

2.2.3. Maximum Likelihood Detection

After all the received symbols are compensated by the estimated phase θ_n^{est1} and θ_{offset}, they are fed into the second stage ML phase estimator. The 2nd stage of the proposed CPE is an ML estimator shown as in Fig. 2.6. The ML estimation of the carrier phase θ_n^{est2} is given by

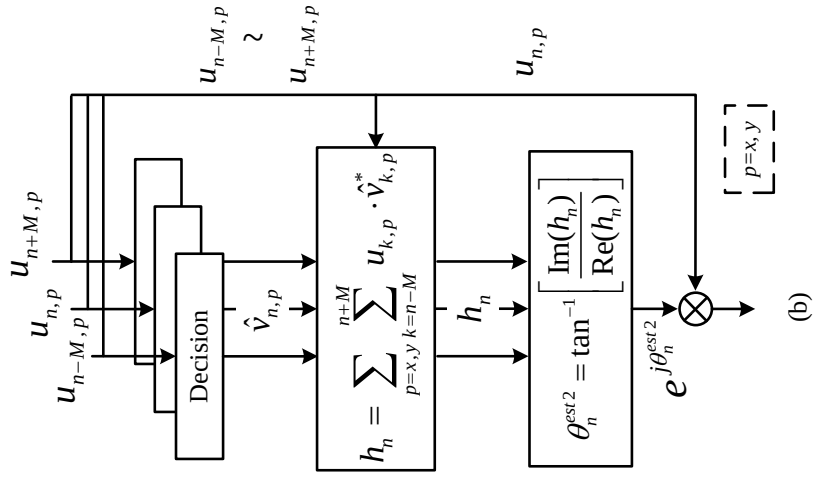

Fig. 2.6 Second stage ML estimator to improve estimation accuracy.

2.3. Simulation Results and Discussions

Simulations are conducted to study and compare the performance of the proposed CPE with others reported in the literature. In particular, 2^{18} 16-QAM symbol sequences on each polarization were used to obtain the bit error ratio (BER). The two most significant bits of each symbol are differentially encoded to avoid cycle slips [21]. The laser phase noise is modeled as a Wiener process, and different amount of ASE noise is loaded to realize different OSNRs.

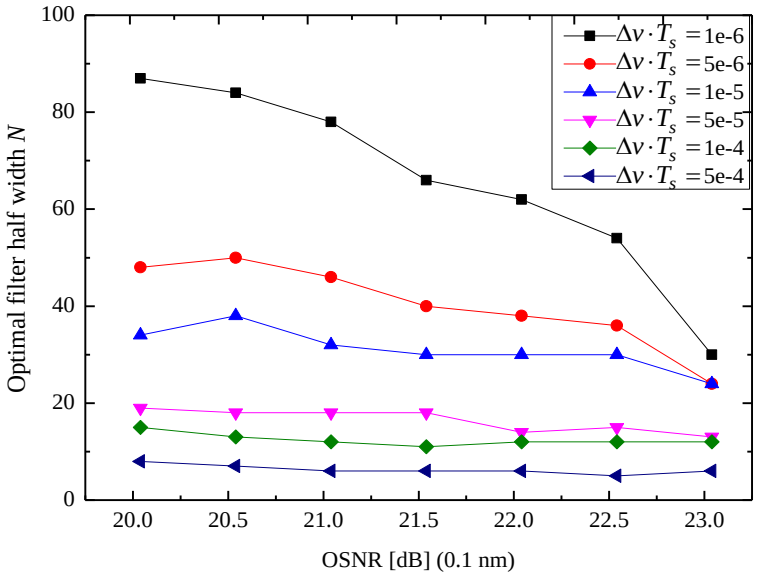

Fig. 2.7 Optimal filter half width N for the first stage estimator vs. OSNR for different linewidth times symbol duration products ($\Delta\nu \cdot T_s$). The symbol rate is 25 GBaud and each data point is obtained by averaging the result of 10 independent trials.

It turns out that for the 1st stage estimator there exists an optimal filter half width that minimizes the BER. The optimal width is determined by a trade-off between additive ASE noise and laser phase noise: A larger filter width is preferred to average out the additive noise while the de-correlation of laser phase noise over different

symbols favors a short filter width. To determine the optimal filter width, we performed extensive Monte Carlo simulations for different combination of laser linewidths and OSNR and the results are shown in Fig. 2.7. The linewidth-symbol duration product $\Delta v \cdot T_s$ ranges from 1e-6 to 5e-4 which covered the typical range of currently used lasers in long haul transmission systems. Here, Δv denotes the combined linewidths of the transmitter and receiver lasers and T_s denotes the symbol period.

Fig. 2.7 suggests that the optimum width decreases when linewidths and/or SNR get larger and vice versa, in agreement with theoretical predictions. For $\Delta v \cdot T_s$ as large as 5e-4, the optimal filter half width *N* is found to be around six and vary slightly with SNR. On the other hand, the optimal *N* becomes larger and more sensitive to ASE noise when they are dominant, e.g. the optimal *N* ranges from 46 to 91 when $\Delta v \cdot T_s$= 1e-6. For BER=1E-3 with 1dB penalty (compared to a system using perfect laser with zero linewidth and gray encoding), the filter half width is found to be *N*=12 when $\Delta v \cdot T_s$ is as large as 2E-4. Similarly, we can optimize the second-stage filter half width *M* using the same approach. However, since a considerate amount of the phase noise has already been compensated in the first stage estimator, the optimal half width *M* of the 2nd stage estimator is found to be quite insensitive to $\Delta v \cdot T_s$ and/or OSNR. Consequently, we set the optimal *N* and *M* to be 12 and 3 for all the simulation and experimental results for the rest of the paper.

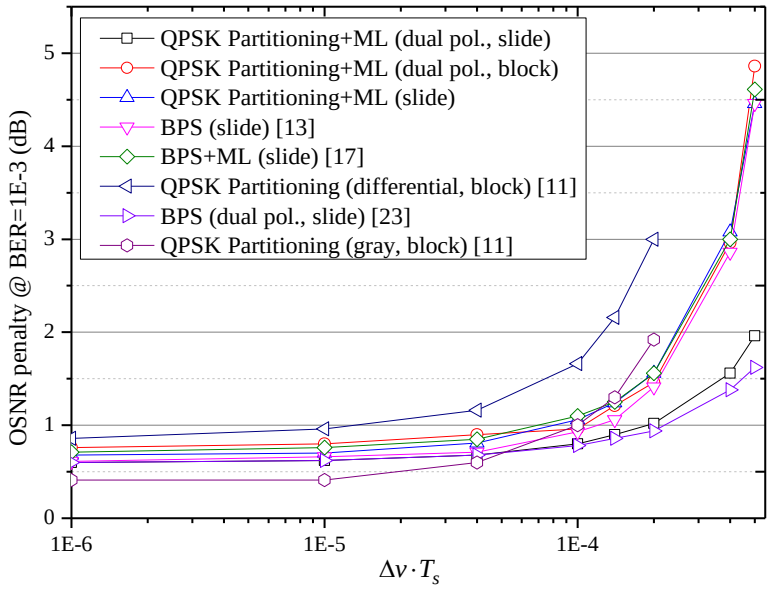

Fig. 2.8 OSNR penalties versus linewidth times symbol duration product ($\Delta v \cdot T_s$) for various feed-forward CPE techniques for 16-QAM systems.

In Fig. 2.8, various CPEs of single/dual polarization, sliding/block averaging and gray/differential encoded approaches are simulated either to be consistent with their original work or for ease of comparison. Unless specifically stated, the performances represent single polarization, sliding averaging or differentially encoded approaches. For fair comparisons, we mainly focus on sliding and differentially encoded techniques. As shown in Fig. 2.8, that our proposed algorithm can tolerate ($\Delta v \cdot T_s = 2e-4$ with OSNR penalty of 1dB.

2.4. Experimental Results

The experimental setup for the investigation of the proposed CPE for a 200 Gb/s DP-16-QAM is shown in Fig. 2.9. External cavity lasers (ECL) or distributed feedback (DFB) lasers with different linewidths ranging from 150kHz to 2.81MHz are

used to investigate the linewidth-tolerance of various CPE algorithms. The linewidths of the lasers are measured using self-heterodyne spectrum measurement technique [48]. The laser source is split and used as LO as well for self-homodyne detection. Here, a 12.5 Gb/s binary pseudo-random bit sequence (PRBS) of length 2^{15}-1 is obtained by driving an Anristu MP1763B pulse pattern generator with one RF synthesizer operating at 12.5 GHz. The signals are then split by a 3dB electrical splitter, one delay line and a 2:1 Anritsu MU182020A-013 25Gbit/s Multiplexer to generate two 25G two-level PRBS signals D and $\overline{D}$, which are further attenuated, relatively delayed and combined to generate two independent four-level signals to drive an integrated $LiNbO_3$ Mach-Zehnder (I/Q) modulator.

An erbium-doped fiber amplifiers (EDFA) and a frequency-variable band-pass filter with 1nm bandwidth followed by a second amplifier and variable attenuator were used to generate variable amount of ASE noise to realize different OSNR values. An OSNR monitoring device comprising of one PC, one polarizer and an OSA is used to monitor the OSNR. With the appropriate amount of ASE noise, the single polarization 16-QAM signal is fed into a polarization multiplexer consisting of a PBS and polarization beam combiner (PBC) and with a path length difference of 116.83ps between polarizations, corresponding to 2.92 symbol period delays. It should be noted that to resemble real transmission system, the path length difference between signals in two polarizations are chosen to be relatively short so that one can obtain statistically independent information symbols but the laser phase noise are correlated

across different polarizations. The polarization-multiplexed signals are then transmitted through 5km of SMF to de-correlate the laser phase between the transmitter and local oscillator in our self-homodyne detection scheme.

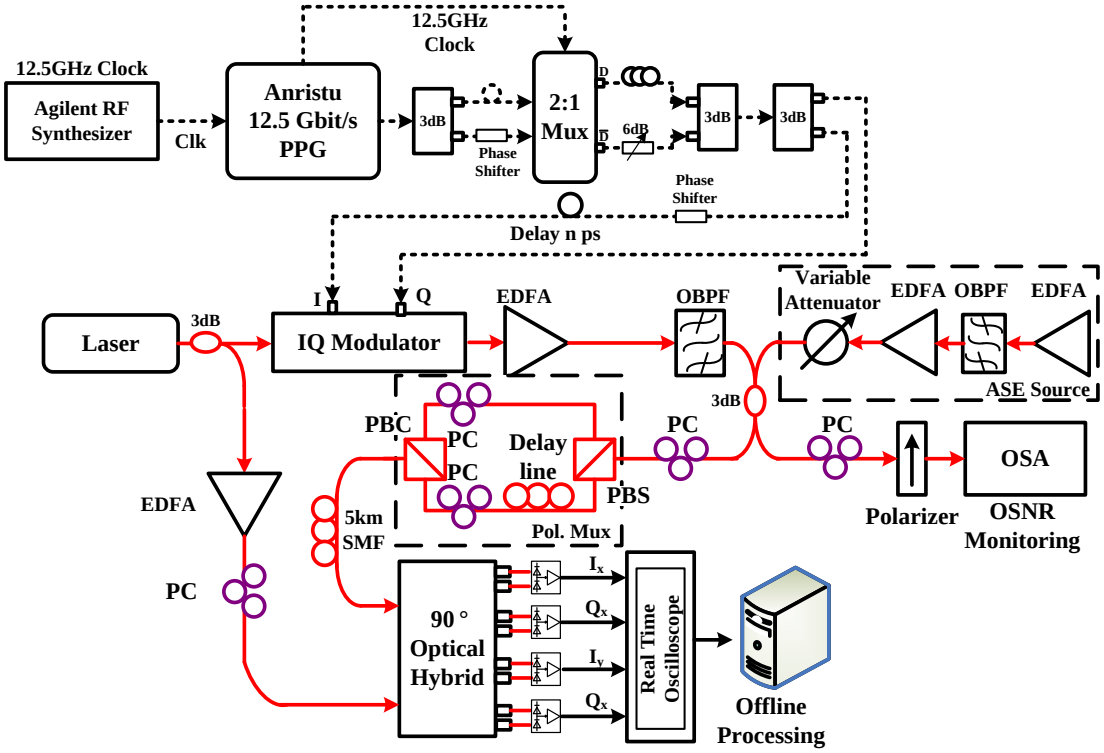

Fig. 2.9 Experimental setup for CPE performance investigation for a 200Gb/s DP-16-QAM system. The 16-QAM signal is generated by applying two four-level electrical signals to IQ modulator, which are generated by combining two 25G/s two-level signals with different amplitudes. PC: polarization controller; EDFA: Erbium-doped optical fiber amplifier; OSA: optical spectrum analyzer; OBPF: optical band-pass filter; SMF: single mode fiber; Pol. Mux: polarization multiplexer; PBS: polarization beam splitter; PBC: polarization beam combiner.

At the receiver, the dual-polarization signals are sampled by a 50G Sample/s real-time sampling scope at two samples per symbol and then processed offline by DSP. The block diagram for the DSP algorithms is shown in Fig. 2.10. The samples

are first processed with orthogonalization [49] for quadrature imbalance compensation and four fractionally-spaced (T_s/2) 13–taps time domain finite impulse response (FIR) adaptive filters for timing phase recovery, polarization de-multiplexing, DGD mitigation and down-sampled to one sample per symbol. The FIR taps are updated using the standard constant modulus algorithm (CMA), which is simple, robust, and works independent of carrier phase. Since we used a self-homodyne scheme, frequency offset compensation can be omitted. The signals are then passed into various CPE techniques followed by symbol detection and BER calculation.

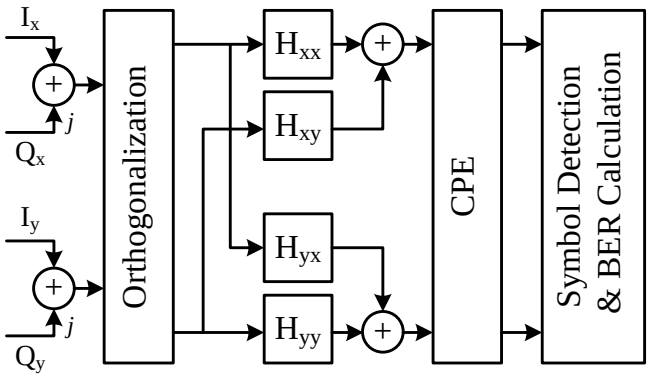

Fig. 2.10 Receiver DSP block diagram for a 200 Gb/s DP-16-QAM system using self-homodyne detection. Two samples per symbol sequences from both polarizations (I_x, Q_x, I_y, Q_y) are first fed into orthogonalization algorithms to equalize quadrature imbalance in modulator and detector imperfections, followed by a 13 taps T_s/2-spaced FIR filters for timing phase recovery and polarization de-multiplexing. The output is then down-sampled to one sample per symbol and passes into five different carrier phase estimation techniques: BPS, BPS+ML, QPSK partitioning, single and dual polarization QPSK partitioning+ML. The CPE outputs are then detected and BER is calculated.

We experimentally compare the performance of five feed-forward CPEs including

QPSK partitioning [39], single polarization BPS [21], single polarization BPS+ML [42], our proposed single polarization QPSK partitioning+ML and dual polarization QPSK partitioning+ML. For comparison, we utilized one ECL laser with linewidth of 150 kHz and five cost-effective DFB lasers with linewidths measured to be 0.45MHz, 1MHz, 1.5MHz, 2MHz and 2.81MHz [48].

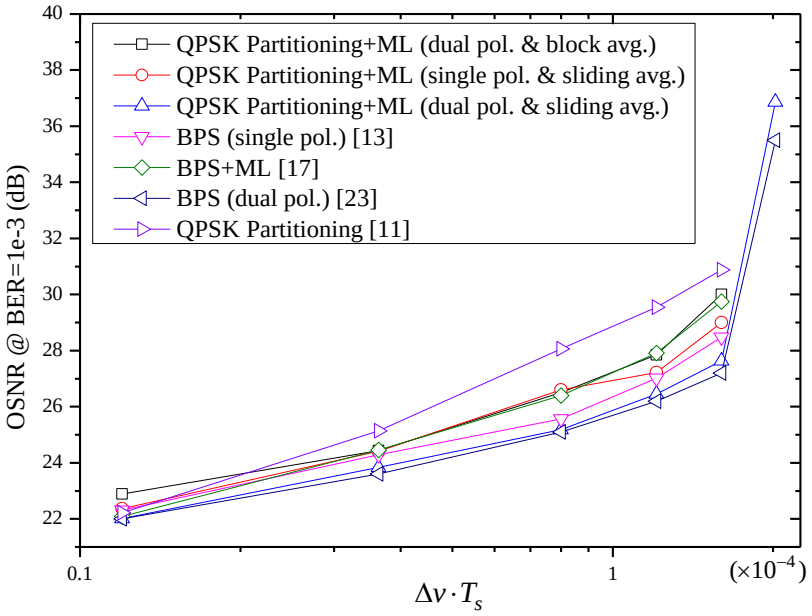

Fig. 2.11 OSNR vs. laser linewidth times symbol duration product ($\Delta v \cdot T_s$) for a 200Gb/s DP-16-QAM system obtained from experiments. The combined linewidth of the transmitter laser and local oscillator are 0.3 MHz, 0.9 MHz, 2 MHz, 3 MHz, 4 MHz, and 5.63 MHz. At large laser linewidth, a BER of 1E-3 can only be achieved by dual pol. QPSK paritioning+ML.

The OSNR penalties at BER of 1e-3 for different lasers with different linewidths are shown in Fig. 2.11. The OSNR penalties are obtained by varying the amount of ASE noise and recording the OSNR from the OSNR monitoring module when the BER equals to 1e-3. The penalty difference between BPS and dual pol. QPSK partitioning+ML increases from 0.01dB to 1.21 dB when $\Delta v \cdot T_s$ increases from

1.2e-5 to 1.7e-4. When $\Delta v \cdot T_s$ is increased to 2.25e-4 (corresponding to a combined laser linewidth of 5.63 MHz), a BER of 1e-3 can only be achieved using dual-polarization QPSK partitioning+ML and dual-polarization BPS. No other CPEs can achieve a BER of 1e-3 even at the highest OSNR (37.2dB) allowed in our setup.

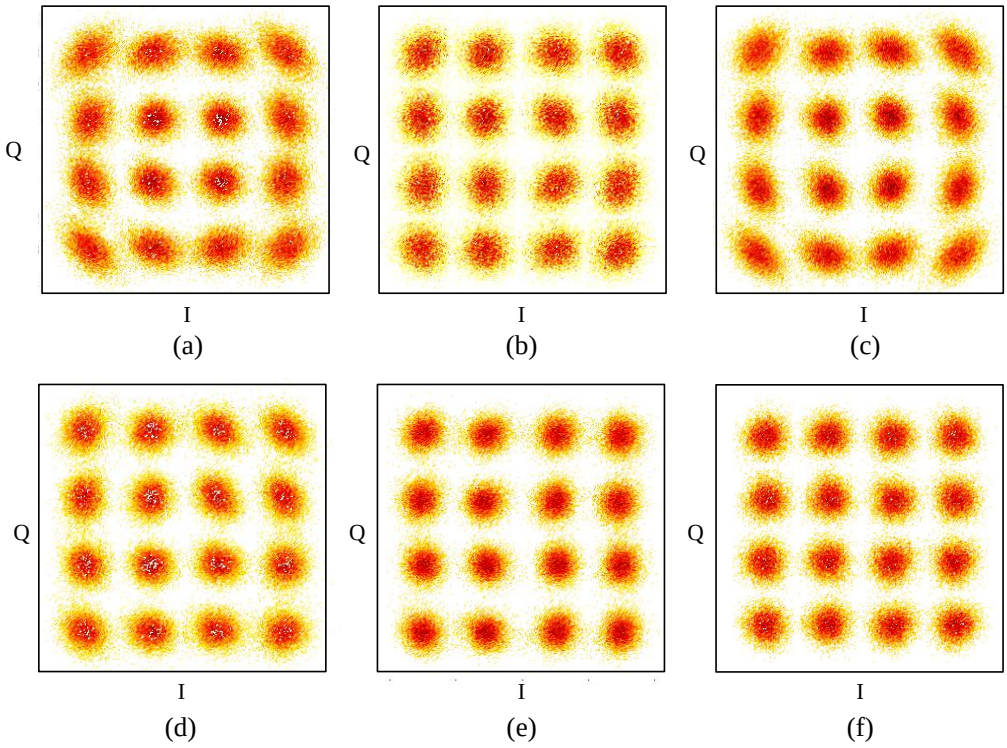

Fig. 2.12 Received signal distributions for $\Delta v \cdot T_s$ of 2.25e-4 and OSNR of 37.2 dB using (a) QPSK partitioning (BER=2.8e-3), (b) BPS (BER=1.2e-3), (c) BPS + ML (BER=1.7e-3), (d) single pol. QPSK partitioning+ML (BER=1.4e-3), (e) dual pol. QPSK partitioning+ML (BER=9.8e-4), (f) dual pol. BPS (BER=8.76e-4).

Fig. 2.12 shows the received signal distributions using various CPE techniques when the combined laser linewidth is 5.63 MHz and the OSNR is 37.2 dB. For QPSK partitioning, BPS, BPS+ML and the single polarization QPSK partitioning+ML, the received signal distributions have more residue phase noise as the outermost four distributions are more ellipse-like. On the contrary, the proposed dual polarization

QPSK partitioning+ML and the dual-polarization BPS demonstrate the good performance and result in the BER below 1e-3.

2.5. Computational Complexity

The required hardware complexity of dual/single polarization BPS, BPS/ML, two stage BPS, QPSK partitioning and the proposed method is compared. Except for the QPSK partitioning method (originally proposed as block-based algorithm), all the methods are implemented using interleaving parallel and sliding averaging scheme for ease of comparison. Block-based complexity of our proposed technique can be found in the Appendix. Here, P represents the number of parallelization paths, B is the number of trial phases for the BPS-like methods [50]. In addition, although the second-stage half filter length M is always smaller than N in the proposed CPE, we still consider the worst case scenario and set $2*M+1=2*N+1=L$, L denotes the smoothing filter length. Without losing generosity and fair comparisons, we assume the same $2P$ symbols for all the CPE techniques considered, i.e. P symbols on x polarization and P symbols on y polarization are processed. To explicitly calculate the complexity of proposed algorithm, the diagram of interleaving parallelization and sliding based averaging is plotted in Fig. 2.13.

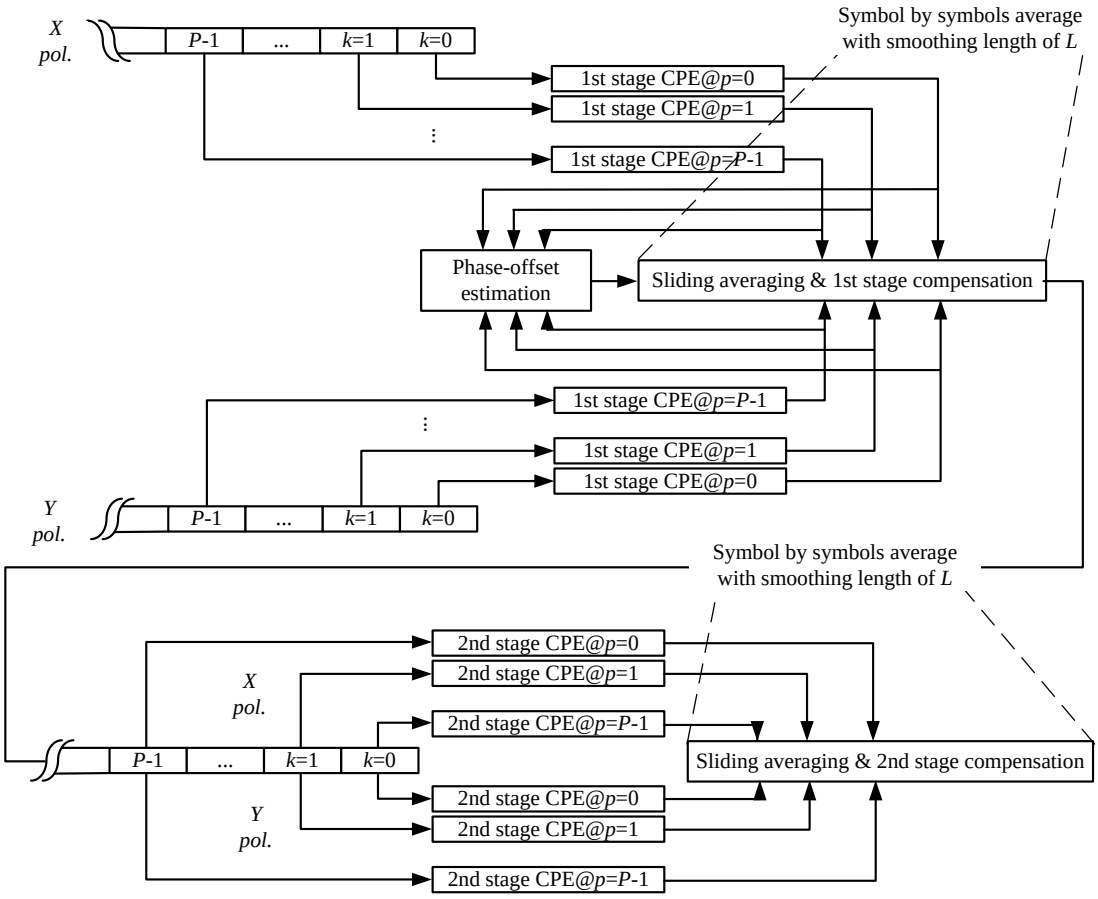

Fig. 2.13 Block diagram of sliding based dual pol. QPSK partitioning+ML CPE.

Table 2.1 shows the complexity comparisons of the various feed-forward algorithms studied in this paper. When discussing the complexity in comparison with the BPS and BPS+ML schemes, we assume B=32 and 11 test phases respectively (suggested by the original publications [21] and [42]), for 1dB sensitivity penalty at BER=1e-3. For the two-stage BPS scheme, the numbers of trial phases (B) are assumed to be 8 and 4 for the first and second estimation stages following [44]. From Table 2.1, it can be seen that for various types of operations, the proposed dual polarization QPSK partitioning+ML algorithm requires less than one third the real multipliers used in two-stage BPS [44] and BPS+ML [50] and nearly one ninth of

those used in dual polarization BPS and single polarization BPS. For other operations, the proposed technique requires much less computations than other CPEs. Although the QPSK partitioning method [39] is slightly simpler in terms of real adders, slicers, memory units and LUTs, it is evident from previous section that the performance of QPSK partitioning alone is noticeably worse than other feed-forward CPE techniques studied here.

Table 2.1 Number of operations required for various feed-forward CPE techniques

Operations	**Dual Pol. BPS**	**BPS**	**BPS+ML**	**Two-stage BPS**	**QPSK partitioning block avg.**	**Dual Pol. QPSK partitioning+ML sliding avg.**
Real Multiplier	$12BP+4P$	$12BP$	$12BP+16P$	$12BP$	$60P$	$43P$
Real Adder	$2(2L-1)BP$	$2(2L-1)BP$	$2(2L-1)BP$ $+4(L-1)P$	$2(2L-1)BP$	$3P-1$	$4LP-20P$
Slicer	$2BP$	$2BP$	$2P(B+1)$	$2BP$	$2P$	$4P$
Memory	$2LBP$	$2LBP$	$2LP(B+1)$	$2LBP$	-	$4LP$
LUT	-	-	$2P$	-	$2P+2$	$3P$
Comparators	$2P$	$2P$	$2P$	$4P$	$5P$	$3P$

LUT: look-up tables, P: number of parallel paths, L: smoothing filter length for sliding average methods, B: trial phases for BPS-like algorithms (B=32, 11 and 12 for dual/signal pol. BPS, BPS+ML and two-stage BPS).

2.6. Summary

In this paper, we proposed a low-complexity and phase noise tolerant feed-forward carrier phase estimation technique for DP-16-QAM systems using QPSK partitioning, estimation of phase offsets between signals in different polarizations, and ML detection. Convergence and time varying performance of phase-offset estimation has been studied and experimentally verified. Simulation and experimental results showed that the proposed CPE can tolerate a linewidth times symbol duration product

comparable with the best feed-forward CPE techniques while the computational complexity is at least one third time lower than the simplest feed-forward CPE reported in the literature. High performance and simple techniques will favor real-time implementation of advanced feed-forward carrier phase estimation techniques in future systems using high SE modulation formats.

Chapter 3 Modulation-Format-Independent Carrier Phase Estimation and Universal Digital Signal Processing for Elastic Optical Networks

3.1. Introduction

Extensive studies have already been conducted on feed-forward or feedback CPE for different modulation formats including QPSK [19], 16-QAM [39][51][52] and higher-order QAM signals such as 64- and 256-QAM [21][42]. On the other hand, since the future Internet traffic is expected to be much more dynamic in all aspects, research to enable flexible or elastic optical networking (EON) have recently attracted a lot of attention [25][53].

In such systems, one of the key enabling technologies is software-defined bandwidth-variable transceiver (BVT) capable of adjusting modulation formats occupying different optical spectrum [54]. In addition to adjusting among a lot of common modulation formats, BVT can be also used to generate time-domain hybrid QAM (TDHQ) to realize full rate-adaptability [55][56]. From the perspectives of receiver DSP design, a single, universal DSP platform that can accommodate all formats including TDHQ during link initialization and tracking stages is highly desired. In general, the flexible generation and reception of different modulation formats with different spectral efficiencies using a single transponder will allow one to optimize network efficiencies under dynamic bandwidth demands [57][58].

Therefore, a common digital signal processing (DSP) platform applicable to all modulation formats is instrumental and most desirable to facilitate future EON. To this end, most of the DSP algorithms in a standard coherent receiver such as blind estimation of link CD [59][60] and its compensation, frequency domain frequency offset estimation [17] and constant modulus algorithm (CMA) are modulation format independent. However, currently available carrier phase estimation techniques are quite dependent on the modulation format and can range from the simple Viterbi Viberbi phase estimation (VVPE) [19] or decision-directed phase lock loop (DD-PLL) for QPSK signals to complex multi-stage blind phase search and maximum likelihood (BPS +ML) for 64-QAM systems [42]. Therefore, it would be very desirable if a common and universal CPE can adequately function for any *M*-QAM signals.

In this thesis, we propose a modulation-format-independent or universal CPE for general square *M*-QAM systems based on a feedback architecture and derive a cost function for phase estimation update that is independent of the signal modulation format. For QPSK, 16-QAM, 64-QAM and 256-QAM signals, the proposed MFI-CPE demonstrates similar OSNR performance, and laser linewidth tolerance to a standard DD-PLL (S-DD-PLL) that requires the knowledge of the modulation format. In addition, the proposed MFI-CPE outperforms a modulation-format-oblivious (MFO)-DD-PLL that simply assumes QPSK decision rules irrespective of the actual modulation format. In addition, we first propose a joint timing phase estimation(TPE) and frequency offset estimation(FOE) algorithm based on examining the spectrum of

received signal raised to the 4^{th} power and estimating the location and phase differences between the spectral tones. The joint TPE/FOE will then be integrated with the standard Constant Modulus Algorithm(CMA) and MFI-CPE [61] to form an overall blind and universal DSP(U-DSP) platform. The blind U-DSP does not induce any overhead, can accommodate modulation formats ranging from QPSK up to 256-QAM as well as TDHQ formats, and the convergence time is comparable with other pilot symbols-based techniques. Tracking algorithms such as decision-directed(DD)-least mean squares(LMS) and DD-phase lock loop(PLL) can adequately function after initial convergence and thus the proposed blind U-DSP can be a good candidate for fast link initialization and dynamic lightpath provisioning in future flexible transmissions.

3.2. Operating Principles of Universal Carrier Phase Estimation and Digital Signal Processing

The signal recovery platform is composed of two stages: i) an initialization stage that can perform a blind, fast and universal data recovery; ii) a standard tracking stage to track the slow varying channel distortions. Here, the vital issue is how to compensate for the phase noise in the initialization stage since most of the existing CPE technologies are modulation format specific. Also, the laser phase noise changes faster than other distortions making the invention of the novel modulation-format-independent (MFI) CPE technique a necessity [61]. In addition,

we also propose a joint TPE/FOE that can be combined with other modulation-format-independent blocks such as CMA and MFI-CPE to form a blind and universal DSP configuration as shown in Fig. 3.1. In the initialization stage, the joint TPE/FOE is followed by standard CMA and then MFI-CPE for pre-convergence. In the tracking stage, we will use DD-LMS and DD-PLL for 2nd-stage convergence (if necessary), data detection and BER calculation.

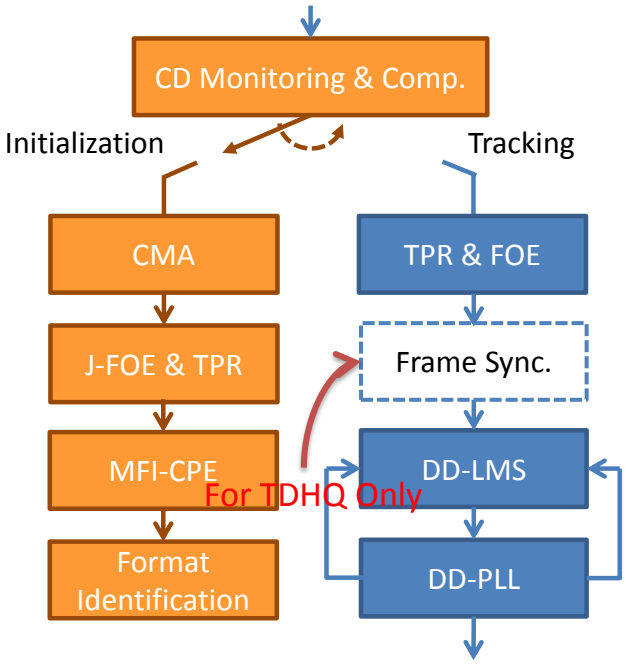

Fig. 3.1 Block diagram of the proposed blind and universal DSP for rapid link initialization.

3.2.1. Joint Timing Phase Estimation and Frequency Offset Estimation

We assume that received signals are coherently detected, sampled and first passed through DSP blocks such as front-end corrections, CD estimation [60] and compensation, which are blind and modulation-format-independent. In one

polarization, let

$$r(t) = e^{j(2\pi f_{FO} t + \phi)} \sum_l s_l p(t - lT - \varepsilon T) \tag{3.1}$$

be the equivalent continuous-time signal after CD compensation where s_l, $p(t)$, T, f_{FO}, ε and ϕ are the information symbols, pulse shape, symbol period, frequency offset, timing error and laser phase (assumed to be approximately constant over a block of symbols) respectively. The block diagram of the proposed joint TPE and FOE is shown in Fig. 3.2. The signal $r(t)$ is first up sampled to 4 samples per symbol, raised to the 4th power and undergo Fourier Transform to obtain

$$V(f) = \mathcal{F}\{r^4(t)\} = e^{j4\phi} P_4(f - 4f_{FO}) \cdot e^{j2\pi(f-4f_{FO})\varepsilon T} \cdot \left(\sum_l s_l^4 e^{j2\pi(f-4f_{FO})lT}\right) \tag{3.2}$$

where $P_4(f)$ is the Fourier Transform of $p^4(t)$. A sample spectrum of $V(f)$ is shown in Fig. 3.2 for non-return-to-zero (NRZ) pulse transmissions. Like [17], the location of the central tone can be used as a frequency offset estimate. To estimate the timing error ε, we study the phases φ_1 and φ_2 of the tones at $f = 4f_{FO}$ and $f = 4f_{FO} + 1/T$ respectively. In particular, as $p(t)$, $p^4(t)$ and hence $P_4(f)$ are real and even in any practical communication system, $\arg\{P_4(f)\} = 0$. The phases φ_1 and φ_2 are given by

$$\varphi_1 = arg\{V(4f_{FO})\} = 4\phi + arg\{\sum_l s_l^4\} \tag{3.3}$$

$$\varphi_2 = arg\{V(4f_{FO} + 1/T)\} = 2\pi\varepsilon + 4\phi + arg\left\{\sum_l s_l^4 e^{j2\pi l}\right\} \tag{3.4}$$

and hence the timing phase error can be estimated through

$$\hat{\varepsilon} = \frac{\varphi_2 - \varphi_1}{2\pi}. \tag{3.5}$$

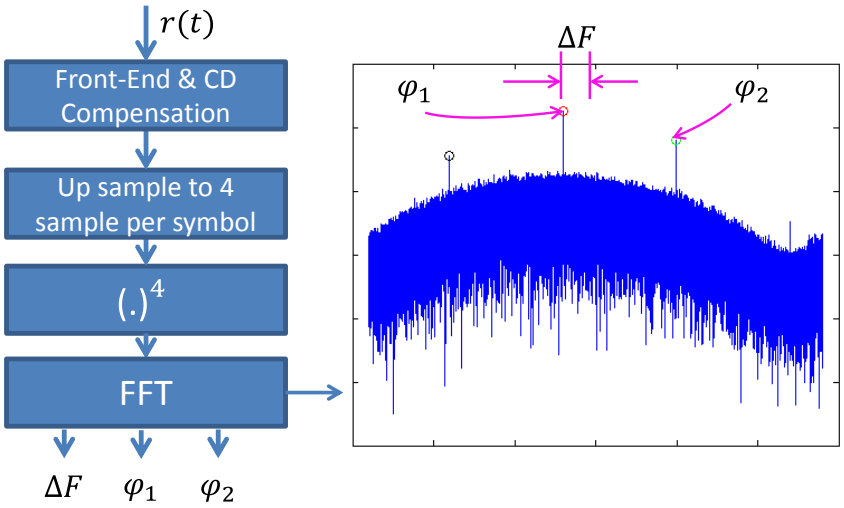

Fig. 3.2 Proposed joint TPE and FOE and the spectrum of received signal raised to the 4th power for NRZ transmissions.

3.2.2. Modulation-Format-Independent Carrier Phase Estimation for Square M-QAM Systems

Consider an *M*-QAM system where the received signal is sampled and processed in a DSP unit. For simplicity purpose, we assume that all linear impairments, such as chromatic dispersion, timing error, polarization impairments and frequency offset are assumed to be perfectly compensated before carrier phase estimation. The n^{th} input signal to the CPE can be expressed as

$$r(n) = s(n) \cdot e^{j\theta(n)} + z(n) \tag{3.6}$$

where $s(n)$ denotes *M*-QAM signals, $\theta(n)$ is the combined transmitter and receiver phase noise and $z(n)$ models the collective ASE noise following complex circularly symmetric Gaussian random process. The power of $r(n) = s(n) \cdot e^{j\theta(n)} + z(n)$ is assumed to be normalized to 1 for simplicity. The laser phase noise is typically

modeled as a Wiener process with a variance $\sigma^2 = 2\pi\Delta v T_s$ where T_s is the symbol period, and Δv is the combined linewidth of the transmitter laser and local oscillator at the receiver.

An important task in the estimation of $\theta(n)$ is to remove the phase of the data. Applying a power law nonlinearity [19][39][51] or decision-directed phase estimates [21][52] are two common techniques used to eliminate the signal modulation phase. The block diagram of standard decision-directed phase lock loop (S-DD-PLL) for carrier phase estimation in [52] is given in Fig. 3.3. The decision-directed carrier recovery loop uses the error between the output of the equalizer and the corresponding decision and the phase update equation is given by

$$\hat{\theta}(n+1) = \hat{\theta}(n) - \mu \cdot Im[y(n)e^*(n)] \tag{3.7}$$

where μ is the step-size parameter, $e(n)$ is the error signal and $y(n)$ is the symbol to be decided given by

$$e(n) = y(n) - \hat{a}(n) \tag{3.8}$$

and

$$y(n) = r(n) \cdot e^{-j\hat{\theta}(n)} \tag{3.9}$$

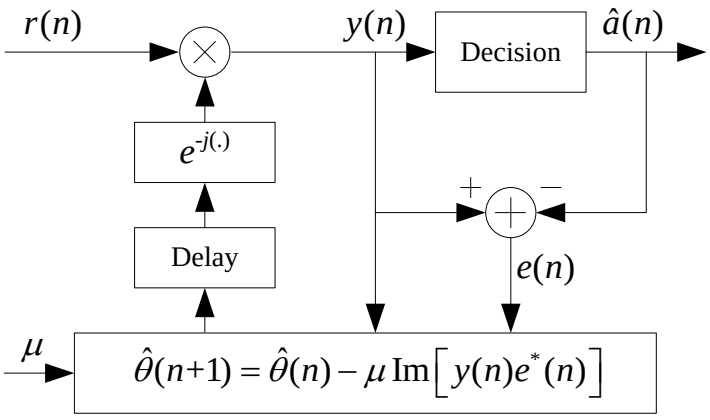

Fig. 3.3 Block diagram of the standard decision-directed phase-lock-loop (S-DD-PLL) for carrier phase estimation.

The S-DD-PLL gives an accurate carrier phase estimate but similar to the majority of feed-forward CPE techniques, requires a-priori knowledge of the modulation format so that the decision blocks can function properly.

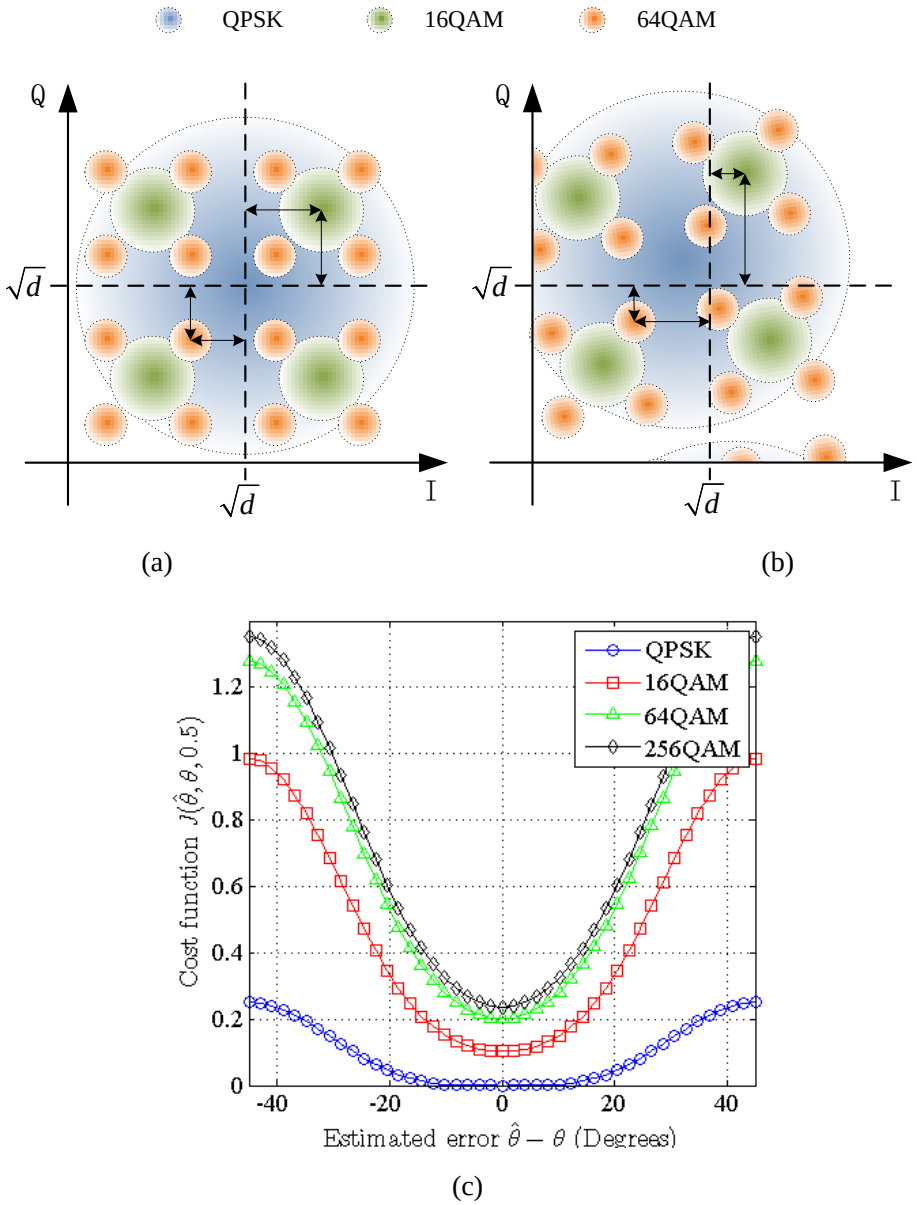

Fig. 3.4 Normalized *M*-QAM constellation and its distance from the 'center of gravity' *d* for MFI-CPE when the phase estimation error is (a) $\hat{\theta} - \theta = 0$.(b) $\hat{\theta} - \theta = 10^{\circ}$. Noted is

that the different signals have common signal power but different central point. (c) Cost function $J\left(\hat{\theta},\theta,0.5\right)$ versus phase estimation error $\hat{\theta}-\theta$.

In contrast, to facilitate modulation format independent or universal CPE, one would need to derive a cost function and the corresponding phase update equation that is common to all modulation formats and optimized when the phase estimate $\hat{\theta}$ approaches the true phase θ. If we assume that only square-shaped constellation formats such as QPSK, 16-QAM, 64-QAM and above are used in practice, the only information to the U-CPE is that incoming signal should have a common square-shaped constellation. In this case, we study the real and imaginary part of the received signal $y_R = \mathrm{Re}\{y(n)\}$ and $y_I = \mathrm{Im}\{y(n)\}$ and consider the cost function

$$J\left(\hat{\theta},\theta,d\right) = E[((|y_R|^2 - d)^2 + (|y_I|^2 - d)^2)^2] \tag{3.10}$$

where d somewhat represents the 'center of gravity' of the constellation in one quadrant as depicted in Fig. 3.4(a) and (b). Now, for a given information symbol, one can show that

$$\frac{\partial}{\partial d}((|y_R|^2 - d)^2 + (|y_I|^2 - d)^2) = 0 \;\Rightarrow d = 0.5 \tag{3.11}$$

i.e J is minimized $d = 0.5$ irrespective of modulation format and estimation error $\hat{\theta}-\theta$. Furthermore, as shown numerically in Fig. 3.4(c), $J\left(\hat{\theta},\theta,0.5\right)$ is minimized at $\hat{\theta}-\theta = 0$ irrespective of the modulation format, thus illustrating that $J\left(\hat{\theta},\theta,0.5\right)$ will be a suitable cost function to realize U-CPE. In this case, the corresponding phase update equation is given by

$$\hat{\theta}(n+L) = \hat{\theta}(n) - \frac{\mu}{2}\frac{\partial J(n)}{\partial \hat{\theta}(n)} =$$

$$\hat{\theta}(n) - \mu[(|y_R|^2 - d)^2 + (|y_I|^2 - d)^2]y_R(n)y_I(n)[y_R(n)^2 - y_I(n)^2] \quad (3.12)$$

where the μ, ε and L are step size, error signal and feedback loop delay respectively. The block diagram of proposed U-CPE technique is depicted in Fig. 3.5.

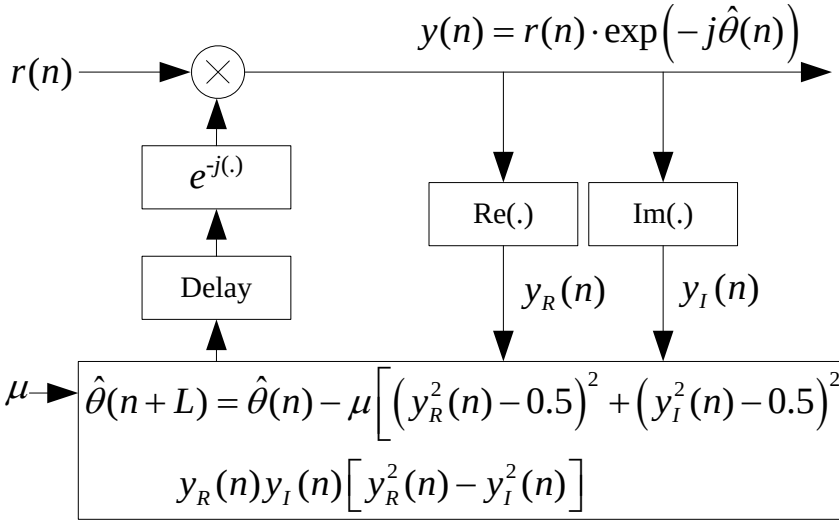

Fig. 3.5 Block diagram of the proposed U-CPE. The 'Delay' block represents the total number of symbol delays L due to possible number of parallelization paths [62] multiplied by number of clock cycles needed for phase estimations.

3.3. Simulation Results

Fig. 3.6 and Fig. 3.7 show the FOE and TPE performance for 16-QAM signals at 20 dB OSNR. 4096 samples are used to generate $V(f)$ and the transmitter and receiver linewidth is 100 kHz. The frequency offset and timing phase can be accurately estimated with residual frequency error as low as 1 MHz. Similar performance can be achieved for other modulation formats as well. To improve its tolerance and robustness to polarization and PMD effects, one can process $r_x(t) + r_y(t)$ and $r_x(t) + jr_y(t)$ in addition to $r_x(t)$ and $r_y(t)$ [63] to identify the polarization state that gives the most prominent tones in $V(f)$ for TPE and FOE. The robustness is

evident from Fig. 3.6 and Fig. 3.7 as different angles between signal PSP and polarization axis and different differential group delay(DGD) gives nearly identical FOE and TPE results.

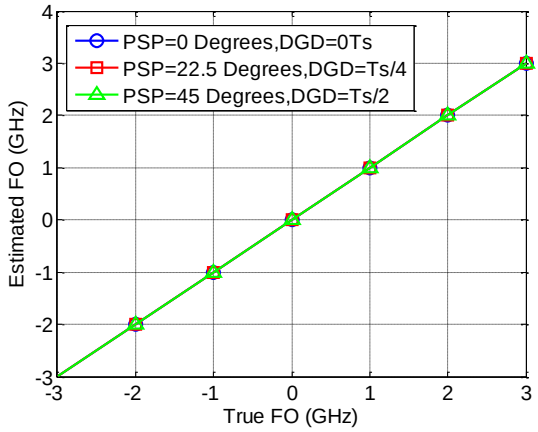

Fig. 3.6 Estimated vs. true timing phase offsets.

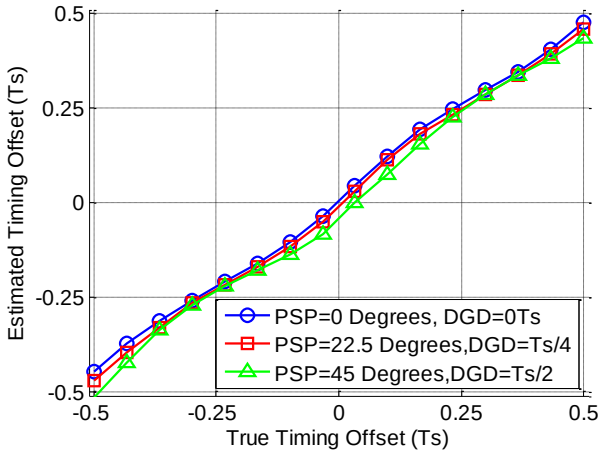

Fig. 3.7 Estimated vs. true frequency offset for 16 QAM signals for difference signal polarization states.

The performance of the proposed U-CPE is studied through simulations and compared with S-DD-PLL in which the decision process assumes the knowledge of the modulation format and MFO-DD-PLL in which QPSK decision process is used irrespective of the actual modulation format of the input signal. In particular, 10×2^{18} symbol sequences were used to calculate the bit error ratio (BER) for 28 Gbaud/s

QPSK, 32 Gbaud/s 16-QAM and 32 Gbaud/s 64-QAM systems and the BER vs. OSNR (in dB/0.1nm) are shown in Fig. 3.8 using the three CPE techniques concerned. The combined laser linewidths are selected as practical values, that is 1MHz for QPSK, 500kHz for 16-QAM and 100kHz for 64-QAM. The two most significant bits of each symbol are differentially encoded to avoid cycle slips and different amount of ASE noise is loaded to realize different OSNRs. The feedback delay L is set to be 10. It is obvious from the figure that U-CPE performs better than MFO-DD-PLL but not as good as S-DD-PLL. This is to be expected as S-DD-PLL does assume the knowledge of modulation format. For a hard-decision-forward error correction(FEC) threshold of 1E-3 and soft-decision(SD-FEC) threshold of 2E-2, U-CPE incurs penalty of less than 1.5dB compared with S-DD-PLL while MFO-DD-PLL requires an additional OSNR of 10.1 to more than 2 dB for 16- or 64-ary QAM signals with BER larger than 1e-3.

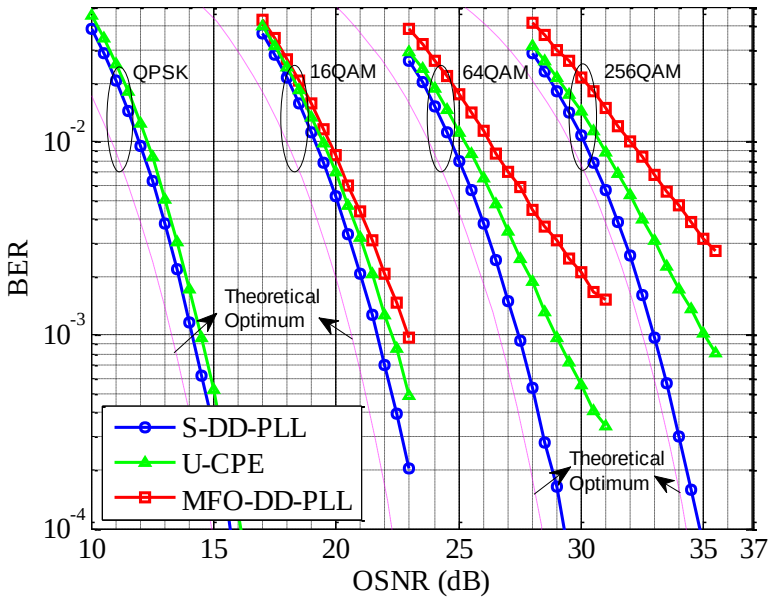

Fig. 3.8 BER vs. OSNR for QPSK, 16-QAM and 64QAM signals. Combined laser

linewidth are 1MHz for QPSK, 500kHz for 16-QAM and 100kHz for 64-QAM signals. The feedback delay *L* is set to be 10.

The OSNR penalties for 28GBaud/s QPSK systems with different linewidths and feedback delays using S-DD-PLL and the proposed U-CPE are shown in Fig. 3.9. For 1dB OSNR penalty, S-DD-PLL can tolerate linewidths of 5.5MHz, 1.4MHz and 350 kHz when the feedback loop delay is 1, 10 and 50 symbols respectively while U-CPE can only tolerate linewidths of 1MHz, 420kHz and 150 kHz for the same feedback delays. This is most likely attributed to the fact that the cost function used in S-DD-PLL assumes the knowledge of the modulation format and therefore is more direct and give better performance while the cost function $J(\hat{\theta},\theta)$ used in U-CPE needs to incorporate a wide range of modulation formats. Noted is that the shortest feedback loop delay can be reduced to 5 for both methods by using superscalar technique [62].

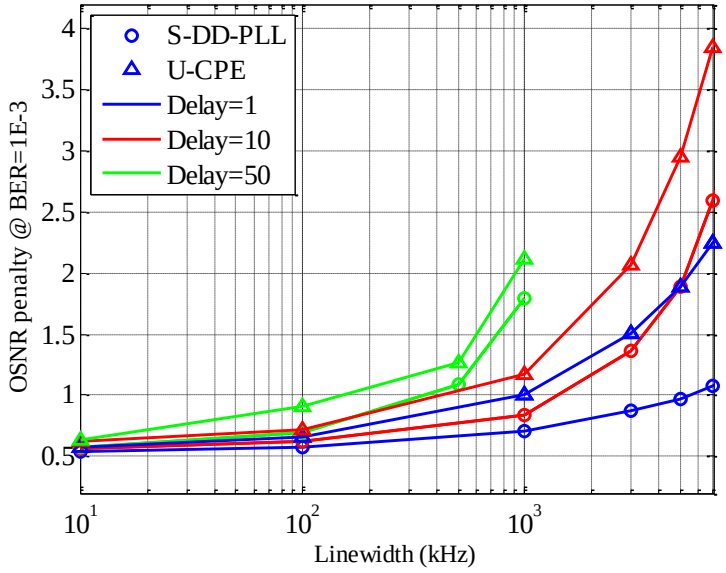

Fig. 3.9 OSNR penalty vs. laser linewidth for 28GBaud/s QPSK systems using S-DD-PLL and U-CPE for different feedback delays

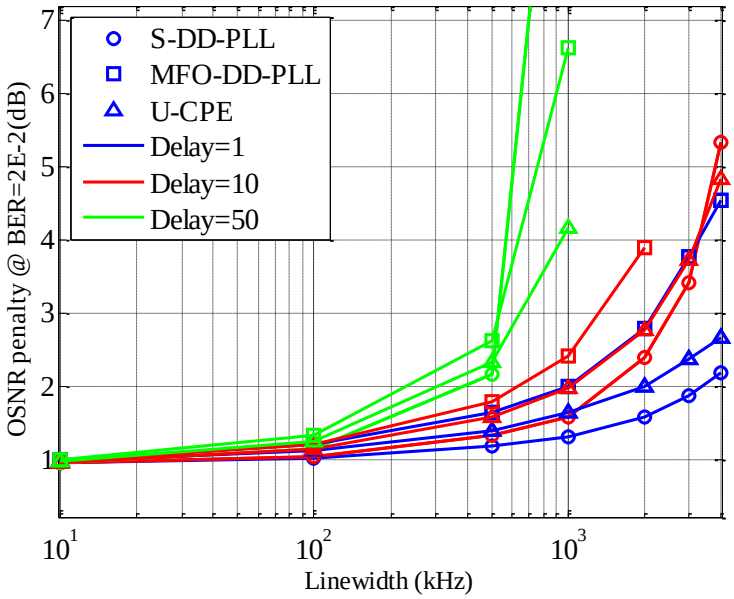

Fig. 3.10 OSNR penalty vs. laser linewidth for 32GBaud/s 16-QAM systems using S-DD-PLL, U-CPE and MFO-DD-PLL for different feedback delays

The performance and OSNR penalties of S-DD-PLL, U-CPE and MFO-DD-PLL for 16-QAM systems are shown in Fig. 3.10 for SD-FEC threshold of 2E-2. For feedback delay of 1, 10 and 50 symbols and 2 dB OSNR penalty, S-DD-PLL can tolerate linewidths of 3.38MHz, 1.43MHz and 390kHz, U-CPE can tolerate 2.03MHz, 1.02MHz and 310kHz while those of MFO-DD-PLL are 1MHz, 640kHz and 230kHz. For all the linewidths and delay time combination, the OSNR penalties of U-CPE are always below 0.5 dB comparing with S-DD-PLL while those of MFO-CPE become larger with increased linewidth and delay time. To be noted is that U-CPE even outperforms S-DD-PLL in the case when linwidth is larger than 1.4MHz (Delay=10) and 1MHz (Delay=50).

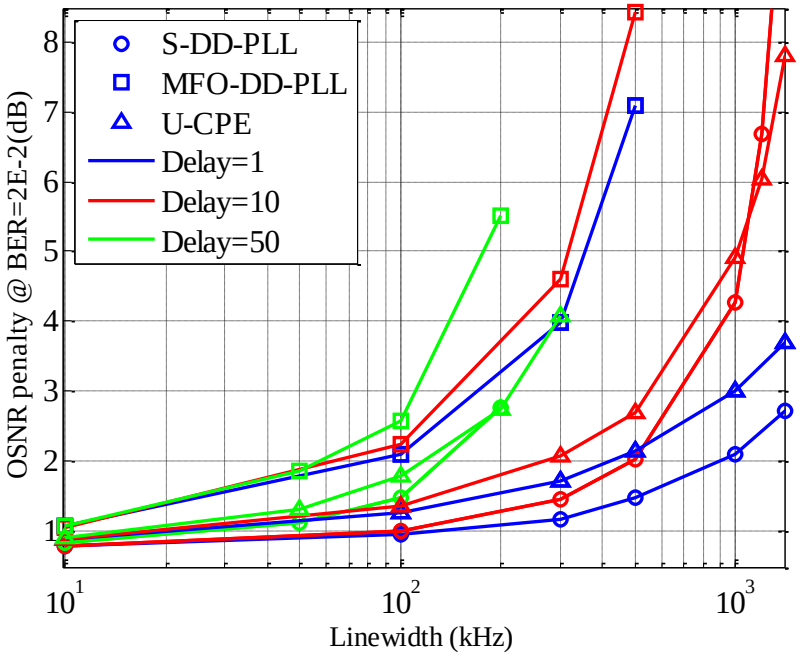

Fig. 3.11 OSNR penalty vs. laser linewidth for 32GBaud/s 64-QAM systems using S-DD-PLL, U-CPE and MFO-DD-PLL for different feedback delays.

For 64-QAM systems, U-CPE can tolerate up to 420kHz, 270kHz and 120 kHz linewidth when the feedback delay is 1, 10 and 50 symbols respectively while those of MFO-DD-PLL are 80kHz, 60kHz and 55kHz as shown in Fig. 3.11. The OSNR penalties of U-CPE are below 1 dB comparing with S-DD-PLL while those of MFO-CPE exceed 1dB when the combined linewidths is larger than 100kHz for all three delay lengths. Similar to the 16-QAM cases, if we increase linewidth larger than 1.2 MHz (Delay=10) or 200kHz (Delay=50), OSNR penalty of U-CPE become even smaller than S-DD-PLL. The overall performance results indicate that with a fairly small penalty, the proposed modulation-format-independent U-CPE performs closely with S-DD-PLL that requires the knowledge of the modulation format. The tolerable linewidths of the proposed U-CPE are summarized in Table 3.1 for various modulation formats and feedback delays.

Table 3.1 Linewidth tolerances for 2 dB OSNR penalty (1 dB for QPSK system) of the proposed U-CPE for 28 GBaud/s QPSK and 32GBaud/s 16- and 64- QAM systems.

	QPSK(28GBaud/s)	**16-QAM(32GBaud/s)**	**64QAM(32GBaud/s)**
Delay L=1	1MHz	2.03MHz	420 kHz
Delay L=10	420kHz	1.02MHz	270 kHz
Delay L=50	150kHz	310 kHz	120 kHz

We then study the performance of the three methods in presence of nonlinear effects. Without loss of generosity, we study 64-QAM signal for example. The signals is launched into a 4×80km standard single mode fiber with nonlinear index of 2.6^{-20}. After reception with coherent receiver, the digitized signal is processed with chromatic dispersion compensation, 31-taps butterfly filters updated with constant modulus algorithm and the three CPE algorithm mentioned above. The output is evaluated by counting BER using Monte Carlo method. Fig. 3.12 illustrates the launch power versus BER. The maximum launch power are 2.19, 3.15 and 3.4 dBm for Blind PLL, U-CPE and S-DD-PLL at BER=2e-2.

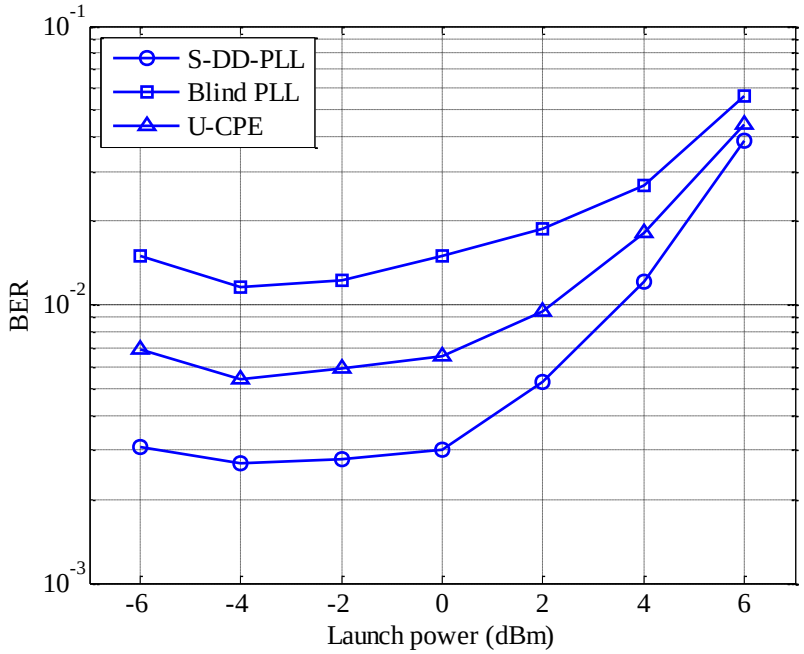

Fig. 3.12 Launch power vs. BER for 64-QAM system. Linewidth is 100 kHz.

Another issue of CPE algorithms are their computation complexity. The operations needed by U-CPE is 12 real multipliers, 6 real adders comparing with S-DD-PLL's 7 real multipliers, 5 real adders and 2 decision blocks. Although the complexity is roughly two times that of S-DD-PLL, it is negligible considering the resources occupied by CD compensation or other feedfoward CPEs.

The back-to-back performance of the proposed blind U-DSP for various modulation formats are shown in Fig. 3.13. Around 4000 symbols are used for the blind U-DSP to converge before BER calculation. An additional 1000 symbols for DD-LMS/DD-PLL refines the filter taps and BER especially for 64-QAM signals and above. In total, the blind U-DSP enables receiver DSP initialization in merely around 5000 symbols for any modulation format. The results presented here represent worst case scenarios with timing error of $\varepsilon = T/4$, half-symbol period DGD and 45 degrees

between signal PSP and polarization axis and similar results are obtained for other timing errors and polarization states.

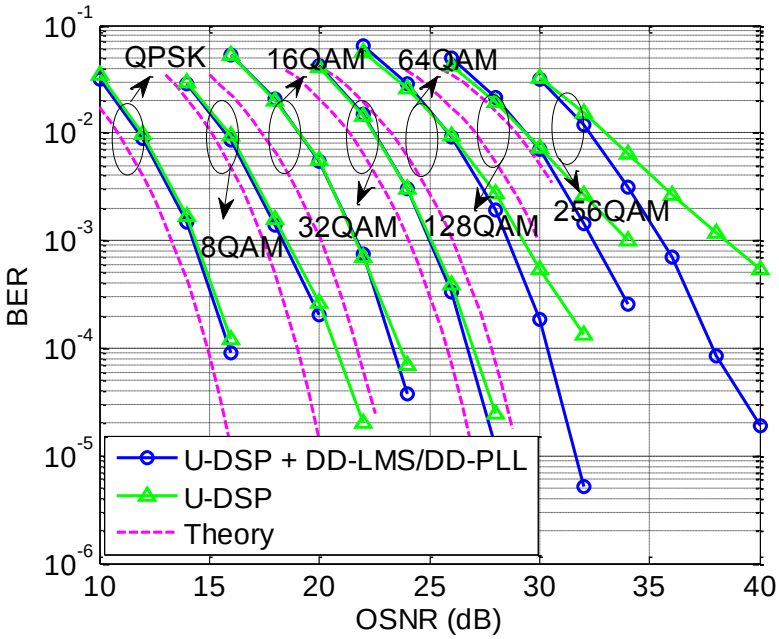

Fig. 3.13 BER vs. OSNR for various modulation formats using the blind U-DSP

3.4. Experimental Results

Fig. 3.14 shows the schematic of the experimental setup. Two high speed Micram DACs with 6 bit resolution together with two field-programmable gate array (FPGA) boards were used to generate the electrical TDHQ signals. We conducted transmission of 28 Gbaud NRZ signals applicable in the current 50 GHz ITU grid based systems. The DACs were operated with one sample per symbol, i.e., 28 GS/s, and one external cavity laser (ECL) was used as the light source for IQ modulation. The modulated optical signal was then passed through a PBS and a PBC with one branch delayed in-between for a full de-correlation of the dual-polarization signal. After being boosted, the signal was launched into a re-circulating loop, which consisted of four

spans of 80 km standard single-mode fiber (SSMF) and four erbium-doped fiber amplifiers (EDFA). At the receiver, a 0.4 nm optical filter and an ECL were tuned to coherently receive the signal, followed by two real-time scopes with 80 GS/s sampling rates to digitize the four-channel signals for offline processing.

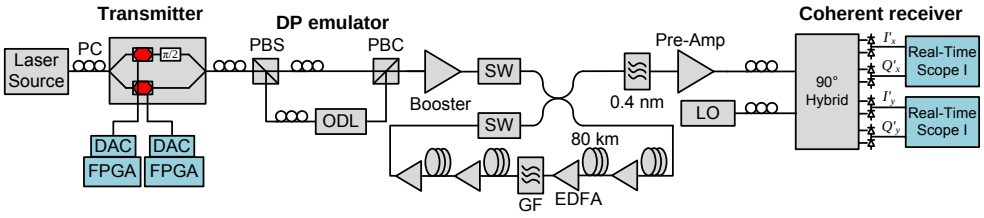

Fig. 3.14 Experimental setup for TDHQ transmission. ODL: optical delay line; PC: polarization controller; SW: switch.

Fig. 3.15 shows BER vs. OSNR for QPSK/8-QAM (2.5 bits/symbol) and 8-QAM/16-QAM (3.5 bits/symbols) TDHQ transmissions for various transmission distances using the proposed blind U-DSP + DD-LMS/DD-PLL and training symbols(TS)-LMS + DD-LMS/DD-PLL. The method in [60] is used for CD estimation and for each transmission distance, the proposed blind U-DSP can successfully initialize the receiver and the final BER performance is identical to training symbol (TS)-LMS with DD-LMS/DD-PLL for 2^{nd}-stage convergence and subsequent tracking. Furthermore, both the proposed blind U-DSP + DD-LMS/DD-PLL and the TS-based technique requires 4096 symbols for convergence, thus suggesting that the proposed blind U-DSP can be used for fast link initialization even for TDHQ transmissions.

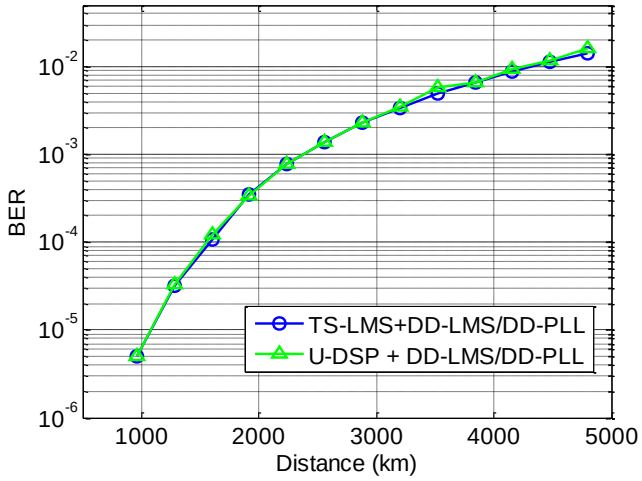

Fig. 3.15 BER vs. distance for 28Gbuad QPSK/8-QAM TDHQ.

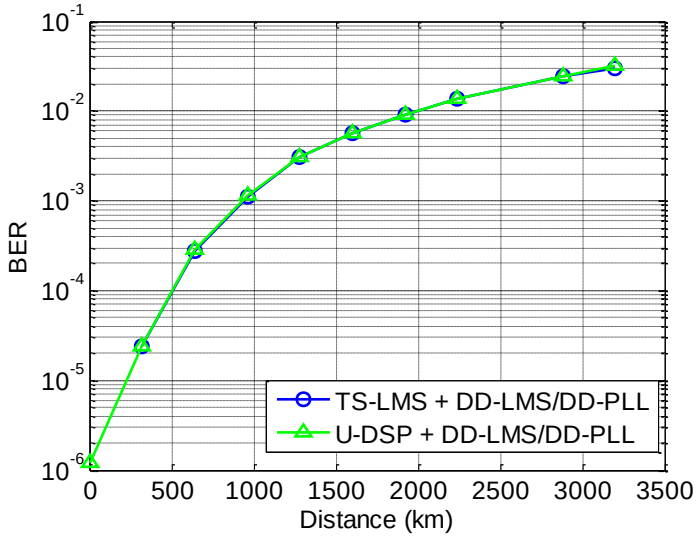

Fig. 3.16 BER vs. distance for 28 Gbuad 8-QAM/16-QAM TDHQ transmissions.

3.5. Summary

In this paper, we proposed a modulation-format-independent or universal CPE (U-CPE) technique based on a feedback architecture with a cost function for phase estimation update suitable for all square-shaped constellations. Comparing with the standard S-DD-PLL, the proposed U-CPE only require less than 1dB OSNR penalty to achieve the same BER for various formats up to 256-QAM. For different feedback

delays and laser linewidths, it is shown that the proposed U-CPE performs closely with S-DD-PLL and gives distinctively better results compared with a DD-PLL without prior knowledge of the modulation format. We also proposed a joint TPR and FOE that is combined with modulation-format-independent CPE to form a blind and universal DSP platform applicable to arbitrary modulation formats and TDHQ transmissions. The initialization time for the blind and universal DSP is comparable with other techniques using training symbols. The proposed blind U-DSP can be used for rapid link initializations in future EONs.

Chapter 4 Non-data-aided and Universal Cycle Slip Detection and Correction for Coherent Communication Systems

4.1. Introduction

Over the past few years, numerous digital signal processing (DSP) techniques have been developed to estimate and recover the laser phase for QPSK, 16-QAM systems and beyond. However, most CPE techniques suffer from the problem of cycle slips (CS) in which the received signal are phase rotated by integer multiples of $\pi/2$ and can potentially lead to catastrophic detection errors.

To cope with this problem, one can use differential encoding where information is encoded in the difference between neighboring bits/symbols. On the other hand, as soft decision-forward error correction (SD-FEC)-based transmission system become the standard choice for systems beyond 100Gb/s, differential encoding is not preferred as it induces an extra OSNR penalty for signals entering into the SD-FEC decoder [37][64][65]. To this end, turbo decoding was proposed to reduce the extra differential encoding penalty [66]. However, it was also shown that the correction capability of FEC depends on the CS occurrence probability. For example, turbo decoding exhibits an error floor when CS probability exceeds 10^{-4} and might cause total decoder failure.

Alternatively, numerous other differential-encoding-free techniques were proposed which basically involves either inserting pilot tones or pilot symbols at

regular intervals [67][68]. Pilot symbols are slightly easier to be incorporated while inserting pilot tones may require additional transmitter complexity and inevitably sacrifices signal power. However, trade-off has to be made between CS robustness and spectral efficiency. In most recent high SE system demonstrations, the amount of pilot symbols are kept sufficiently low to minimize the impact to SE, rendering the system susceptible to burst errors and hence require more robust FECs with increased code interleaving depth [69]. Several pilot-aided CPEs have already been modified in an attempt to mitigate the CS-induced burst-error impact [70][71][72]. In addition, a fully blind or non-data-aided CS compensation technique has recently been proposed by using block polarization coding which, however, is only applicable to BPSK systems [69]. This is becoming a serious drawback as optical communications are moving towards flexible transmissions and elastic optical networks(EON) which simultaneously support signal transmissions with multiple modulation formats. Modulation-format independence or universality has become an important attribute to any digital signal processing(DSP) algorithm in next generation transceivers [73]. Thus, it would be highly desirable to have a non-data-aided and universal CS detection and correction technique with minimal additional transceiver complexities.

In [74], we have proposed a blind CS detection and correction (CS-DC) technique that can be appended to any CPE algorithm. The CS-DC examines the sliding average of twice estimated phase noise $e^{j2\hat{\phi}}$ and it is shown numerically that the magnitude of such average undergo an abrupt drop when CS occurs. Therefore, locating the abrupt

drops and studying the corresponding phase evolution at that time allow one to detect and correct CS. In this thesis, we extend our investigation and analytically derive the probability density function of the sliding average, which allow us to optimize the sliding window length and threshold for CS detection. Simulation results show that even for unrealistic long-haul systems with high nonlinearity, the proposed CS-DC can substantially reduce the CS probability in both single carrier and Nyquist wavelength division multiplexing (WDM) systems. Furthermore, we show that cascading a second stage of CS-DC can successfully detect and correct multiple cycle slips that are close to each other and further reduce the CS probability by at least one order of magnitude. In the end, the tolerance of CS-DC to residue frequency offset (FO) is also studied. The proposed CS-DC is simple, non-data-aided and universal and can be used in conjunction with turbo differential decoding [66] or other pilot symbol/tone based techniques to mitigate CS to the largest possible extent.

4.2. Principle of Non-data-aided and Universal Cycle Slip Detection and Correction

Consider a digital coherent system using QPSK, 16-QAM or other common single-carrier modulation formats. For simplicity purpose, we neglect fiber nonlinearity and WDM effects and assume that linear transmission impairments such as chromatic dispersion and polarization-mode dispersion has been compensated by appropriate signal processing algorithms preceding the CPE. With symbol-rate

sampling, the i^{th} signal in one polarization going into the CPE unit of the overall DSP platform is given by

$$r_i = s_i e^{j\varphi_i} + n_i \tag{4.1}$$

where s_i denotes the information signal, φ_i is the combined phase noise of the transmitter laser and local oscillator at the receiver with linewidth Δv and n_i collectively models ASE noise generated from inline amplifiers which are complex circularly symmetric Gaussian random processes. Laser phase noise is typically modeled as a Wiener process in which the phase differences between two adjacent symbols $\varphi_{i+1} - \varphi_i$ are modeled as zero-mean Gaussian random variables with variance $\sigma^2 = 2\pi\Delta v T_s$ and symbol period T_s.

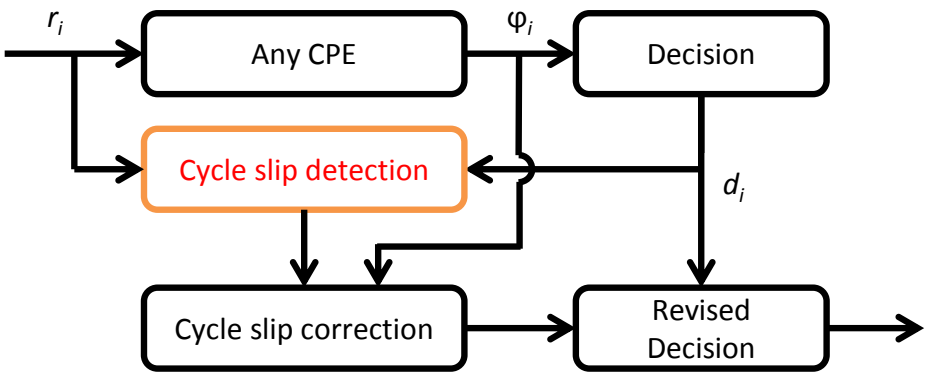

Fig. 4.1 Block diagram of the proposed CS-DC technique. The received signal r_i and decided symbol d_i are used to form y_i and the magnitude of its sliding average z_i. When CS occurs at i_{cs}, z_i undergo an abrupt drop and this very feature can be used to identify the presence of CS. To correct the CS, one can then evaluate the evolution of estimated phase $\hat{\varphi}_i$ around i_{cs} to determine if $\hat{\varphi}_i$ should be rotated by $\pi/2$ or $-\pi/2$.

The block diagram of cycle-slip detection and correction is shown in Fig. 4.1. For practical 100Gb/s, 400Gb/s and super-channel transmission systems, $\sigma^2 = 2\pi\Delta v T_s$ is

small enough such that the laser phase $e^{j\varphi_i}$ can be considered as a slowly varying process. When a cycle slip occurs, however, the estimated phase noise $\hat{\varphi}_i$ will considerably deviate from its true value φ_i. In particular, let d_i be the detected symbols from the CPE output and consider

$$y_i = [r_i d_i^* / |r_i d_i^*|]^M \approx \begin{cases} e^{jM\varphi_i} & no\ CS\ at\ i \\ e^{jM(\varphi_i \pm \pi/M)} = -e^{jM\varphi_i} & CS\ occured\ at\ i \end{cases} \quad (4.2)$$

where M is an integer determined by the degree of symmetry of the signal constellation. For instance, M is 4 if a 8-phase shift keying (8-PSK) constellation is used. Without loss of generality, we focus on square-shaped QAM signal with a phase ambiguity of $\pi/2$ and the corresponding M is set to be 2 for the rest of this paper. Therefore, if a cycle slip occurs at i_{cs}, y_i will approximately be the negative of itself before and after i_{cs}. Thus, if we consider the summation of y_i over a window length K+1, i.e.

$$z_i = \left| \sum_{k=i-\frac{K}{2}}^{i+\frac{K}{2}} y_k \right| / (K+1)$$

$$\left| \sum_{k=i-\frac{K}{2}}^{i+\frac{K}{2}} e^{j2\hat{\varphi}_k} \right| / (K+1) \quad (4.3)$$

z_i should have a minimum at i_{cs} as shown in Fig. 4.2. Such minimum can be used to detect cycle slips. To correct such cycle slips, one can study the evolution of the estimate phase $e^{j\hat{\varphi}_i}$ around i_{cs} and determine whether the CPE has incorrectly rotated the signals by $-\pi/2$ or $\pi/2$.

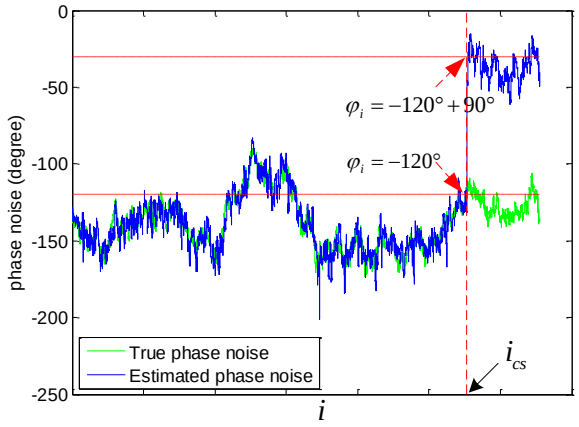

(a)

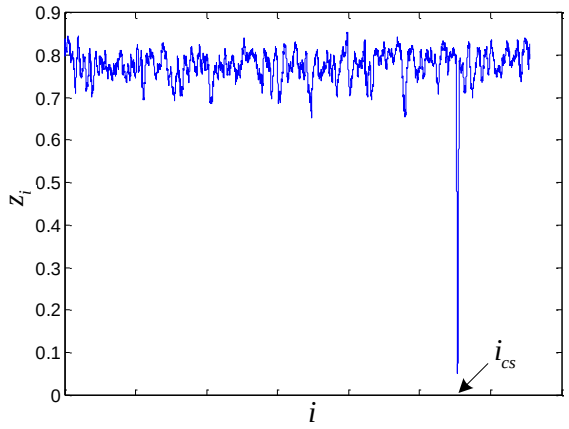

(b)

Fig. 4.2 Estimated phase evolution indicating the presence of cycle-slips and (b) evolution of the corresponding parameter z_i for CS-DC.

4.3. Theory Analysis of Cycle Slip Detection and Correction

We will begin our analysis with the summation of y_i over a window with length K+1. Since K+1 is typically larger than 50, the effect of ASE noise will be considerably averaged out and suppressed and hence can be neglected. In this analysis, nonlinear effects are not considered for simplicity purposes and simulation results on nonlinear transmission systems (described in the next section) show that nonlinear impairments

are second-order effects of the analytical insights developed herein. In addition, we assume no detection errors in the window of K+1 symbols except when a cycle slip occurred at the center of the window, which will be followed by catastrophic detection errors till the end. When there are no cycle slips, the sum of y_i over a window with length K+1 is given by

$$x_{K+1} = \sum_{k=i-K/2}^{i+K/2} y_k = \sum_{k=i-K/2}^{i+K/2} e^{j2\varphi_k} \tag{4.4}$$

which can also be expressed as

$$x_{K+1} = e^{j2\varphi_{i-K/2}} \left(\ldots \left(1 + e^{j\phi_2} \left(1 + e^{j\phi_1} \right) \right) \right) \tag{4.5}$$

where $\phi_k = 2\left(\varphi_{i+\frac{K}{2}-k+1} - \varphi_{i+\frac{K}{2}-k} \right)$ are independent identically distributed (i.i.d.) zero-mean Gaussian random variable with variance $\sigma^2 = 8\pi\Delta\nu T_s$. For the purpose of studying the magnitude of x_{K+1}, we can set the phase $\varphi_{i-K/2} = 0$ without loss of generality. Furthermore, x_{k+1} can also be recursively expressed as

$$x_{k+1} = e^{j\phi_{k+1}}(1 + x_k) \tag{4.6}$$

with $x_1 = e^{j\phi_1}$. The probability density function (pdf) $f_{x_k}(r,\theta)$ of x_k will then be given by

$$f_{x_{k+1}}(r,\theta) = f_{x_k}\left(\sqrt{1 + r^2 - 2rcos\theta}, tan^{-1}\left(\frac{rsin\theta}{rcos\theta - 1} \right) * f_\Phi(\theta) \right) \tag{4.7}$$

where $f_\Phi(\theta)$ is the pdf of ϕ_k and $*$ denotes convolution. The pdf of the magnitude is

$$z_{K+1|no\ CS} = |x_{K+1}|/(K+1) \tag{4.8}$$

which is the quantity of interest, is obtained from marginalizing $f_{x_{K+1}}(r,\theta)$ over θ and scaled by K+1 i.e.

$$f_{z_{K+1|no\ CS}}(r) = (K+1) \cdot \int_0^{2\pi} f_{x_{K+1}}\big((K+1)r, \theta\big) d\theta \tag{4.9}$$

When a cycle slip occurs at the center of the summing window followed by catastrophic detection errors, one can set $\varphi_i = 0$ without loss of generality and

$$z_{K+1|CS} = \left| \sum_{k=i-\frac{K}{2}}^{i-1} e^{j2\varphi_k} + 1 + \sum_{k=i+1}^{i+\frac{K}{2}} e^{j2\left(\varphi_k \pm \frac{\pi}{2}\right)} \right| / (K+1)$$

$$= \left| \sum_{k=i-\frac{K}{2}}^{i-1} e^{j2\varphi_k} + 1 - \sum_{k=i+1}^{i+\frac{K}{2}} e^{j2\varphi_k} \right| / (K+1). \qquad (4.10)$$

In this case, the two summation terms in (4.10) are i.i.d. with pdf $f_{x_{K/2}}(r,\theta)$ and the pdf of $z_{K+1|CS}$ can be obtained by similar derivations outlined above. Fig. 4.3 (a) and (b) depicts the pdf of x_{61} with and without CS and compared with Monte Carlo simulation results obtained from 10^9 independent realizations and the pdf of $z_{61|noCS}$ and $z_{61|CS}$ are shown in Fig. 4.4. It can be seen that the analytical derivations agree well with simulation results. Also, the analytical derivations are particularly useful for our CS analysis as they enable us to study scenarios with low CS occurrences, which are otherwise prohibited by simulations that require excessively long times.

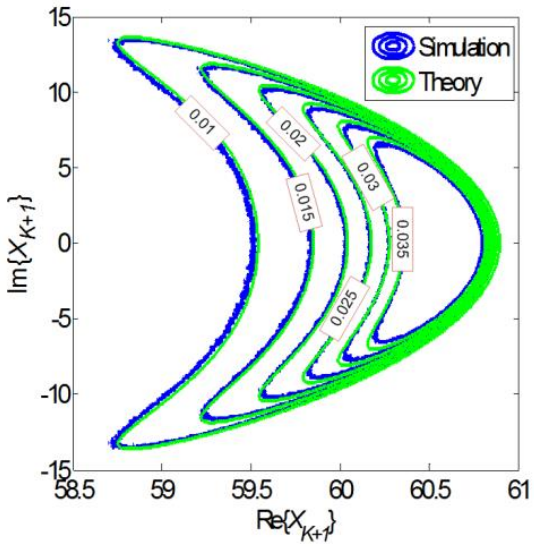

(a)

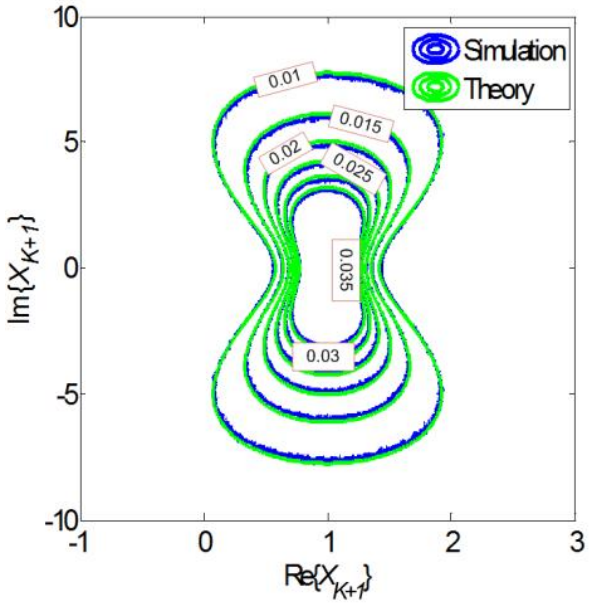

(b)

Fig. 4.3 Probability density function of (a) x_{61} without CS and (b) x_{61} with CS obtained from theory and Monte Carlo simulations. The linewidth duration product is $\Delta\nu T_s = 6 \times 10^{-4}$.

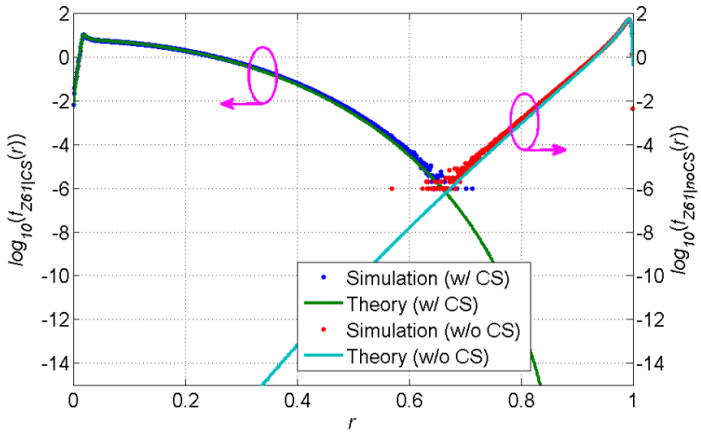

Fig. 4.4 Probability density function of $z_{61|CS}$and $z_{61|noCS}$. The linewidth duration product is $\Delta\nu T_s = 6 \times 10^{-4}$.

The proposed CS-DC technique detects cycle slips by examining whether z_i is smaller than a threshold Z_{th}. The threshold should be set to minimize the cycle slip probability P_{post} after CS-DC, given by

$$P_{post} = P_{pre} \cdot P_{miss} + \left(1 + P_{pre}\right) \cdot P_{FA} \tag{4.11}$$

Where P_{pre} is the CS probability before applying CS-DC,

$$P_{FA} = \int_0^{Z_{th}} f_{Z_{K+1|no\ CS}}(\varsigma) d\varsigma \tag{4.12}$$

is the probability of misidentifying a CS when there is none (referred to as false alarm probability hereafter), and

$$P_{miss} = \int_{Z_{th}}^{\infty} f_{Z_{K+1|CS}}(\varsigma) d\varsigma \tag{4.13}$$

is the probability of failing to identify a CS when there is one.

Fig. 4.5 shows the CS probability P_{post} after CS-DC for different thresholds Z_{th} and K. It can be seen that the optimum threshold becomes smaller with increasing averaged window length. With P_{pre} of 10^{-5}, for example, the optimum threshold decreases from 0.6 to 0.5 when the average window length doubled from 41 to 81. Also, P_{post} increases with K as the laser phase noise correlation weakens with time. The results further suggest that the optimum threshold does not change drastically with respect to window length and thus we can fix our threshold to be 0.5 for the rest of this paper.

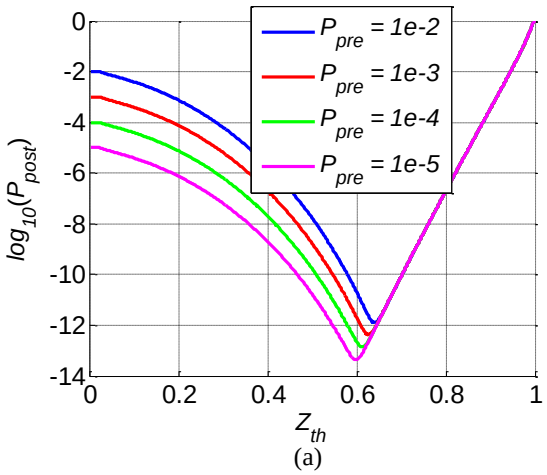

(a)

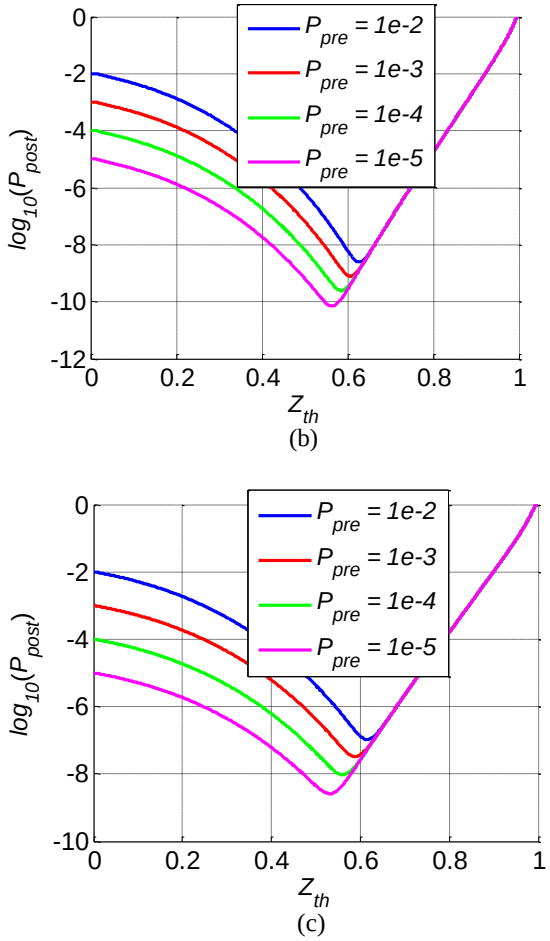

Fig. 4.5 P_{Post} versus Z_{th} with different P_{Pre} for (a) $K+1$=41, (b) $K+1$=61 and (c) $K+1$=81.

4.4. Simulation Results

Simulations are conducted to investigate the performance of the proposed CS-DC technique for PM-QPSK and PM-16-QAM systems. The CS occurrence probability before and after CS-DC is shown in Fig. 6 for 112 Gb/s PM-QPSK transmissions over 2400km and 7200 km with various optical signal to noise ratio (OSNR, in dB/0.1nm) and CPE lengths. In particular, 340M symbol sequences for each data point with gray coding were transmitted through a link consisting of multiple spans of 80-km SMF with inline optical amplifiers. The signal launched power is chosen to be 4 dBm,

significantly more than the typical launch power of 0 dBm or below so as to increase the amount of CS occurring instances. The laser linewidths of both transmitter and local oscillator are 100kHz which is typical for external cavity lasers(ECL). The receiver DSP unit includes chromatic dispersion compensation [75], polarization de-multiplexing [75] and CPE using Viterbi & Viterbi phase estimation (VVPE) method [19]. The window length for CS-DC is K+1=401. The missed cycle slips are identified by examining the bit errors patterns in a 200-symbol sliding window after carrier phase recovery or CS-DC. If the BER in the window is more than expected, i.e. 0.1, a cycle slip is assumed to have ocurred in this window. Then, the correction algorithm de-rotates the recovered data at the middle of the window with three other possible ambiguous phases and assumes the one with lowest BER to be the actual phase estimate. The whole process is carried out until the whole set of data is correctly decoded. The cycle slip probability (CSP) is calculated by dividing the amount of missed CSs with the length of the whole data set. It is obvious from Fig. 6 that CS-DC can appropriately detect and correct cycle slips and substantially reduce the CS probability by nearly two orders of magnitudes. In addition, when the CPE half-length exceeds 50, no CS has been identified except for the case of 16dB OSNR at 7200km in which the BER is as high as 5×10^{-2}, an impractical system setup. In more realistic system configurations with moderate launch power and adequate OSNR for a given transmission distance, all cycle slips are perfectly detected and corrected through CS-DC.

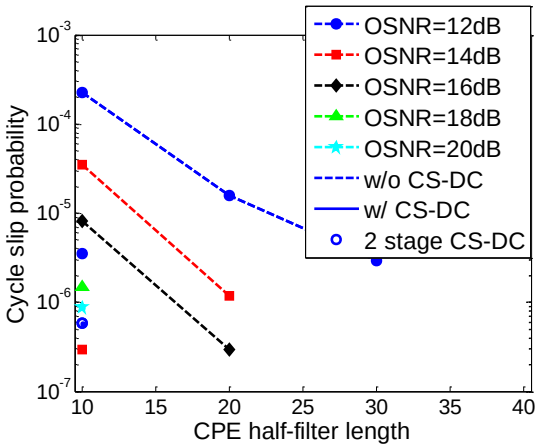

(a)

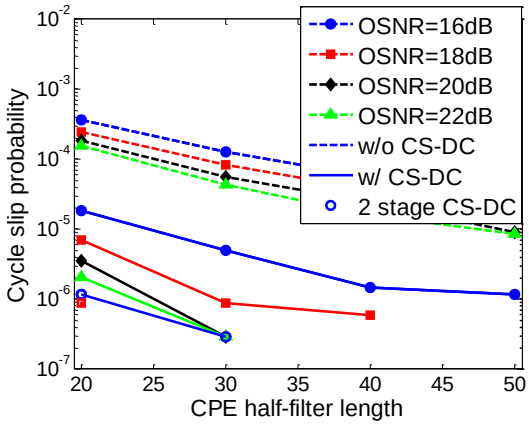

(b)

Fig. 4.6 CSP with and without the proposed CS-DC technique for a single carrier 112Gb/s PM-QPSK system with various OSNR and CPE lengths over a (a) 2400 km and (b) 7200 km link. The signal launched power is 4 dBm and the laser linewidths are 100kHz. Without CS-DC, the amount of CS for each data point ranges from 10s to more than 1200. With two-stage CS-DC, the CS probability is driven down to 0 most of the time and at most 10-6 under highly unrealistic system conditions.

The performance of the proposed CS-DC technique for 224bit/s PM-16QAM transmissions over 1200 km and 2400 km are shown in Fig. 7. 340M 16-QAM symbols are generated and the receiver DSP include CD compensation [75], constant modulus algorithm for pre-convergence followed by the cascaded multi-modulus

algorithm [76] and the CPE used is QPSK partitioning + maximum likelihood phase estimation method [51]. Other 16-QAM CPE techniques such as blind phase search [77][78] also gives similar CS-DC occurrences. The window length for CS-DC is K+1=301. The proposed CS-DC technique can reduce CS probability by at least an order of magnitude and essentially eliminate all cycle slips as long as the CPE half-filter length exceeds 30 taps.

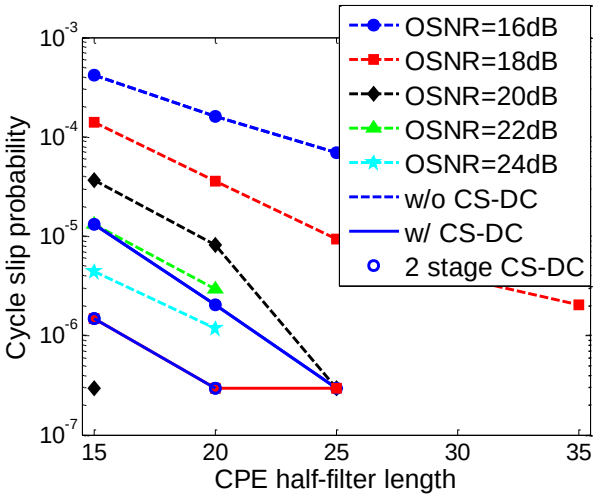

(a)

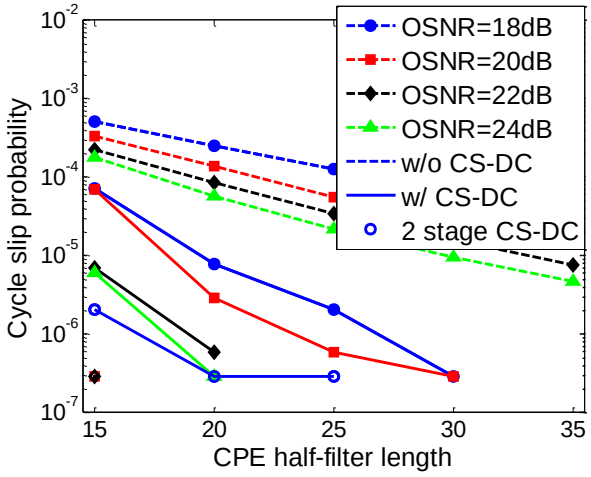

(b)

Fig. 4.7 CSP with and without the proposed CS-DC technique for a single carrier 224 Gb/s PM-16-QAM system with various OSNR and CPE lengths over a (a) 1200 km and (b) 2400 km link. The launched power is 4 dBm and the laser linewidths are

100kHz. Without CS-DC, the amount of CS for each data point ranges from 10s to more than 1700. With the proposed two-stage CS-DC, the CS probability is driven down to 0 most of the time and at most 3×10^{-7} under highly unrealistic conditions.

To study the impact of inter-channel nonlinearities, simulations have been conducted for a 5×112Gbit/s PM-QPSK Nyquist-WDM system over a 2400km SMF link and a 5×224Gbit/s Nyquist-WDM PM-16QAM system over a 1200km SMF link. The channel spacing and bandwidth are set to be 50GHz and 40GHz respectively. The launch power for each channel is 4dBm and the laser linewidths are 100 kHz. Fig. 4.8 (a) shows the CSP versus CPE half-filter length for the middle channel. Although more CSs have been observed comparing with single channel cases, the CS-DC algorithm still achieves notable CS reduction of at least one- and two-orders of magnitudes respectively for the one-stage and two-stage strategies. Without CS-DC, the amount of CS for each data point ranges from 10s to more than 2400. With 2-stage CS-DC, the CSP is driven down to 0 most of the time and at most 8×10^{-6} under highly unrealistic system conditions. Fig. 4.8 (b) shows the CSP versus CPE half-filter length. Comparing with single-carrier systems. Without CS-DC, the amount of CS for each data point ranges from 10s to more than 1700. With the proposed 2-stage CS-DC, the CSP is driven down to 0 most of the time and at most 7×10^{-6} under highly unrealistic conditions. This proves that the algorithm works effectively for the PM-QPSK signal in presence of inter-channel nonlinearities.

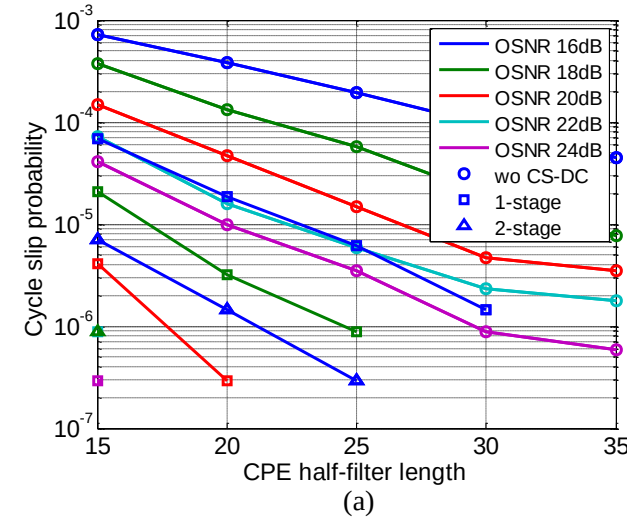

(a)

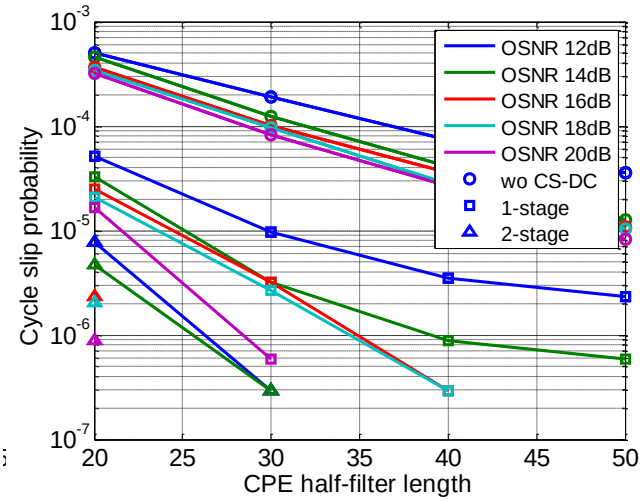

(b)

Fig. 4.8 CSP without CS-DC, with 1-stage CS-DC and with 2-stage CS-DC techniques for (a) 5×112Gbit/s PM-QPSK Nyquist-WDM system over 2400km SMF link and (b) 5×224Gbit/s PM-16QAM Nyquist-WDM system over 1200km SMF link with various OSNR and CPE lengths. The signal launched power is 4dBm per channel and the laser linewidths are 100kHz. Without CS-DC, the amount of CS for each data point ranges from 10s to more than 2400. With two-stage CS-DC, the CSP is driven down to 0 most of the time and at most 8×10^{-6} and 7×10^{-6} respectively for QPSK and 16QAM signals under highly unrealistic system conditions.

To further improve the CS mitigation performance, we can cascade an additional stage of CS-DC with a different window length K_2+1 after a first stage of CS-DC with

window length K_1+1 as shown in Fig. 4.9. This helps to detect and correct multiple cycle-slips that occurred close to each other and a first stage of CS-DC fail to correctly identify and correct all of them. With the two-stage CS-DC, Fig. 4.6-Fig. 4.8 show the final CS probability for QPSK and 16-QAM transmissions can be further reduced by ten times to below 10^{-6} and 10^{-5} for single channel and WDM systems respectively. The window length for the second-stage CS-DC is 600 and 450 for QPSK and 16-QAM transmissions respectively. Furthermore, the required CPE average length to achieve zero CS probability is shortened. This offers more flexibility for CPE length design and is beneficial to the systems with large laser linewidths. We emphasize that we intended to exemplify CS occurrences by studying highly non-linear and unrealistic system setups and the proposed CS-DC can virtually detect and correct all CS for more realistic and practical scenarios.

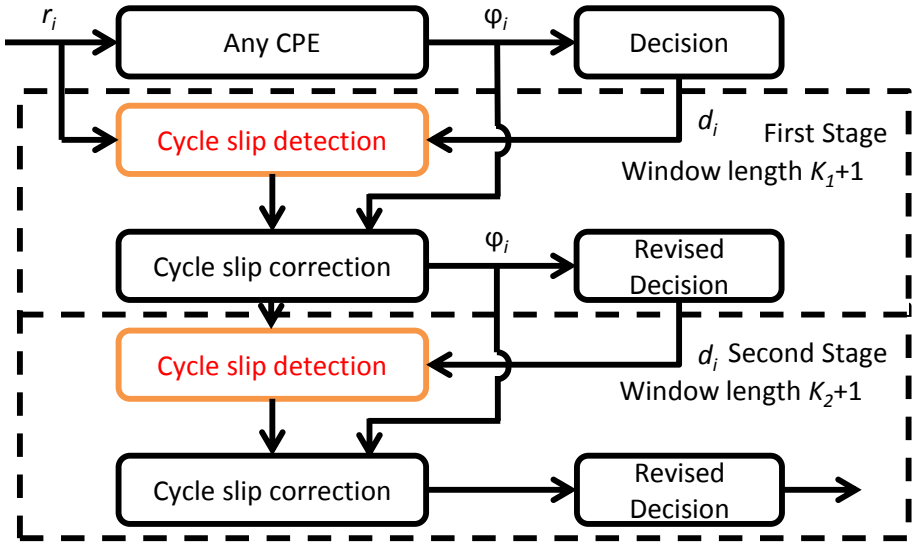

Fig. 4.9 Block diagram of two-stage CS-DC with different window lengths K_1+1 and K_2+1. The structure can help detect and correct multiple cycle-slips that occurred close to each other such that a single CS-DC may fail to identity all the cycle slips correctly.

It is unquestionably clear from the simulation results above that a longer CPE filter length is desirable in suppressing cycle slip occurrences. However, it is also known that increasing CPE filter length affects phase tracking capability especially in the highly nonlinear transmission scenarios [66]. To this end, Bisplinghoff et al. proposed to use a shorter CPE filter with half-filter length N_1 in addition to a longer one in parallel to form a slip-reduced CPE (SR-CPE) [77]. We can show that one can append CS-DC to another other algorithms to further improve CS mitigation performance. We reproduced the channel model in [77], simulate a single channel 112 Gbit/s PM-QPSK system with 210M symbols on each polarization and compare the performance between SR-CPE and SR-CPE+CS-DC. For various N_1, the required OSNR for a differentially decoded BER of 0.04 (target for turbo decoding) [77] and the CS probability is studied and shown in Fig. 4.10. Combined laser linewidth is set to be 200 kHz and the correlated nonlinear phase noise standard deviation is set from 0.2 rad to 0.8 rad [77] to investigate worst case scenarios. Compared with SR-CPE, the CS probability of SR-CPE+CS-DC is reduced by more than 10 times to well below $2\text{x}10^{-7}$ which is much lower than the upper tolerance of turbo differential decoding of 10^{-4} [66]. In addition, the best OSNR can be achieved by optimizing N_1 to be 4.

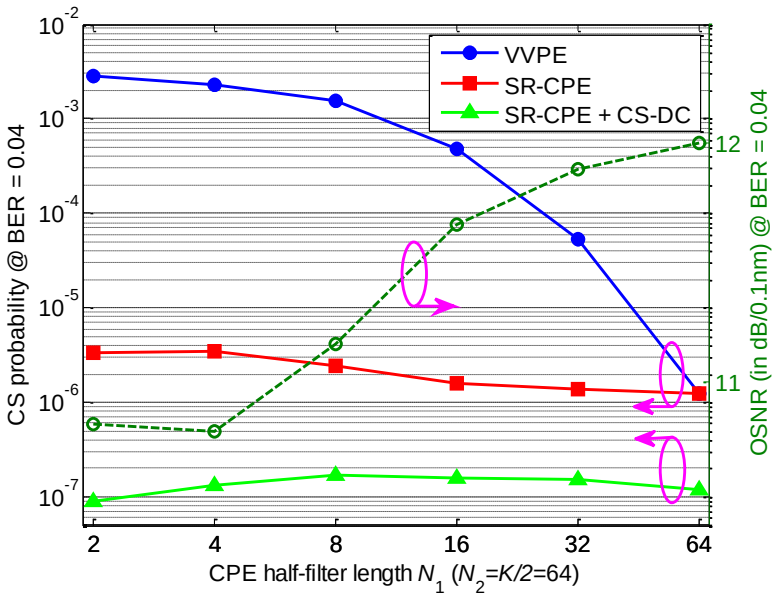

Fig. 4.10 CSP and required OSNR at BER of 0.04 for VVPE, SR-CPE and SR-CPE+CS-DC. N_1 and N_2 are half-filter lengths of short and long filers respectively in SR-CPE.

In the practical systems, frequency offset cannot be fully compensated before carrier phase recovery. Thus, it is of great importance to study CS-DC's tolerance to residue FO. For residue-FO tolerance investigation, tens of normally distributed frequency offsets are added to the input signal of carrier phase recovery. Here, the mean square error (MSE) of residue FO is defined as [78]

$$MSE = E[|\Delta f \cdot T_s|^2] \tag{4.14}$$

where T_s denotes the symbol duration and Δf denotes the difference between the actual frequency offset and the estimated frequency offset.

Fig. 4.11 (a) shows the CSP versus the MSE of residue frequency offset for a 112Gbit/s PM-QPSK system over 7200km SMF link. The MSE of the residue FO is swept from 10^{-11} to 7×10^{-9}. The launch power is 4dBm. The OSNR is set to be 16 dB

which is the worst case scenario. For the 1-stage CS-DC, no penalty has been noticed until the MSE becomes larger than 6×10^{-9}. For the 2-stage CS-DC, the missed CS rate does not change much until MSE is larger than 4×10^{-9}. This is equivalent to a FO estimation error of 1.77 MHz for a 28GBaud system. Since the achievable MSE is around 10^{-12}, it is safe to conclude that CS-DC is robust against residue FO [78]. We have also studied the impact of residue FO on the optimum average length. Extensive simulations with average lengths of 100, 200, 300 and 400 symbols have been conducted. Due to the residue FO, the best average length is 100 for the 1-stage CS-DC while the optimum length for the 2-stage CS-DC is found to be 200. This is because the phase noise evolution dynamics of most of the missed CS after the first stage CS-DC happens gradually, and therefore, average window with a length of 100 is not sufficient anymore. It also explains why the 2-stage CS-DC is more susceptible to residue FO.

Then, the same investigation has been conducted for a 224 Gbit/s PM-16QAM transmission system over 2400km SMF link as shown in Fig. 4.11 (b). The launch power is 4dBm and the OSNR is set to be 18 dB. The tolerable residue FO is compromised as the modulation order becomes higher. Nonetheless, the 1-stage CS-DC is still quite robust when the MSE is smaller than 10^{-8} while the 2-stage CS-DC can tolerate residue FO with MSE up to 10^{-9}. This is still 1000 times larger than the tolerable MSE considered in [78], and is equivalent to a FO estimation error of 885 kHz for a 28GBaud system. The best filter length is 100 for the 1-stage CS-DC

while the optimum filter length for 2-stage CS-DC is 200.

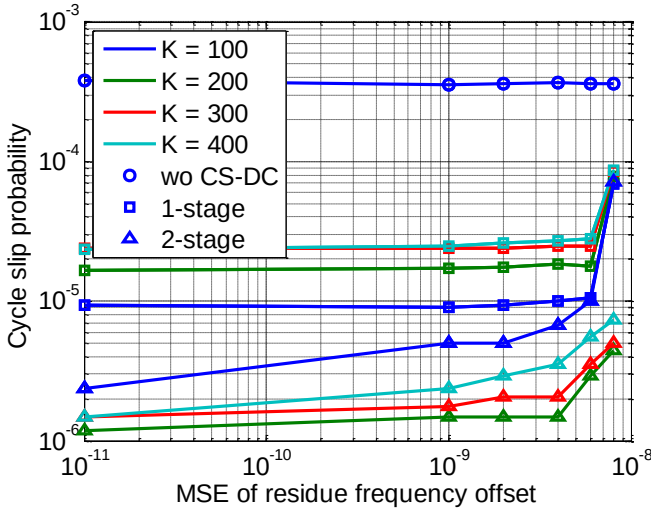

(a)

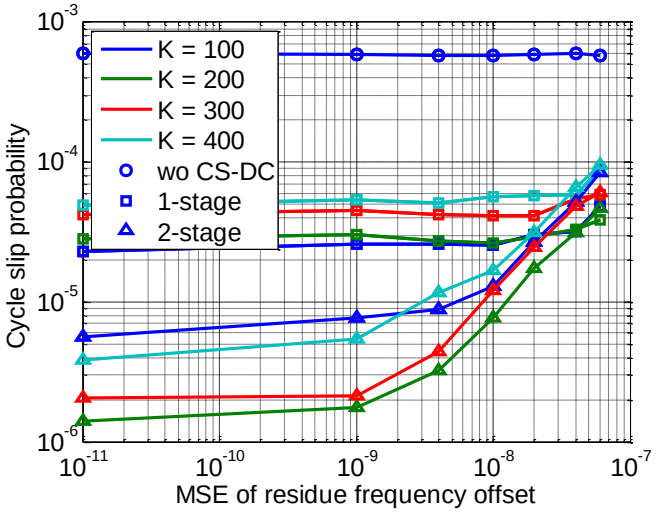

(b)

Fig. 4.11 CSP without CS-DC, with 1-stage CS-DC and with 2-stage CS-DC for (a) 112Gbit/s QPSK transmission system over 7200km SMF link and (b) 224Gbit/s 16QAM transmission systems over 2400km SMF link with various residue FO MSE. The CPE half-filter lengths are set to be 10 and 15 for QPSK and 16QAM respectively. The launch power is 4dBm. The OSNRs are set to be 16 dB and 18dB respectively for QPSK and 16QAM. K denotes the average length of CS-DC. The best average lengths are 100 and 200 for 1-stage and 2-stage CS-DC respectively.

4.5. Summary

We proposed a non-data-aided (or unsupervised) and universal CS-DC technique based on locating the minimum of the sliding average of twice estimated phase noise. The technique is independent of modulation format and choice of preceding CPE algorithms, which potentially enable the use of soft decision-forward error correction (SD-FEC) without regularly inserted pilot symbols. We analytically derived the probability density function of the CS identification metric and characterize the amount of CS reduction with the proposed CS-DC technique. Simulation results show that the CS-DC can reduce CS occurrence probability by orders of magnitudes even in systems with excessive noise and nonlinear impairments. In addition, the proposed CS-DC technique is tolerant to inter-channel nonlinearities and residue frequency offset effects and can be appended to other CS mitigation techniques reported in the literature. As CS mitigation is the primary objective of regularly inserting pilot symbols in practice, the blindness and universality of the proposed CS-DC technique may hold key to finally break such conventional wisdom and pave the way to practical implementation of non-data-aided and universal transceivers for coherent communications.

Chapter 5 Conclusions

The dissertation investigated and developed two advanced carrier phase estimation techniques each for high spectral efficiency transmission and elastic optical networks. In addition, a cycle slip detection and correction technique is also proposed for future long-haul coherent optical transmission systems. All the proposed techniques are numerically or experimentally investigated to investigate their tolerance to various system impairments such as polarization state rotation, polarization mode dispersion, frequency offset, laser linewidth, and fiber nonlinearities.

For the spectral efficient systems using PM 16-QAM signal, a low-complexity feed-forward carrier phase estimation technique is presented in chapter 2. By combining QPSK partitioning, maximum likelihood detection, and phase offset estimation between signal in different polarizations, simulation and experimental results for 200 Gb/s DP-16-QAM system demonstrate similar linewidth tolerance to the best feed-forward CPE reported while the computational complexity is at least one third time lower compared with other simplified feed-forward CPE techniques. Simulation and experimental results showed that the proposed CPE can tolerate a linewidth times symbol duration product comparable with the best feed-forward CPE techniques while the computational complexity is at least one third time lower than the simplest feed-forward CPE reported in the literature.

A modulation-format-independent or universal carrier phase estimation technique is proposed for 4-, 16-, 64- and 256-QAM transmission systems for the future elastic

optical networks in chapter 3. The proposed U-CPE eliminates the need to know the signal modulation format by using a cost function in the phase estimation update that is common to all square-shaped constellations. The U-CPE maintains close OSNR performance and linewidth tolerance with standard decision-directed phase lock loop that requires the knowledge of the modulation format and outperforms a modulation-format-oblivious-DD-PLL in which QPSK decision rules are used irrespective of actual modulation format of the signals. Simulation results show that the proposed technique has a reasonable laser linewidth tolerance for all the modulation formats even the higher order formats like 64-QAM. To demonstrate a complete modulation-format-independent signal reception system, a blind and universal DSP platform containing a new joint timing phase and frequency offset estimation technique and proposed MFI-CPE is proposed. The platform has been numerically investigated in terms of its tolerance to sampling timing offset, carrier frequency offset, polarization state rotation as well as polarization mode dispersion. Compared with the conventional training symbol aided techniques, the proposed DSP platform is capable of recovering multiple high-order modulation formats as well as the TDHQ signal only using similar initialization time as demonstrated by the experiment results indicating its effectiveness in future fast and flexible elastic optical networks.

The fourth chapter proposes a cycle slip detection and correction technique for compensating the catastrophic phase slip problem in the future coherent transmission

systems employing advanced software-defined forward error corrections. The proposed CS-DC is a simple non-data-aided or unsupervised technique based on locating the minimum of the sliding average of twice estimated phase noise. As it is blind to modulation format and CPE techniques used, the proposed CS-DC can be appended to any CPE and other cycle slip mitigation technologies. In order to evaluate the post corrected cycle slip ratio, we have numerically investigated the missed cycle slips through extensive Mont-Carlo simulations for 112Gb/s PM-QPSK and 224Gb/s PM-16-QAM systems with various OSNR, CPE averaging length, residue frequency offsets, and inter-channel nonlinearities. We also build up an analytical model to describe the post-correction cycle slip probability (CSP). In the end, a two-stage CS-DC technique is proposed with two CS-DCs cascaded together. With this modified CS-DC the post-correction CSP can be further reduced by one order of magnitude down to nearly 1×10^{-7}. Overall, the proposed CS-DC technique can be used to maximize the ability of CS mitigation in the next generation high-speed and high spectral efficiency optical transceivers.

Chapter 6 Future Perspectives

Recently, spectrum efficient transmission systems using advanced modulation techniques beyond 16-QAM begin to be deployed. For the QAM signals higher than 16-QAM, QPSK partitioning techniques are less effective as the radius difference between neighbor rings are much closer, and therefore, developing new metric to eliminate modulation phase for advanced modulation format would become a necessity. Meanwhile, the reduction of computation complexity in carrier phase estimation remains to be another challenging issue especially for higher-order modulation formats.

For elastic optical networks, the proposed blind and universal DSP platform can be modified to be more flexible by adding several identification modules. For the detection of the signal with various transmission impairments, the optical performance monitoring (OPM) techniques can be incorporated such as chromatic dispersion monitoring, OSNR monitoring, and signal identification techniques, etc. With these advanced techniques, the future DSP platform can be envisioned to be more spontaneous, automatic, and intelligent.

For the cycle slip detection and correction, the ASE noise and nonlinear phase noise is not considered when the analytical module is derived since they are the second order effects to be considered. This is true when the averaging length is sufficiently long. However, the averaging length is limited in some extreme circumstances, i.e. cost efficient transmissions using DFB lasers with large laser

linewidth, and thereby, a theoretical study with fiber nonlinearities would become a meaningful investigation. Also, an experimental investigation of the proposed technique in a single carrier or super-channel transmission system would be an interesting topic in the future.

Appendix

A. Complexity in interleaving parallelization structure using slide averaging

The required processing complexity for the proposed DP QPSK partitioning+ML scheme can be derived from Fig. 2.1 and Fig. 2.6 and separately calculated for each functional block. Here, we can separate the proposed algorithm mainly into 4 parts: partitions, VVPEs, first stage compensation and ML estimators. As discussed above the phase-offset estimation is only attributed to the first 1000 symbols, approximately 0.25% of the symbols in our experiment, we omit its complexity calculation. Computation complexity can be evaluated by counting the required operations to process 2*P* paralleled symbols from both polarizations. Without losing generosity, we let $x=a+ib$ be a received complex symbol to better illustrate the required operations, *a* and *b* represent its real and imagine parts.

1. To achieve the partition for 2*P* symbols, it requires 2*P* amplitude calculations and 2*P* amplitude comparisons with ring boundaries as shown in Fig. 2.2:
   1) Amplitude calculation require 4*P* real multipliers and 2*P* real adders: $|x|^2 = a \cdot a + b \cdot b$;
   2) Amplitude comparison: 2*P* comparators.
2. In the two VVPEs, the P C1 or C3 symbols (on average) from both polarizations require to be raised to their fourth power and normalized.

1) Each of the P fourth power operations is composed of two cascaded power operations. Thus, requiring 8P real multipliers and 4P real adders, as illustrated below:

$$real(x^2) = a \cdot a - b \cdot b = c; imag(x^2) = a \cdot b + b \cdot a = d;$$

$$real(x^4) = c \cdot c - d \cdot d = e; imag(x^4) = c \cdot d + d \cdot c = f.$$

2) The P normalization operations require P absolute value calculations realized by 2P real multipliers, P real adders and P root square operations (look-up tables), then divided with themselves using 2P real multipliers. The absolute value calculation is illustrated below:

$$\left|x^4\right| = \sqrt{\left|x^4\right|^2} = \sqrt{e \cdot e + f \cdot f}$$.

3. In the first stage carrier phase compensation, the P outcoms from y symbols need to be rotated by the phase-offset $\exp(j \cdot \theta_{offset})$, which cost 4P real multipliers and 2P real adders. Afterwards, 2P x and y polarization results of first stage estimation are summed up. P θ_n^{est1} are calculated, unwrapped and utilized to compensate the 2P x and y symbols:

   1) First stage results summation: 2LP memory unites and (2L-1)P real adders;

   2) θ_n^{est1} calculations for P x and y pairs: P 'arg(.)/4' operations which are realized by P look-up tables and P real multipliers;

   3) Unwrapping: P comparators and P real adders;

   4) First stage compensation: 8P real multipliers and 4P real adders.

4. In the ML estimator, 2P outcomes from the first stage estimation are multiplied

with their conjugated decisions and summed up to calculate the second stage phase noise estimation. After the 2P symbols be compensated, final decisions will be made:

1) First stage decision: 2P slicers;
2) Multiply with first stage decision: 8P real multipliers and 4P real adders;
3) Second stage results summation: (2L-1)P real adders and 2LP memory unites;
4) θ_n^{est2} calculation: P arg(.) realized by P look-up tables;
5) Second stage compensation: 8P real multipliers and 4P real adders;
6) Final decision: 2P slicers.

The computation complexity of dual polarization QPSK partitioning+ML CPE should be 43*P* real multipliers, 4*LP*+20*P* real adders, 4*P* slicers, 4*LP* memory unites, 3*P* comparators, 3*P* LUTs.

B. Complexity of the proposed CPE in interleaving structure using block averaging

The complexity computation of block averaging is almost the same except for the summing process and phase noise calculations, since block averaging only compute one estimated phase noise for each block. For a block of 2*P* symbols, to calculate θ_n^{est1} or θ_n^{est2} only require (2*P*-1) adders and 1 arg(.), realized by look-up table. Unwrap is also reduced to 1 comparator and 1 real adder. In addition, the memory units for summation are also not needed anymore.

The computation complexity of block based dual polarization QPSK partitioning+ML CPE should be: 40*P*+1 real multipliers, 23*P*-1 real adders, 4*P* slicers, 2*P*+1comparators, *P*+2 LUTs.

Reference

[1] E. Ip, A. P. T. Lau, D. J. F. Barros and Joseph M. Kahn, "Coherent detection in optical fiber systems," *Opt. Exp*., vol. 16, no. 2, pp. 753–791, Jan. 2008.

[2] S. Kawanishi, H. Takara, K. Uchiyama, T. Kitoh, M. Saruwatari, "100 Gbit/s, 50 km, and nonrepeated optical transmission employing all-optical multi/demultiplexing and PLL timing extraction," *Electron. Lett.*, vol. 29, no. 12, pp. 1075–1077, Aug. 1993.

[3] P. J. Winzer, G. Raybon, M. Duelk, "107-Gb/s optical ETDM transmitter for 100G Ethernet transport," in *Proc. Eur. Conf. Optical Communication* (*ECOC*) *2005*, Paper Th4.1.1.

[4] P. J. Winzer, G. Raybon, C.R. Doerr, L.L. Buhl, T. Kawanishi, T. Sakamoto, M. Izutsu, K. Higuma, "2000-km WDM transmission of 10 × 107-Gb/s RZ-DQPSK," in *Proc. Eur. Conf. Optical Communication* (*ECOC*) 2006, Paper Th4.1.3.

[5] OIF, "100G Ultra Long Haul DWDM Framework Document," OIF document, June 30, 2009.

[6] I. P. Kaminow, T. Li, and A. E. Willner, *Optical Fiber Telecommunications VI B.* New York: Academic, 2013.

[7] K. Roberts, "100G-Key technology enablers of 100Gbit/s in carrier networks," in *Proc. Opt. Fiber Commun. Conf.* (*OFC/NFOEC*) *2011*, Los Angeles, CA, paper NWA1.

[8] G.P. Agrawal, *Nonlinear Fiber Optics*, 4th ed. San Diego, CA: Elsevier, 2006.

[9] R. Kudo, T. Kobayashi, K. Ishihara, Y. Takatori, A. Sano, E. Yamada, H. Masuda,

Y. Miyamoto, and M. Mizoguchi, “Two-stage Overlap Frequency Domain Equalization for Long-haul Optical Systems,” in *Proc. Opt. Fiber Commun.Conf.(OFC/NFOEC) 2009*, San Diego, CA, paper. OMT3.

[10] F. Gardner, “A BPSK/QPSK timing-error detector for sampled receivers,” *IEEE Trans. Commun.*, vol. 34, No. 5, pp. 423-429, May 1986.

[11] M. Oerder and H. Meyr, “Digital filter and square timing recovery,” *IEEE Trans. Commun.*, vol. 36, no. 5, pp. 605-612, May 1988.

[12] K. Mueller and M. Muller, “Timing recovery in digital synchronous data receivers,” *IEEE Trans. Commun.*, vol. 24, no. 5, pp. 516-531, May 1976.

[13] Y. Han and G. Li, “Coherent optical communication using polarization multiple-input- multiple-output,” *Opt. Exp.*, vol. 13, no. 19, pp. 7527-7534, Sep. 2005.

[14] D. N. Godard, “Self-Recovering Equalization and Carrier Tracking in Two-Dimensional Data Communication Systems,” *IEEE Trans. Commun.*, vol. COM-28, no. 11, pp. 1864-1875, Nov. 1980.

[15] X. Zhou, J. Yu and P. Magill, “Cascaded two-modulus algorithm for blind polarization de-multiplexing of 114-Gb/s PDM-8-QAM optical signals,” in *Proc. Opt. Fiber Commun. Conf.* (*OFC/NFOEC*) *2009*, San Diego, CA, paper OWG3.

[16] H. Louchet, K. Kuzmin and A. Richter, “Improved DSP algorithms for coherent 16-QAM transmission,” in *Proc. Eur. Conf. Optical Communication* (*ECOC*) 2008, Brussel, Belgium, Paper Tu.1.E.6.

[17] T. Nakagawa, M. Matsui, T. Kobayashi, K. Ishihara, R. Kudo, M. Mizoguchi, and Y. Miyamoto, “Non-Data-Aided Wide-Range Frequency Offset Estimator for QAM Optical Coherent Receivers,” in *Proc. Opt. Fiber Commun. Conf. (OFC/NFOEC) 2011*, Los Angeles, CA, paper OMJ1.

[18] D. Rife and R. R. Boorstyn, “Single tone parameter estimation from discrete-time observations,” *IEEE Trans. Inf. Theory*, vol. 20, no. 5, pp. 591–598, Sep. 1974.

[19] A. J. Viterbi and A. N. Viterbi, “Nonlinear estimation of PSK-modulated carrier phase with application to burst digital transmission,” *IEEE Trans. Inf. Theory*, vol. 29, no. 4, 543–551, July 1983.

[20] G. Li, “Recent advances in coherent optical communication,” *Adv. Opt. Photon.*, vol. 1, no. 2, pp. 279-307, Apr. 2009.

[21] T. Pfau, S. Hoffmann, R. Noe, “Hardware-efficient coherent digital receiver concept with feedforward carrier recovery for M-QAM constellations,” *J. Lightw. Technol.*, vol. 27, no. 8, pp. 989-999, Apr. 2009.

[22] S. K. Oh and S. P. Stapleion, “Blind phase recovery using finite alphabet properties in digital communications,” *Electron. Lett.*, vol. 33, no. 3, pp. 175–176, Jan. 1997.

[23] X. Li, Y. Cao, S. Yu, W. Gu, and Y. Ji, “A simplified feed-forward carrier recovery algorithm for coherent optical QAM system,” *J. Lightwave Technol*., vol. 29, no. 5, pp. 801-807, Jan. 2011.

[24] J. Li, Lei Li, Z. Tao, T. Hoshada, J. C. Rasmussen, “Laser-linewidth-tolerant feed-forward carrier phase estimator with reduced complexity for QAM,” *J. Lightwave Technol.*, vol. 29, no. 16, pp. 2358-2364, Aug. 2011.

[25] O. Gerstel, M. Jinno, A. Lord, and S. J. Yoo, “Elastic Optical Networking: A new dawn for the optical layer?” *IEEE Commun. Mag.*, vol. 50, no. 2, pp. s12-s20, Feb. 2012.

[26] http://www.ciena.com/technology/wavelogic3/

[27] M. Jinno, H. Takara, B. Kozicki, Yukio Tsukichima, Y. Sone, and S. Matsuoka,

"Spectrum-efficient and scalable elastic optical path network: architecture, benefits, and enabling technologies," *IEEE Commun. Mag.*, vol. 47, no. 11, pp. 66–73, Nov. 2009.

[28] A. Leven, N. Kaneda and S. Corteselli, "Real-Time Implementation of Digital Signal Processing for Coherent Optical Digital Communication Systems," *IEEE J. Sel. Top. Quantum Electron.*, vol. 16, no. 5, pp. 1227-1234, Sept/Oct. 2010.

[29] E. Ip and J. M. Kahn, "Feedforward Carrier Recovery for Coherent Optical Communications," *J. Lightwave Technol*. vol. 25, no. 9, pp. 2675-2692, Sep. 2007.

[30] A. H. Gnauck, R. W. Tkach, and A. R. Chraplyvy, and T. Li, "High-capacity optical transmission systems," *J. Lightwave Technol.*,vol. 26, no. 9, pp. 1032-1045, May 2008.

[31] E. Ip, A. P. T. Lau, D. J. F. Barros, and J. M. Kahn, "Coherent detection in optical fiber systems," *Opt. Exp*., vol. 16, no. 2, pp. 753-791, Jan. 2008.

[32] G. Charlet, J. Renaudier, H. Mardoyan, P. Tran, O. Pardo, F. Verluise, M. Achouche, A. Boutin, F. Blache, J. Dupuy, and S. Bigo, "Transmission of 16.4 Tbit/s capacity over 2550 km using PDM QPSK modulation format and coherent receiver," in *Proc. Opt. Fiber Commun. Conf. (OFC/NFOEC) 2008*, San Diego, CA, paper PDP3.

[33] P. J. Winzer, "Beyond 100G Ethernet," *IEEE Commun. Mag*., vol. 48, no. 7, pp. 26-30, July 2010.

[34] P. Andrekson, "Metrology of Complex Optical Modulation Formats," in *Proc. Opt. Fiber Commun. Conf. (OFC/NFOEC) 2011*, Los Angeles, CA, Paper OWN1.

[35] P. J. Winzer, A. H. Gnauck, C. R. Doerr, M. Magarini, and L. L. Buhl, "Spectrally Efficient Long-Haul Optical Networking Using 112-Gb/s

Polarization-Multiplexed 16-QAM," *J. Lightwave Technol.*, vol. 28, no. 4, pp. 547-556, Sep. 2010.

[36] S. Zhang, P. Y. Kam, J. Chen, and C. Yu, "Bit-error rate performance of coherent optical M-ary PSK/QAM using decision-aided maximum likelihood phase estimation," *Opt. Exp.*, vol. 18, no. 12, pp. 12088-12103, May 2010.

[37] M. G. Taylor, "Phase estimation methods for optical coherent detection using digital signal processing," *J. Lightwave Technol.*, vol. 27, no. 7, pp. 901-9144 Apr. 2009.

[38] M. Seimetz, "Laser linewidth limitations for optical systems with high-order modulation employing feed forward digital carrier phase estimation," in *Proc. Opt. Fiber Commun. Conf. (OFC/NFOEC) 2008*, San Diego, CA, Paper OTuM2.

[39] I. Fatadin, D. Ives and S. J. Savory, "Laser Linewidth Tolerance for 16-QAM Coherent Optical Systems using QPSK Partitioning", *IEEE Photon. Technol. Lett.*, vol. 22, no. 9, pp. 631-633, May 2010.

[40] F. Rice, B. Cowley, B. Moran, and M. Rice, "Cramer-Rao lower bounds for QAM phase and frequency estimation," *IEEE Trans. Commun.*, vol. 49, no. 9, pp. 1582-1591, Sep. 2001.

[41] T. Pfau and R. Noe, "Phase-noise-tolerant two-stage carrier recovery concept for higher order QAM formats," *IEEE J. Sel. Top. Quantum Electron.*, vol. 16, no. 5, pp. 1210-1216, Sep. 2010.

[42] X. Zhou, "An Improved Feed-Forward Carrier Recovery Algorithm for Coherent Receivers with M-QAM Modulation Format," *IEEE Photon. Technol. Lett.*, vol. 22, no. 14, pp. 1051-1053, July 2010.

[43] Q. Zhuge, C. Chen, and D. V. Plant, "Low computation complexity two-stage feedforward carrier recovery algorithm for M-QAM," in *Proc. Opt. Fiber Commun. Conf. (OFC/NFOEC) 2011*, Los Angeles, CA, Paper OMJ5.

[44] J. Li, Lei Li, Z. Tao, Takeshi Hoshada, Jens C. Rasmussen, "Laser-Linewidth-Tolerant Feed-Forward Carrier Phase Estimator with Reduced Complexity for QAM," *J. Lightwave Technol*., vol. 29, no. 16, pp. 2358-2364, Aug. 2011.

[45] Y. Gao, A. P. T. Lau, C. Lu, Y. Li, J. Wu, K. Xu, W. Li, and J. Lin, "Low-Complexity Two-Stage Carrier Phase Estimation for 16-QAM Systems using QPSK Partitioning and Maximum Likelihood Detection" in *Proc. Opt. Fiber Commun. Conf. (OFC/NFOEC) 2011*, Los Angeles, CA, Paper OMJ6.

[46] A. H. Gnauck, G Charlet, P. Tran, P. J. Winzer, C. R. Doerr, J. C. Centanni, E.C. Burrow, T. Kawanishi, T. Sakamoto, and K. Higuma, "25.6-Tb/s WDM transmission of polarization-multiplexed RZ-DQPSK signals," *J. Lightwave Tchnol*., vol. 26, no. 1, pp. 79-84, Jan. 2008.

[47] R. R. Muller and Darli Augusto De Arruda Mello, "Phase-Offset Estimation for Joint-Polarization Phase-Recovery in DP-16-QAM Systems," *IEEE Photon. Technol. Lett.,* vol. 22, no. 20, pp. 1515-1517, Oct. 2010.

[48] T. Okoshi, K. Kikuchi, and A. Nakayama, "Novel method for high resolution measurement of laser output spectrum," *Electron. Lett.*, vol. 16, no. 16, pp. 630-631, July 1980.

[49] I. Fatadin, S. J. Savory, and D. Ives, "Compensation of quadrature imbalance in an optical QPSK coherent receiver," *IEEE Photon. Technol. Lett*, vol. 20, no. 20, pp. 1733-1735, Oct. 2008.

[50] X. Zhou and Y. Sun, "Low-complexity, blind phase recovery for coherent receivers using QAM modulation," in *Proc. Opt. Fiber Commun. Conf. (OFC/NFOEC) 2011*, Los Angeles, CA, Paper OMJ3.

[51] Y. Gao, A. P. T. Lau, S. Yan, and C. Lu, "Low-complexity and phase noise tolerant carrier phase estimation for dual-polarization 16-QAM systems," *Opt.*

Exp., vol. 19, no. 22, pp. 21717-21729, Oct. 2011.

[52] I. Fatadin, D. Ives, S. J. Savory, "Blind Equalization and Carrier Phase Recovery in a 16-QAM Optical Coherent System," *J. Lightw. Technol.*, vol. 27, no. 15, pp. 3042-3049, Aug. 2009.

[53] M. Angelou et al., "Spectrum, cost and energy efficiency in fixed-grid and flex-grid networks," *in Proc. Conf. Opt. Fiber Commun. Conf. (OFC/NFOEC)* 2012, Los Angeles, Paper NM3F.4.

[54] R. Elschner et al., "Experiment demonstration of a format-flexible single-carrier coherent receiver using data-aided digital signal processing," *Opt. Exp.*, vol. 20, no. 26, pp. 28786-28791, Dec. 2012.

[55] Q. Zhuge, M. Morsy-Osman, X. Xu, M. Chagnon, Q. Meng, and D. V. Plant, "Spectral efficiency-adaptive optical transmissoin susing time domain hybrid QAM for agile optical networks," *J. Lightw. Technol.*, vol. 31, no. 15, pp. 2621-2628, Aug. 2013.

[56] X. Zhou, L. E. Nelson, and P. Magill, "Rate-adaptable optics for next generation long-haul transport networks," *IEEE Commun. Mag.*, vol. 51, no. 3, pp. 41–49, 2013.

[57] M. Eiselt, B. Teipen, K. Grobe, A. Autenrieth, and J. –P. Elbers, "Programmable modulation for high-capacity networks," in *Proc. Eur. Conf. Optical Communication* (*ECOC*) *2011*, Geneva, Switzerland, Paper Tu.5.A.5.

[58] H. Y. Choi, T. Tsuritani, and I. Morita, "BER-adaptive flexible-format transmitter for elastic optical networks," *Opt. Exp.*, vol. 20, no. 17, pp. 18652-18658, Aug. 2012.

[59] R. A. Soriano, F. N. Hauske, N. G. Gonzalez, Z. Zhang, Y. Ye, and I. T. Monroy, "Chromatic dispersion estimation in digital coherent receivers," *J. Lightw. Technol.*, vol. 29, no. 11, pp. 1627-1637, Jun. 2011.

[60] Q. Sui, A. P. T. Lau, C. Lu, “Fast and Robust Blind Chromatic Dispersion Estimation Using Auto-Correlation of Signal Power Waveform for Digital Coherent Systems,” *J. Lightw. Technol*., vol. 31, no. 2, pp. 306-312, Jan. 2013.

[61] Y. Gao, A. P. T. Lau, and C. Lu, “Modulation-format-independent carrier phase estimation technique for square M-QAM systems” *IEEE Photon. Technol. Lett.,* vol. 25, no. 11, pp.1073-1076, June, 2013 .

[62] K. Piyawanno, M. Kuschnerov, B. Spinnler, and B. Lankl, “Low-Complexity Carrier Recovery for Coherent QAM using Superscalar Parallelization,” in *Proc. Eur. Conf. Optical Communication* (*ECOC*) *2010,* Torino, Italy, Paper We.7.A.3.

[63] H. Sun and K.-T. Su, “A novel dispersion and PMD tolerant clock phase detector for coherent transmission systems,” *in Proc. Opt. Fiber. Commun. (OFC) 2011*, Los Angeles, CA, Paper OMJ4.

[64] E. Ibragimov, B. Zhang, T. J. Schmidt, C. Malouin, N. Fediakine, and H. Jiang, “Cycle slip probability in 100G PM-QPSK systems” *in Proc. Opt. Fiber Commun. (OFC) 2010*, San Diego, CA, Paper OWE2.

[65] C.R.S Fludger, D. Nuss, and T. Kupfer, “Cycle-slips in 100G DP-QPSK tranmission systems” *in Proc. Opt. Fiber. Commun. (OFC)* 2012, Los Angeles, CA, Paper OTu2G. 1.

[66] A. Bisplinghoff, S. Langenbach, T. Kupfer, and B. Schmauss, “Turbo differential decoding failure for a coherent phase slip channel” in *Proc. Eur. Conf. Optical Communication* (*ECOC*) *2012,* Amsterdam, Netherlands, Paper Mo.1.A.5.

[67] C. Xie and G. Raybon, “Digital PLL based frequency offset compensation and carrier phase estimation for 16-QAM coherent optical communication systems” in *Proc. Eur. Conf. Optical Communication* (*ECOC*) *2012,* Amsterdam, Netherlands, Paper Mo.1.A.2.

[68] S. Zhang, X. Li, P. Y. Kam, C. Yu, and J. Chen, “Pilot-assisted, decision-aided,

maximum likelihood phase estimation in coherent optical phase-modulated systems with nonlinear phase noise," *IEEE Photon. Technol. Lett*., vol. 22, no. 6, pp. 380-382, Mar. 2010.

[69] T. Yoshida, T. Sugihara, K. Ishida, and T. Mizuochi, "Cycle slip compensation with polarization block coding for coherent optical transmission: two-dimensional phases constellation corresponds to a slip stage," *IEEE Signal Process. Mag.,* vol. 31, no. 2, pp. 82-92, Mar. 2014.

[70] H. Zhang, Y. Cai, D. G. Foursa, and A. N. Pilipetskii, "Cycle slip mitigation in POLMUX-QPSK modulation" *in Proc. Opt. Fiber. Commun. (OFC) 2011*, Los Angeles, CA, Paper OWE2.

[71] Y. Gao, A. P. T. Lau, and C. Lu, "Cycle-slip resilient carrier phase estimation for polarization multiplexed 16-QAM systems" *in Proc. Opto. Electron. Commun. Conf. (OECC) 2012*, Busan, Korea, Paper 4B2-4.

[72] H. Cheng, Y. Li, M. Yu, J. Zang, J. Wu, and J. Lin, "Experimental demonstration of pilot-symbol-aided cycle slip mitigation for QPSK modulation format," *in Proc. Opt. Fiber Commun. (OFC) 2014,* San Francisco, CA, Paper Th4D.1.

[73] A. P. T. Lau, Y. Gao, Q. Sui, D. Wang, Q. Zhuge, M. Morsy-Osman, M. Chagnon, X. Xu, C. Lu, and D. V. Plant, "Advanced DSP techniques enabling high spectral efficiency and flexible transmissions: toward elastic optical networks," *IEEE Signal Process. Mag.*, vol. 31, no. 2, pp. 82-92, Mar. 2014.

[74] Y. Gao, A. P. T. Lau, C. Lu, Y. Dai, and X. Xu, "Blind cycle-slip detection and correction for coherent communication systems" in *Proc. Eur. Conf. Optical Communication* (*ECOC*) *2013*, London, U. K., Paper P.3.16.

[75] S. J. Savory, "Digital filters for coherent optical receivers," *Opt. Exp.*, vol. 16, no. 2, pp. 804-817, Jan. 2008.

[76] X. Zhou, J. Yu, and P. Magill, "Cascaded two-modulus algorithm for blind

polarization de-multiplexing of 114-Gb/s PDM-8-QAM optical signals" *in Proc. Opt. Fiber Commun. (OFC) 2009*, San Diego, CA, Paper OWG3.

[77] A. Bisplinghoff, C. Vogel, T. Kupfer, S. Langebach, and B. Schmauss, "Slip-reduced carrier phase estimation for coherent transmisssion in the presence of non-linear phase noise" *in Proc. Opt. Fiber Commun. (OFC) 2013*, Anaheim, CA, Paper OTu3I.1.

[78] M. Selmi, Y. Jaouen, and P. Ciblat, "Accurate digital frequency offset estimator for coherent PolMux QAM transmission systems," in *Proc. Eur. Conf. Optical Communication* (*ECOC*) *2009*, Vienna, Austria, Paper P3.08.